Quantum Microwave Radiation and its Interference Characterized by Correlation Function Measurements in Circuit Quantum Electrodynamics

Christian Lang

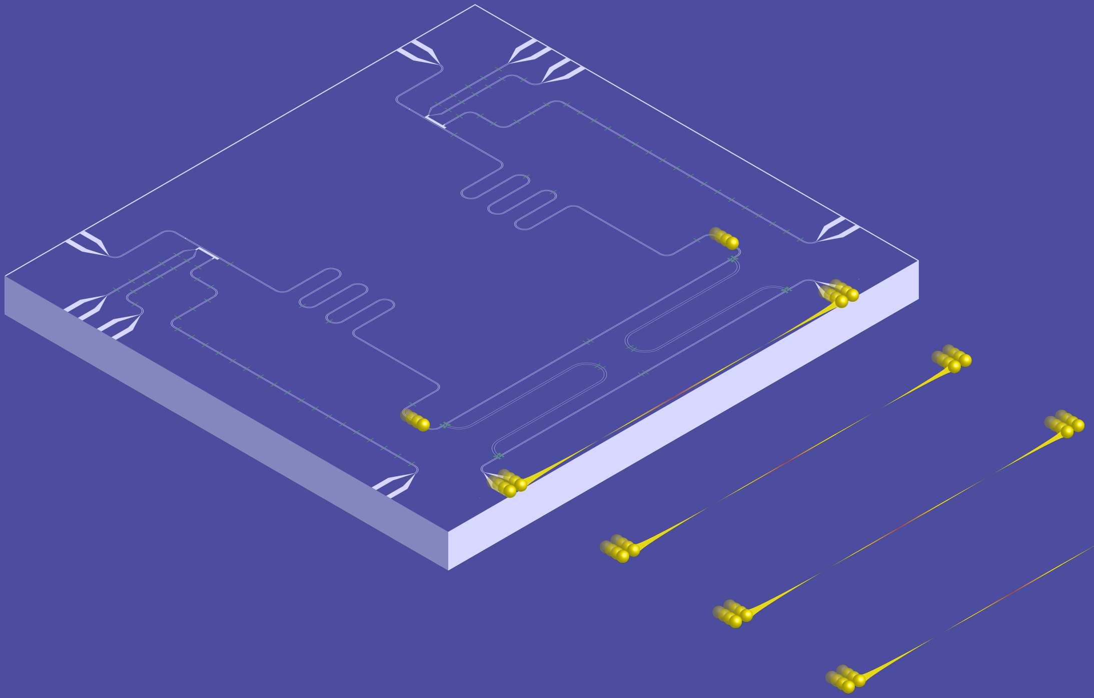

DISS. ETH NO. 21779

Quantum Microwave Radiation and its Interference Characterized by Correlation Function Measurements in Circuit Quantum Electrodynamics

A thesis submitted to attain the degree of

DOCTOR OF SCIENCES of ETH ZURICH

(Dr. sc. ETH Zurich)

presented by

Christian Lang

Diplom-Physiker (Univ.), Ludwig-Maximilians-University of Munich

born on 31.12.1980
citizen of Germany

accepted on the recommendation of

Prof. Dr. Andreas Wallraff, examiner
Dr. Denis Vion, co-examiner

2014

Abstract: Superconducting circuits provide an attractive architecture for quantum optics experiments in solid state systems. Microwave radiation interacts strongly with individual (macroscopic) quantum systems, and enables to realize emitters of single photons. The statistical property of emitting exactly a single photon as information carrier makes these emitters relevant for quantum communication and information processing protocols. To display statistical properties of a radiation source, their correlation functions are usually measured. In the optical frequency domain this is realized using photo detectors. At microwave frequencies linear amplifiers effectively measure the amplitude of propagating electromagnetic fields. However, noise necessarily added to the microwave signal in the process of amplification and inefficiencies of correlation function measurements prevented studies of the statistics of microwave-frequency quantum fields and their interference effects up to now. In this thesis I discuss the statistical characterization of continuous and pulsed single-photon sources, and investigate two-photon interference at an on-chip beam splitter.

I demonstrate that even in the presence of a high noise level characteristic for conventional microwave amplifiers, the photon statistics of quantum radiation sources can be acquired. Correlation functions are extracted by recording the linearly amplified electromagnetic field and analyzing it using efficient digital signal processing. Field programmable gate array (FPGA) based electronics is developed to process and average these data continuously and in real-time. Through first-order correlations I investigate resonance fluorescence and Rayleigh scattering in Mollow-triplet-like spectra. Single-photon antibunching is clearly observed in second-order correlation function measurements. We fully characterize the coalescence of indistinguishable single photons at an on-chip beam splitter into a pair of photons, generating non-local entanglement in the beam splitter output modes.

The measurement device developed within this thesis project has widely broadened microwave frequency signal analysis, and enables real-time feed-back in future experiments due to customizable signal processing. The presented experiments constitute a first step towards using single-photon sources and two-photon interference at microwave frequencies for quantum communication and information processing.

Zusammenfassung: Supraleitende Schaltkreise bieten eine attraktive Plattform für quantenoptische Experimente im Festkörper. Mikrowellenstrahlung koppelt an einzelne (makroskopische) Quantensysteme und erlaubt es dadurch Emitter von Einzelphotonen zu realisieren. Die statistische Eigenschaft genau ein einzelnes Photon als Informationsträger zu emittieren macht diese Einzelphotonenquellen relevant für die Quanten-Kommunikation und Informationsverarbeitung. Um statistische Eigenschaften von Strahlungsquellen zu bestimmen, werden typischerweise ihre Korrelationsfunktionen gemessen. Bei optischen Frequenzen wird dies mittels Photodetektoren realisiert. Im Mikrowellenbereich wird mit linearen Verstärkern die propagierende elektromagnetische Feldamplitude gemessen. Jedoch haben das Rauschen, das beim Verstärken notwendigerweise über das Mikrowellensignal gelegt wird, und ineffiziente Messmethoden von Korrelationsfunktionen bislang Studien der statistischen Eigenschaften von Quantenfeldern im Mikrowellenbereich und Interferenzeffekten erschwert. In dieser Abhandlung diskutiere ich die statistische Charakterisierung von kontinuierlicher und gepulster Einzelphotonenstrahlung und analysiere Zweiphotoneninterferenz am Strahlteiler auf einem Mikrochip.

Ich zeige, dass trotz eines hohen Rauschlevels die Photonenstatistik von Quantenstrahlungsquellen aufgenommen werden kann. Die Korrelationsfunktionen werden über das Auslesen des linear verstärkten elektromagnetischen Feldes und dessen Analyse mit effizienter digitaler Signalverarbeitung extrahiert. Die digitale Signalverarbeitung und stetiges Mitteln ist dabei in Echtzeit auf FPGA-basierter Elektronik realisiert. In Mollow-Triplett ähnlichen Spektren untersuche ich Resonanzfluoreszenz und Rayleigh-Streuung mittels Korrelationen erster Ordnung. Antibunching von Einzelphotonen wird in Messungen von Korrelationsfunktionen zweiter Ordnung deutlich sichtbar gemacht. Des Weiteren charakterisieren wir vollständig die Koaleszenz zweier ununterscheidbarer Einzelphotonen am Strahlteiler in ein einziges Photonenpaar, die einen räumlich verschränkten Zustand in den beiden Ausgangsmoden des Strahlteilers generiert.

Das Messinstrument, welches im Rahmen dieser Arbeit entwickelt wurde, hat die Analysemöglichkeiten von Mikrowellenstrahlung um ein

Vielfaches erweitert. Weiter erlaubt es in Zukunft, dank anpassbarer Signalverarbeitung, Experimente mit Rückkopplungsmöglichkeiten in Echtzeit durchzuführen. Die hier vorgestellten Experimente bilden erste Schritte hin zu Quanten-Kommunikation und Informationsverarbeitung auf der Basis von Einzelphotonen und Zweiphotoneninterferenz bei Mikrowellenfrequenzen.

Contents

1 Introduction 1

2 Cavity QED with Superconducting Circuits 9
- 2.1 Cavity QED 9
- 2.2 Circuit QED 12
  - 2.2.1 Coplanar Waveguide - Resonator 13
  - 2.2.2 Artificial Atom - Transmon Qubit 15
  - 2.2.3 Coupling of Resonator and Transmon 19
  - 2.2.4 Fabrication of Circuit QED Devices 21
- 2.3 Energy Level Diagram 21
- 2.4 Dispersive Regime 26
  - 2.4.1 Qubit Read-Out 27
  - 2.4.2 Qubit Control 31
- 2.5 On-Chip Beam Splitter 33
- 2.6 Experimental Setup 38
  - 2.6.1 Thermal Radiation and Dilution Refrigerator . 38
  - 2.6.2 Sample Mount and Magnetic Shielding 41

2.6.3 Cabling and Control Signal Generation 42
2.6.4 Synchronization 46

3 Quantum Signal Analyzer 49
3.1 Heterodyne Detection Chain 50
3.2 Linear Signal Processing 54
3.3 Linear Detection in the Frequency Domain 55
3.4 Operator Formulation of Linear Detection 59
3.5 Measurement of Power 62
3.6 Data Reduction 63
3.7 Scattering Parameter Measurement 64
3.8 Time-Dependent Ensemble Average 65
3.9 Two-Time Correlations 67
3.10 Measurements of Moments 70

4 Photon Blockade 73
4.1 Effective Photon-Photon Interactions 74
4.2 Observation of Mollow Triplets 77
4.3 Measurement of Photon Statistics 79

5 Pulsed Single Photons 83
5.1 Triggered Single-Photon Source 83
5.2 Time Dependence of Field and Power Measurements . 86
5.3 Measurement of Correlation Functions 89

6 Hong-Ou-Mandel Experiments 95
6.1 Two-Photon Interference 96
6.2 Measurement of Photon Statistics 99
6.3 Observation of Spatial Entanglement 102
6.4 Superposition State Interference 104

7 Summary and Outlook 107

A FPGA 111
A.1 Principles of FPGA Data Processing 112
A.2 FPGA Board Hardware 113
A.3 FPGA Communications 116

B Reconstruction of Two-Time Correlations 119
B.1 Power Spectral Density 120
B.2 Cross-Power Spectral Density 121
B.3 Second-Order Auto-Correlation 122
B.4 Second-Order Cross-Correlation 123
B.5 Cross-Power Auto-Correlation 124

C Theoretical Expressions 127
C.1 Photon Blockade 127
C.1.1 Resonance Fluorescence Spectrum 127
C.1.2 Master Equation Simulation 130
C.2 Pulsed Photons and their Interference 132
C.2.1 Temporal Mode Function 132
C.2.2 Second-Order Correlations and Interference . . 134

List of Figures 137

Glossary 139

Acronyms 145

Bibliography 147

Acknowledgements 165

Curriculum Vitae 167

1

Introduction

Quantum optics is a research field of physics in which quantum-mechanical phenomena of electromagnetic radiation and its interaction with matter are studied (Walls and Milburn, 2008). This field of research has its foundation over one hundred years ago, when Planck (1900, 1901) and Einstein (1905) proposed that the energy of electromagnetic radiation is distributed in discrete packets, namely quanta of light. These specific quanta were shortly after referred to as photons. This renewal in thinking was in contrast to the common classical theory of electrodynamics based on Maxwell's equations, which states that electromagnetic radiation is described by waves. Today, it is commonly accepted that electromagnetic radiation shows both, wave and particle character (Walls and Milburn, 2008).

Experimental advances in the last decades allow physicists to control the state of individual quantum systems, not only of photons but also other quantized states, such as the spin or the energy of an electron bound to the nucleus of an individual atom. "For ground-breaking experimental methods that enable measuring and manipulation of individual quantum systems" Haroche (2013) and Wineland (2013) were honored by the 'Nobel Prize in Physics 2012'. Although their experimental systems are very different, they share fundamental conceptual aspects: Both systems involve a quantized harmonic oscillator and a few atoms that provide an anharmonic energy level structure.

Due to the high level of control over individual quantum states, which has been demonstrated in these experiments, it was soon realized that these and similar systems may find application in the realization of a quantum computer. These days quantum computation is an extremely active field of research worldwide, and many experiments use approaches from quantum optics.

The field of research addressed in the present thesis is cavity quantum electrodynamics (QED), a subfield of quantum optics, see, for example, Haroche and Raimond (2006) and Walls and Milburn (2008). A generic cavity QED system consists of a harmonic oscillator describing a single mode of the electromagnetic field and one two-level system. Illustratively spoken, radiation is trapped between two highly reflective mirrors and bounces back and forth between the two mirrors. The two-level system is located inside of the cavity, and has two discrete energy levels. The two-level system can be in any quantum superposition of its two energy eigen-states, the ground state $|g\rangle$ and the excited state $|e\rangle$. By the exchange of energy the electromagnetic radiation in the cavity interacts with the two-level system. The interaction strength is typically weak in free space, but the interaction time is massively prolonged due to the large number of round-trips of the radiation in the cavity. This prolongation allows us to investigate the interaction between single quanta and is, hence, one reason for the frequent use of cavities around atoms. In physical implementations, the two-level system is often considered to be a single particle, such as an atom, with an anharmonic energy level spectrum. Two of its discrete energy levels are then effectively used as the two-level system. Due to the anharmonicity, transitions to the other levels happen at sufficiently small rates. Thus, these levels can be neglected in many cases.

Cavity QED systems cannot only be implemented by highly excited Rydberg atoms in a microwave cavity (Haroche, 2013) or groundstate atoms in an optical cavity (Thompson, Rempe, and Kimble, 1992), but also with solid state artificial atoms such as semiconductor quantum dots (Yoshie *et al.*, 2004) or with superconducting qubits (Wallraff *et al.*, 2004). Advantages of solid state systems are amongst others the possibility to customize designs and the prospect of easy scalability to more degrees of freedom. In the present thesis, we use the framework of circuit QED (Wallraff *et al.*, 2004; Blais *et al.*, 2004; Schoelkopf and Girvin, 2008), which allows us to implement cavity QED experiments on a superconducting chip. A typical chip consists of superconducting coplanar waveguides, which are used to confine a mode of the electromagnetic field in the microwave frequency range. Further, macroscopic superconducting circuits realize artificial atoms, for which various designs are used. All designs include a superconducting quantum interference device (SQUID), due to which the circuits have anharmonic energy level structures as required for artificial atoms. The energy difference between two of these energy levels corresponds to frequencies in the microwave domain.

We use such superconducting circuits to generate microwave frequency photons traveling freely along a coaxial transmission line. In quantum-mechanics, radiation is frequently described in the Fock basis, where an n-photon Fock state refers to radiation that consists of exactly n photons. A continuous electromagnetic wave, say coherent radiation emitted from a laser, is thus described as a superposition of infinitely many Fock states which are Poissonian distributed with mean photon number $|\alpha|^2$. Coherent radiation can also be described by Maxwell's equations ignoring field quantization, so that it is referred, together with thermal radiation, as classical radiation. From a quantum-mechanical point of view, pure Fock states and especially the single-photon Fock state are of particular interest. For example efficient single-photon sources have technological relevance for quantum key distribution (Bennett and Brassard, 1984) and linear optics quantum computation (Knill, Laflamme, and Milburn, 2001). The realization and characterization of both continuous and pulsed single-photon sources is one focus of the present thesis.

Equally relevant as generating single-photon Fock states is the unambiguous demonstration of successful single-photon generation. Hanbury Brown and Twiss (HBT) developed a new type of interferometer to measure correlations in the intensity fluctuations of two signals (Hanbury Brown and Twiss, 1956). Using a beam splitter and two photo detectors their method can be used to demonstrate the single-photon character of a radiation source. A beam splitter is an ideally lossless device with two inputs and two outputs. The input radiation leaves the beam splitter at either one of its two outputs with equal probability. An example of such a device for optical radiation is a half silvered mirror. To split a single radiation beam into the two outputs, the second beam splitter input is left the vacuum state. At both beam splitter outputs a photo detector is placed to produce a signal, referred to as a *click*, whenever a photon is detected. For a single-photon at the beam splitter input either one of the photo detectors clicks, but never do both. However, for more than one photon at the beam splitter input, there is a non-zero probability that both photo detectors click simultaneously. Thus, the absence of simultaneous clicks demonstrates the single-photon character of the radiation at the beam splitter input. Denoting by τ the time difference between clicks of the two detectors and introducing τ into the statistics, we are able to measure the so-called second-order correlation function $G^{(2)}(\tau)$, from which the photon number distribution can be inferred. This makes the measurement of correlation functions crucial to explore quantum-mechanical characteristics of electromagnetic radiation (Carmichael, 2002). In the optical frequency domain, where efficient photon detectors are available, the HBT-setup introduced above is nowadays the standard approach to measure second-order correlation functions of radiation.

Since microwave photons carry five orders of magnitudes less energy than optical photons it is considerably more challenging to build efficient photon counters for the microwave frequency domain. When I started this thesis project there were no microwave photon counters available and today they are still under development (Chen *et al.*, 2011; Romero, García-Ripoll, and Solano, 2009). In contrast to optical setups not the photon flux but the field amplitudes of the radiation are the typical measurement observable in the microwave frequency domain. Therefore, we could not measure second-order correlation functions of microwave radiation analogous as done in optics. In this thesis, we realize a measurement scheme to evaluate second-order correlation functions based on the measured field amplitudes (da Silva *et al.*, 2010). Hereby, the nonlinearity of photon flux detection is mimicked mathematically, for which digital signal processing, extensive calculations and statistics are necessary before the measurement data can be averaged. To cope with these in real-time, we developed and programmed a field programmable gate array (FPGA) based measurement device which allows highly parallelized digital data analysis (Lang *et al.*, 2013a).

The main focus of this thesis is the realization and demonstration of this new approach for correlation function measurements at microwave frequencies. As interesting sources of radiation, we implement both a continuous (Lang *et al.*, 2011) and a pulsed (Bozyigit *et al.*, 2011a) single-photon source and measure their second-order correlation function using an HBT-like setup employing an on-chip microwave beam splitter.

To demonstrate the quality and flexibility of our single-photon sources, we implement two individual sources to generate indistinguishable single-photons. In contrast to leaving the second beam splitter input empty, one source each is placed at both beam splitter inputs. Whenever two indistinguishable single-photons impinge at the two inputs, they leave the beam splitter as a pair in either one of the two outputs but never as single-photons in each of the two outputs. This experiment was pioneered by Hong, Ou, and Mandel (HOM) with optical photons (Hong, Ou, and Mandel, 1987) and has become a tool to benchmark the indistinguishability of single-photon sources. It is also a key element in linear optics quantum computation schemes (Knill, Laflamme, and Milburn, 2001). Here, we demonstrate for the first time HOM interference with independently generated photons in the microwave frequency domain. Their interference at an on-chip beam splitter is investigated by a complete characterization of the radiation fields at the beam splitter outputs and their correlations (Lang *et al.*, 2013b).

To sum up, this thesis has developed microwave frequency single-photon sources, to study the statistical properties of the emitted field in correlation function measurements, and to investigate two-photon interference effects that display unique quantum characteristics. The investigations enable further steps towards quantum information processing based on microwave photons on a chip and the developed measurement scheme allows to characterize future sources of microwave radiation. Throughout this thesis I worked on four papers. The content of these papers is integrated within this thesis and presented in a unified notation.

The thesis is structured as follows:

In **Chapter 1** an introduction providing background information and setting the context of this thesis work is presented.

Chapter 2 introduces the circuit QED setting which is used for the experiments presented in this thesis. A theoretical description of a generic cavity QED system and an introduction to circuit QED is given. The theoretical model underlying these systems is illustrated and confirmed by an experimentally probed energy level diagram which is useful to explain all relevant circuit QED phenomena discussed in this thesis. Furthermore, I introduce the experimental methods and setup.

Chapter 3 describes linear microwave detection and the FPGA based electronics I developed to perform all real-time data analyses presented. It is based on:

C. Lang, D. Bozyigit, Y. Salathe, C. Eichler, and A. Wallraff. *Quantum Signal Analyzer for Itinerant Microwave Radiation.* Technical Report, ETH Zurich, Switzerland (2013a).

Chapter 4 discusses a continuously pumped single-photon source. Coherent radiation is converted into a train of single photons, created by coherently driving a two-level system (Carmichael, 2002; Walls and Milburn, 2008). Hereby effective photon-photon interactions are realized, an effect that enables future experimental work on coupled cavity arrays. Additionally, measurements of second-order correlation functions of coherent and thermal radiation are shown. This chapter is based on:

C. Lang, D. Bozyigit, C. Eichler, L. Steffen, J. M. Fink, A. A. Abdumalikov Jr., M. Baur, S. Filipp, M. P. da Silva, A. Blais, and A. Wallraff. *Observation of Resonant Photon Blockade at Microwave Frequencies Using Correlation Function Measurements.* Phys. Rev. Lett. **106**, 243601 (2011).

In **Chapter 5** the generation and characterization of a pulsed single-photon source is presented. We clearly observe single-photon coherence in first-order and photon antibunching in second-order correlation function measurements of the propagating fields. This chapter is based on:

D. Bozyigit, C. Lang, L. Steffen, J. M. Fink, C. Eichler, M. Baur, R. Bianchetti, P. J. Leek, S. Filipp, M. P. da Silva, A. Blais, and A. Wallraff. *Antibunching of microwave-frequency photons observed in correlation measurements using linear detectors.* Nat. Phys. **7**, 154 (2011a).

In **Chapter 6** I describe HOM experiments, where we demonstrate the indistinguishability of photons from independent triggered single-photon sources. We investigate the non-local entanglement in the beam splitter output modes, which is likely to be of importance for quantum communication and information processing based on microwave frequency photons. This chapter is based on:

C. Lang, C. Eichler, L. Steffen, J. M. Fink, M. J. Woolley, A. Blais, and A. Wallraff. *Correlations, indistinguishability and entanglement in Hong-Ou-Mandel experiments at microwave frequencies.* Nat. Phys. **9**, 345 (2013b).

In **Chapter 7** my thesis is summarized and its importance for future research is outlined.

2

Cavity QED with Superconducting Circuits

2.1 Cavity QED

In this section, I give a short introduction into a generic cavity quantum electrodynamics (QED) system, where a harmonic system is coupled to a single two-level system. This includes also an introduction to the Jaynes-Cummings Hamiltonian, which is a theoretical model for the aforementioned generic cavity QED system. To incorporate both the coupling to the measurement system, and residual coupling to the environment, we discuss the finite lifetimes of cavity field and two-level system excitations.

In the field of cavity QED the interaction between electromagnetic radiation confined in a cavity and atoms is investigated (Haroche and Raimond, 2006). The cavity consists of two highly reflecting mirrors; compare green mirrors in Figure 2.1. Illustratively, photons can bounce back and forth multiple times between the mirrors before leaving the cavity. This process forms a stationary electromagnetic field satisfying the boundary condition, that the field of the stationary wave has an anti-node at the location of each mirror. Consequently, only fields with specific frequencies are allowed, namely the cavity modes, while fields with other frequencies are suppressed. We consider

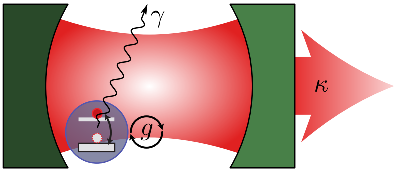

Figure 2.1: Cavity QED system. A single two-level atom (blue), located preferably at a field anti-node, couples with rate g to the radiation (red) confined between two mirrors (green). The atom radiatively decays with rate γ into modes other than the cavity mode. A mirror with finite transmittance (light green) on the right ensures directed decay of cavity excitations with rate κ.

in the following only a single cavity mode with the resonance frequency $\nu_\mathrm{r} = \omega_\mathrm{r}/2\pi$ and assume all other modes are not excited and belong to the residual environment. We consider the right (light green) mirror in Figure 2.1 has finite transmittance such that radiation is emitted with rate κ through that mirror, as otherwise the cavity would be perfectly isolated from the outside world. The energy stored in the cavity decays to $1/e$ of its initial value within the characteristic time $1/\kappa$ enabling the observation of the decayed radiation. Alternatively, the photon loss rate κ can be translated into the dimensionless quality factor Q of the cavity defined by $Q = \omega_\mathrm{r}/\kappa = \nu_\mathrm{r}/2\delta\nu_\mathrm{r}$. Due to the finite cavity decay, the magnitude of the radiation suppression with frequencies other than the resonance frequency ν_r follows a Lorentzian line shape, and $\delta\nu_\mathrm{r}$ is the half width at half maximum (HWHM) of that Lorentzian.

Inside of the cavity a two-level atom is located, whose excited state $|e\rangle$ is coupled to the ground state $|g\rangle$ by an electric dipole transition at frequency $\nu_\mathrm{a} = \omega_\mathrm{a}/2\pi$. In analogy to a classical bit, that is in either one out of two possible states, the two-level atom is also referred to as a *qubit*, since the atom can be in any quantum superposition $c_g\,|g\rangle + c_e\,|e\rangle$ where $c_g, c_e \in \mathbb{C}$ and $|c_g|^2 + |c_e|^2 = 1$; compare blue schematic in Figure 2.1. Compared to the continuum of modes in free space the cavity modifies the density of modes available for the qubit to spontaneously decay from the excited state $|e\rangle$ to the ground state $|g\rangle$ by emitting a photon of frequency ν_{a}. Thus, the cavity protects the qubit from decay when the qubit transition is detuned from the cavity where the density of modes allowed by the cavity becomes very small. This effect is named after Purcell (1946), who considered a two-level system coupled to external circuitry (Houck *et al.*, 2008). Additionally due to imperfections in experimental setups, it is possible that the qubit decays spontaneously from state $|e\rangle$ to $|g\rangle$ with a residual characteristic rate of γ through spurious electromagnetic modes other than the cavity mode or by other energy absorption processes (Blais *et al.*, 2004).

The atom couples to the electromagnetic field in the cavity by an electric dipole interaction since the electromagnetic mode induces an electric dipole moment in the atom. When cavity and qubit are on resonance ($\nu_{\mathrm{r}} = \nu_{\mathrm{a}}$), single radiation quanta are exchanged between the qubit and the cavity field at the coupling rate g. In the strong coupling limit with $g \gg \kappa$ and $g \gg \gamma$, in which the coupling strength dominates over cavity and qubit decay rates, this energy exchange can result in *multiple* coherent oscillations referred to as vacuum Rabi oscillations (Blais *et al.*, 2004).

The system described above is well described by the Jaynes-Cummings Hamiltonian

$$\hat{H}_{\mathrm{JC}} = \hbar\omega_{\mathrm{r}} \left(\hat{A}^\dagger \hat{A} + \tfrac{1}{2} \right) + \tfrac{1}{2}\hbar\omega_{\mathrm{a}}\hat{\sigma}_z + \hbar g \left(\hat{\sigma}_- \hat{A}^\dagger + \hat{\sigma}_+ \hat{A} \right) + \hat{H}_\kappa + \hat{H}_\gamma \,, \tag{2.1}$$

where a single electromagnetic field mode is coupled to a single two-level atom (Blais *et al.*, 2004). The first term in Equation (2.1) describes the energy stored as photons in the cavity and is formally equivalent to a quantum harmonic oscillator. Here, $\hat{A}^\dagger$ denotes the creation operator of a photon in the cavity, which is defined as $\hat{A}^\dagger |n\rangle = \sqrt{n+1}\,|n+1\rangle$ such that a photon is created in addition to the n existing photons. Similarly the photon annihilation operator $\hat{A}$ is defined as $\hat{A}\,|n\rangle = \sqrt{n}\,|n-1\rangle$. Their product $\hat{A}^\dagger\hat{A}$ is interpreted as the photon number operator due to the action $\hat{A}^\dagger\hat{A}\,|n\rangle = n\,|n\rangle$. Note that $\hat{A}$ is the operator for the field *in* the resonator, while I have reserved $\hat{a}'$ for fields *emitted* from the cavity and $\hat{a}$ for fields *traveling* towards the detection setup.

The second term in the Jaynes-Cummings Hamiltonian (2.1) describes the energy stored in the qubit. The Pauli z-operator $\hat{\sigma}_z = |g\rangle\langle g| - |e\rangle\langle e|$ refers to the ground state $|g\rangle$ and the excited state $|e\rangle$ of the qubit. Together with the factor $\frac{1}{2}$ this term shows that the energy difference between the two qubit states is $\hbar\omega_\mathrm{a}$.

The interaction between the field and the qubit is described by the third term in Equation (2.1). Single energy quanta are exchanged with rate g. A transition $\hat{\sigma}_- = |g\rangle\langle e|$ from state $|e\rangle$ into state $|g\rangle$ of the qubit creates a photon $\hat{A}^\dagger$ in the cavity mode. In the case the photon is absorbed ($\hat{\sigma}_+ = |e\rangle\langle g|$) by the qubit a photon in the cavity is annihilated ($\hat{A}$).

The coupling of the cavity to the continuum and the coupling of the atom to other modes than the single cavity mode is described by the fourth and fifth terms, $\hat{H}_\kappa$ and $\hat{H}_\gamma$, of the Jaynes-Cummings Hamiltonian (2.1), respectively (Blais *et al.*, 2004). These two terms are operations that include the environment. To avoid including the environment into the model, typically the dynamics of the system is investigated using the master equation for the Jaynes-Cummings model of Equation (2.1) where the environment is incorporated as a reservoir; see e.g. Carmichael (2008).

2.2 Circuit QED

The framework of circuit QED allows to implement a cavity QED system similar to the generic model introduced in Section 2.1. The circuit QED architecture is proposed, e.g., in Blais *et al.* (2004) and an experimental realization is described in Wallraff *et al.* (2004). Figure 2.2(a) shows schematically such a circuit QED system, which has been used for the experiments presented in this thesis. Macroscopic superconducting electronic circuits are used to realize anharmonic systems, thus being *artificial* atoms (blue). Further, the artificial atom is coupled capacitively to the electric field (red) of the superconducting coplanar waveguide resonator (green). The afore mentioned building blocks are introduced in Sections 2.2.1 to 2.2.3. The presented theory

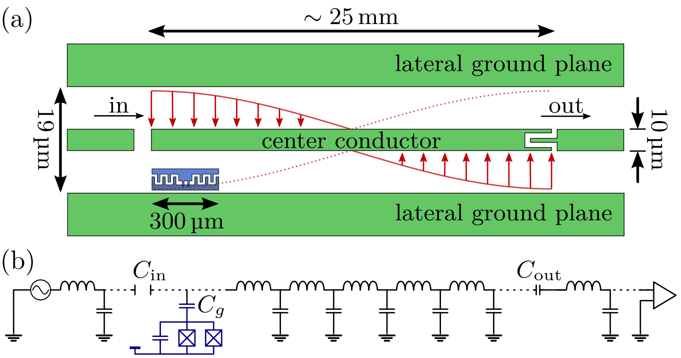

Figure 2.2: (a) Circuit QED scheme with coplanar waveguide resonator (green) and embedded transmon qubit (blue) at a resonator field anti-node. (b) Lumped element model of the waveguide resonator capacitively coupled to a SQUID-loop with parallel capacitance. Dominant field decay at the output is ensured by a larger ratio $C_{\mathrm{out}}/C_{\mathrm{in}} \gg 1$ between input and output capacitance. Dashed lines indicate the continuation of the infinitesimally small serial inductor and parallel capacitor to represent inductance L_0 and capacitance C_0 per unit length of the waveguide. See Glossary on page 139 for a description of the symbols.

follows mainly proposals of Blais *et al.* (2004, 2007) with extensions due to modifications of the artificial atom proposed by Koch *et al.* (2007).

2.2.1 Coplanar Waveguide - Resonator

In contrast to the illustrations of cavity QED in Section 2.1, where the radiation is confined in a three-dimensional cavity, the electromagnetic radiation is here confined within a waveguide. Here, we use superconducting coplanar waveguides defined by thin film patterns on a chip. A coplanar waveguide consists of a center conductor and two lateral ground planes, colored green in Figure 2.2(a). Since in the transverse direction the physical dimensions are typically much smaller than the electrical wavelength, we can draw an equivalent lumped-element circuit model for such a waveguide as shown in Figure 2.2(b) by the array of inductors and capacitors that indicate an inductance L_0 per unit length and a capacitance C_0 per unit length of the coplanar waveguide (Pozar, 2011). The width of the center conductor, the gap from the center conductor to the ground planes [compare Figure 2.2(a)] and the effective dielectric constant of the used materials define the impedance $Z_0 = \sqrt{L_0/C_0}$ of the waveguide (Göppl *et al.*, 2008). Typically, impedances of $Z_0 = 50\,\Omega$ are chosen (Pozar, 2011).

We define a resonator in the coplanar waveguide by leaving a gap in the center conductor at the input and output. This introduces an input C_{in} and an output C_{out} capacitance into the waveguide, which play the role of the mirrors in the cavity QED model of Section 2.1. Similarly as for the three-dimensional cavity the standing waves in the coplanar waveguide resonator must satisfy boundary conditions. Here, the electric field must have an anti-node at each end of the coplanar waveguide resonator, as shown for the fundamental mode in Figure 2.2(a). Thus, the resonator carries the fundamental mode (standing wave with single field node) and the harmonics thereof (standing waves with two or more field nodes) out of the continuum of possible modes supported by the waveguide. The length of the resonator together with the effective dielectric constant sets the resonance frequency ν_{r}, which we define throughout this thesis being the fundamental mode and has frequencies around 7 GHz. The ground planes confine the resonator mode laterally to a small mode volume leading to a very high electromagnetic field strength in the resonator plane, i.e. a quasi one-dimensional transmission line (Wallraff, 2008; Blais *et al.*, 2004). Due to the use of superconducting material resistive losses in the resonator are negligible at temperatures well below the critical temperature of the superconductor and at frequencies well below the superconducting gap. Intrinsic photon losses such as photon loss in the dielectric or through spurious electromagnetic modes on the chip limit the internal quality factor of the resonator to typically several hundred thousands (Göppl, 2009). However, since the resonators used in this thesis have quality factors $Q < 2000$ in the overcoupled regime photon loss through the resonator output dominates over internal photon loss.

Note that alternatives for implementing microwave resonators exist. Examples are lumped element LC-oscillators [see for example Cicak *et al.* (2009)], which do not support higher harmonics, and three-dimensional microwave cavities [see for example Paik *et al.* (2011)].

2.2.2 Artificial Atom - Transmon Qubit

In circuit QED, superconducting electric circuits are placed into the resonator that act as artificial atoms with quantized and anharmonic energy levels. Being a solid state circuitry the artificial atoms are at fixed position. Unlike real atoms, the circuits can be designed and adapted so that experimental requirements, such as transition frequencies, are met. Additionally, most current designs of superconducting artificial atoms allow to control transition frequencies by external control parameters in experiments, e.g. to bring the transition frequency of the circuit into and out of resonance with the resonator (Clarke and Wilhelm, 2008).

All types of superconducting artificial atoms incorporate at least one Josephson tunnel junction as a nonlinear circuit element (Clarke and Wilhelm, 2008). As described by Bardeen, Cooper, and Schrieffer (1957) in their theory of superconductivity, bosonic quasi-particles (Cooper pairs of electrons) *condense* into a single macroscopic state described by an effective single-particle wavefunction. This macroscopic wavefunction is the basis for the observation of atomic-scale phenomena such as the anharmonic energy level quantization in a macroscopic system (Clarke and Wilhelm, 2008). A Josephson tunnel junction consists of two superconducting leads separated by an insulating barrier of appropriate thickness (few nm). The thickness and geometry of this barrier are related to the critical current I_c up to which Cooper pairs are able to tunnel without dissipation through the barrier (Clarke and Wilhelm, 2008). The Josephson junction can be interpreted as a nonlinear inductor shunted by its intrinsic capacitance. It thus behaves like an anharmonic oscillator, which is the key property and building block for superconducting artificial atoms. The combination of Josephson inductance and intrinsic capacitance is represented as ⊠ in circuit diagrams; compare Figure 2.2(b). We refer to Clarke and Wilhelm (2008) for an overview of superconducting artificial atoms and their microscopic descriptions. In the remainder of this section, I describe in more detail the transmon type superconducting artificial atom, which has been used within the scope of this thesis. In the rest of this thesis, I refer to this specific type of artificial atom simply as a *transmon*.

The transmon is a Cooper pair box in parallel with a capacitor (Koch *et al.*, 2007). Here, we discuss the split Cooper pair box, which adds the ability to change the transition frequencies of the artificial atom by externally applying magnetic fields. The split Cooper pair box consists of a superconducting island and a superconducting reservoir that are connected by two Josephson tunnel junctions, instead of a single junction. In addition to the two intrinsic junction capacitances, there is a capacitance between island and reservoir. For the transmon regime of the split Cooper pair box this capacitance is desired to be large, as explained later in this section, and is controlled by the geometry of the characteristic finger capacitor; compare blue circuit in Figure 2.2(a) or—for a more detailed view—the false-color micrograph in Figure 2.3. The charging energy of a single electron charge e on the island is given by $E_\mathrm{c} = e^2/2C_\Sigma$, where C_Σ is the sum of the three capacitances above and the effective capacitance C_g to the resonator (which includes capacitance to ground); compare Figure 2.2(b). Island, reservoir, and the two Josephson junctions form a SQUID-loop, a ring through which a circulating super-current may flow. By externally applying magnetic flux Φ through the loop, we can tune the critical current $I_\mathrm{c}(\Phi)$ of the SQUID. The critical current $I_\mathrm{c}(\Phi)$ is periodic in the applied flux Φ with period of the flux quantum $\Phi_0 = h/2e$ and directly influences the Josephson energy defined as $E_\mathrm{J} = E_\mathrm{J}(\Phi) = I_\mathrm{c}(\Phi)\,\Phi_0/2\pi$, which describes the energy stored in the Josephson junctions due the coupling of the two superconductors. Hence, the Josephson energy varies as $E_\mathrm{J}(\Phi) = E_{\mathrm{J}\Sigma}\,|\cos(\pi\,\Phi/\Phi_0)|$, where $E_{\mathrm{J}\Sigma}$ is the maximal Josephson energy and represents a design parameter (Makhlin, Schön, and Shnirman, 2001).

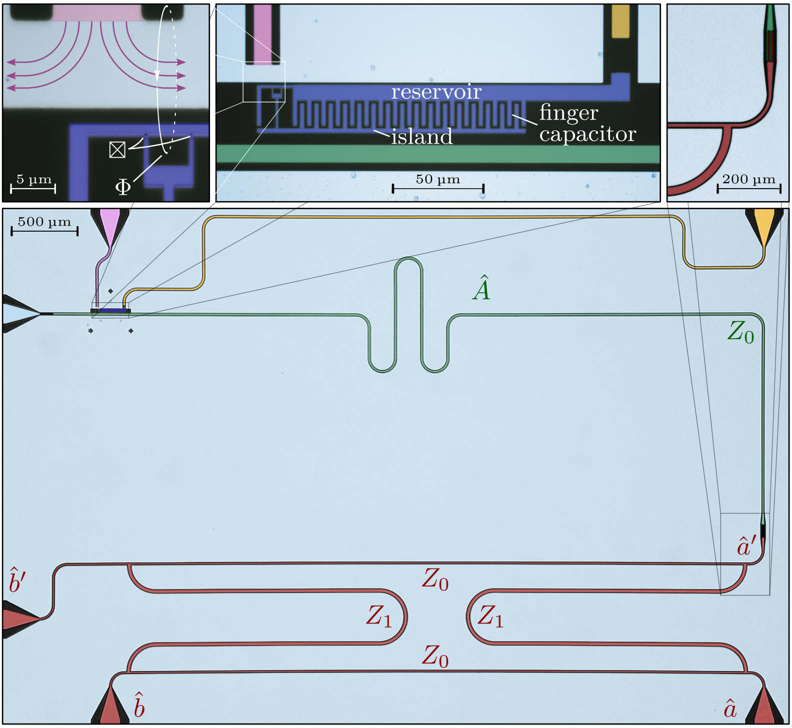
5 µm
Φ
reservoir
finger capacitor
island
50 µm
200 µm
500 µm
$\hat{A}$
Z_0
$\hat{a}'$
$\hat{b}'$
Z_0
Z_1
Z_1
Z_0
$\hat{b}$
$\hat{a}$

Figure 2.3: False-color micrograph of a circuit QED sample with beam splitter. Superconducting coplanar waveguide resonator (green) realizing resonant mode $\hat{A}$ interacting with integrated transmon (blue, left insets), which can be biased with a large bandwidth flux gate line (purple, shorted to ground) and manipulated with a charge gate line (orange). Output mode $\hat{a}'$ is coupled into the beam splitter (red) with mode $\hat{b}'$ in the vacuum state and output modes $\hat{a}$ and $\hat{b}$. Four $\lambda/4$ sections of waveguide with impedances $Z_0 = 50\,\Omega$ and $Z_1 = Z_0/\sqrt{2}$ realize the beam splitter. All superconducting ground planes (light blue) are connected via few aluminum wire bonds (not shown) over both insulating stripes (black) of the waveguides. See Section 2.2.4 for used materials and fabrication of this sample.

The Hamiltonian $\hat{H}_{\mathrm{CPB}}$ which describes the Cooper pair box on the basis of the excess[1] number of Cooper pairs m that are on the island is given by

$$\hat{H}_{\mathrm{CPB}} = 4E_{\mathrm{c}} \sum_m \big(m - m_{\mathrm{g}}\big)^2 \left|m\right\rangle\!\left\langle m\right| - \tfrac{1}{2}E_{\mathrm{J}} \sum_m \big(\left|m+1\right\rangle\!\left\langle m\right| + \text{h.c.}\big) ,$$

where $m_{\mathrm{g}} = C_{\mathrm{g}}V_{\mathrm{g}}/2e$ is the gate charge in units of number of electron pairs due to the voltage V_{g} at the island (Blais *et al.*, 2004). In the regime $E_{\mathrm{c}} \gg E_{\mathrm{J}}$ the Cooper pair box is referred to as a charge qubit, because the Hamiltonian is predominantly defined by the charge, i.e. the number of Cooper pairs m, on the island (Blais *et al.*, 2004). The energy levels E_i $(i = g, e, f, h, \ldots)$ of the Cooper pair box for the ground state $\left|g\right\rangle$, excited state $\left|e\right\rangle$, second-excited state $\left|f\right\rangle$, … are the eigen-values E_i of the Hamiltonian $\hat{H}_{\mathrm{CPB}}$ as

$$\hat{H}_{\mathrm{CPB}} \left|i\right\rangle = E_i \left|i\right\rangle \ .$$

The transition frequency $\nu_{\mathrm{a}} = (E_e - E_g)/h$ strongly depends on the gate charge m_{g} and is thus susceptible to variations of that parameter. Therefore, the gate charge m_{g} is typically controlled in experiments and adjusted to the charge degeneracy point $m_{\mathrm{g}} = 1/2$, where ν_{a} only depends to second-order on m_{g} as exploited by Vion *et al.* (2002).

In contrast, in the transmon regime of the Cooper pair box, E_{c} is reduced significantly[2] to $E_{\mathrm{c}} \ll E_{\mathrm{J}}$, so that the dependence of transition frequency ν_{a} on the gate charge m_{g} decreases exponentially with $\sqrt{E_{\mathrm{J}}/E_{\mathrm{c}}}$, which makes the energy levels E_i insensitive to gate charge fluctuations in m_{g} (Koch *et al.*, 2007; Schreier *et al.*, 2008). This insensitivity comes at the cost of reduced anharmonicity $\alpha \equiv E_{ef} - E_{ge}$ of the transition energies E_{ij}. The subsets of E_{ij} and ν_{ij} with $i, j = g, e, f, h, \ldots$ denote a transition from state $\left|i\right\rangle$ to $\left|j\right\rangle$. The anharmonicity α relates to the operation time, i.e. the maximal drive rate at which transitions between the lowest two states $\left|g\right\rangle$

---

[1] The number of additional Cooper pairs on the island compared to the neutral state.

[2] Note that the class of phase qubits have even higher $E_J \sim 10^4 \cdot E_c$ and are usually arranged in a different way (Makhlin, Schön, and Shnirman, 2001).

and $|e\rangle$ can be driven selectively, and thus at which the artificial atom still can be considered as a qubit. Since the relative anharmonicity α/E_{ge} decreases only with a weak power law in $\sqrt{E_\mathrm{c}/E_\mathrm{J}}$ resulting in $\alpha \simeq -E_\mathrm{c}$, the anharmonicity can be made sufficiently large for fast operation times while the transmon is still insensitive to gate charge fluctuations (Koch *et al.*, 2007; Schreier *et al.*, 2008). Calculating the energy levels of the transmon we find a transition energy from the ground to the excited state which can be approximated by

$$h\nu_{ge} \approx \sqrt{8E_\mathrm{c}E_{\mathrm{J}\Sigma}|\cos(\pi\tfrac{\Phi}{\Phi_0})|} - E_\mathrm{c}$$

in dependence of the flux Φ applied through the SQUID-loop, for all Φ so that $E_\mathrm{c} \ll E_\mathrm{J}(\Phi)$ is still fulfilled. The Hamiltonian for the transmon in its eigen-basis with multiple energy levels is

$$\hat{H}_\mathrm{transmon} = \sum_i \hbar\omega_i \, |i\rangle\langle i| \ ,$$

where the energy levels E_i are expressed in terms of the angular transition frequencies ω_i between ground state $|g\rangle$ and state $|i\rangle$. The dependence of the energy levels E_i on the applied flux Φ is illustrated in Section 2.3.

2.2.3 Coupling of Resonator and Transmon

To complete the discussion of the circuit QED system, we describe the coupling of the transmon to the electric field of the resonator mode. For this purpose, the transmon is fabricated into the gap between center conductor and ground plane; compare Figures 2.2 and 2.3. This gap is in the small mode volume the resonator field is concentrated in (see Section 2.2.1), which results in a strong field strength at the location of the transmon. The coupling is maximal when the transmon is positioned at an anti-node of the standing wave in the resonator. Thus, transmon and electromagnetic field of the resonator interact capacitively which can be interpreted as an electric dipole coupling. The dipole coupling is described in the uncoupled transmon state basis $|i\rangle$ by the coupling Hamiltonian

$$\hat{H}_\mathrm{c} = \sum_{i,j} \hbar g_{i,j} \; |i\rangle\langle j| \, (\hat{A}^\dagger + \hat{A}) \, ,$$

where indices i and j enumerate the states of the transmon $i, j = g, e, f, h, \ldots$ and $\hbar g_{i,j}$ are the coupling energies associated with the transmon transitions together with the emission/absorption of an excitation in the resonator mode, where $g_{i,j}$ are determined by the root mean square voltage of the resonator field and the ratios $E_\mathrm{J}/E_\mathrm{c}$ and C_g/C_Σ (Koch *et al.*, 2007). In the transmon regime of large $E_\mathrm{J}/E_\mathrm{c}$ the only relevant couplings are found to be between neighboring states of the transmon, i.e. $g_{i,i\pm 1}$ (Koch *et al.*, 2007). After applying a rotating wave approximation the effective coupling Hamiltonian of the transmon is

$$\hat{H}_\mathrm{c} = \sum_i \hbar \left(g_i \hat{\sigma}_i \hat{A}^\dagger + g_i^* \hat{\sigma}_i^\dagger \hat{A} \right) \; ,$$

where $\hat{\sigma}_i = |i\rangle\langle i+1|$ and $\hat{\sigma}_i^\dagger = |i+1\rangle\langle i|$ denote the atom lowering and raising operators, and $g_i = g_{i,i+1}$ (Koch *et al.*, 2007).

Combining resonator, transmon artificial atom, their electric dipole interaction (compare Sections 2.2.1 to 2.2.3) and dissipation of resonator and atom excitations, we describe the complete system by the effective generalized Jaynes-Cummings Hamiltonian

$$\hat{H}_\mathrm{gJC} = \hbar\omega_\mathrm{r} \left(\hat{A}^\dagger \hat{A} + \tfrac{1}{2} \right) + \sum_i \hbar\omega_i \, |i\rangle\langle i| + \sum_i \hbar \left(g_i \hat{\sigma}_i \hat{A}^\dagger + g_i^* \hat{\sigma}_i^\dagger \hat{A} \right) \; . \tag{2.2}$$

This Hamiltonian with appropriate flux-dependent treatment of transition frequencies ω_i and coupling strengths g_i is numerically diagonalized in Section 2.3 and compared to spectroscopic measurement data. For a large enough anharmonicity of the transmon we can restrict Equation (2.2) to the lowest two atomic states, $i = g, e$. In that case we refer to the transmon as the qubit and the effective Hamiltonian above reduces to the Jaynes-Cummings Hamiltonian Equation (2.1).

2.2.4 Fabrication of Circuit QED Devices

Figure 2.3 shows a false-color micrograph of the circuit QED device used for the experiments of Chapters 4 and 5. The network of coplanar waveguides and the resonator is patterned in optical lithography with approximately 200 nm thick niobium (ground plane and center conductors) on a mono-crystalline sapphire substrate. The input and output capacitances of the resonator are chosen by adjusting the gap size in the center conductor, or for larger capacitances by introducing a finger capacitor as shown in the right inset of Figure 2.3 (Göppl *et al.*, 2008).

The artificial atoms used for this thesis were patterned using electron beam lithography, with which we reach a feature size of $\sim 20\,\mathrm{nm}$ compared to $\sim 1\,\mu\mathrm{m}$ for optical lithography. To reach the required few nm thickness of the insulating barrier of the Josephson junctions, the barrier is made by aluminum oxide, and exploits shadow evaporation and an oxidation break in between the consecutive evaporation of two aluminum films which form island and reservoir (Göppl, 2009).

2.3 Energy Level Diagram

In this section we use the effective generalized Jaynes-Cummings Hamiltonian $\hat{H}_{\mathrm{gJC}}$ (2.2) to analyze the quantum-mechanics of the circuit QED system. We spectroscopically probe the lowest lying transitions and map them to a corresponding energy level diagram. Since this diagram is the solution of the Hamiltonian of the experimental system, we do not need to consider the microscopics of the Josephson junction to explain most quantum physical phenomena discussed in this thesis. We find almost perfect agreement between experimentally found energy levels and the numerical diagonalized Hamiltonian, which confirms the validity of the generalized Jaynes-Cummings Hamiltonian.

Here we discuss with the numerical diagonalization of the generalized Jaynes-Cummings Hamiltonian. To include the tunable parameter magnetic flux Φ, we rewrite $\hat{H}_{\mathrm{gJC}}$ [Equation (2.2)] incorporating the four parameters ν_{r}, $E_{\mathrm{J}\Sigma}$, E_{c}, $g = g_{g,e}$ fixed at fabrication. To numerically find the energy eigen-states and eigen-values for all $-\Phi_0/2 < \Phi \leq \Phi_0/2$, we restrict ourselves to five transmon levels $i = g, e, f, h, k$ and maximally nine photonic excitations n of the resonator for the basis denoted by $|i, n\rangle$. We have chosen more photonic excitations than transmon levels since in typical experiments the resonator is easily populated with multiple photons using a single drive frequency. Further, we exclude the dissipation terms in the diagonalization since they only influence the width but not the eigen-value itself. The obtained eigen-values of the Hamiltonian correspond to the energy levels of the complete circuit QED system. The lowest lying eigen-values are shown in Figure 2.4 for the parameters of the device shown in Figure 2.3 and used for the experiments discussed in Chapters 4 and 5. The obtained energy levels are sorted from low (purple) to high (red) energies.

If two states have the same energy and the two states are coupled by a non-zero coupling strength, the system hybridizes into a new pair of energy eigen-states, namely the symmetric and anti-symmetric superposition of the original states of the uncoupled system. This is illustrated in Figure 2.4, for example with the states $|g1\rangle$ and $|e0\rangle$ in the uncoupled basis. When the two uncoupled states have the same energy, the coupled system hybridizes into a doublet[3], and the new energy eigen-basis is an equal superposition of the uncoupled eigen-states $|1\pm\rangle = (|g1\rangle \pm |e0\rangle)/\sqrt{2}$. Away from the so-called *anti-crossing* the superposition eigen-states are dominated by either one of the uncoupled eigen-states $|g1\rangle$ and $|e0\rangle$ and the energy levels are close to the uncoupled eigen-states. In between it is an unequal superposition of the two states where the weighting increases with the uncoupled energy difference, and thus with flux Φ; compare the anti-crossing at $|1\pm\rangle$ in Figure 2.4. The energy splitting at an anti-crossing is a measure of the coupling energy between the crossing levels. The anti-crossings with small separation are due to residual coupling of second-order or less and can typically be neglected.

The same arguments as for $|1\pm\rangle$ hold for the two-excitation man-

---

[3] with different energies

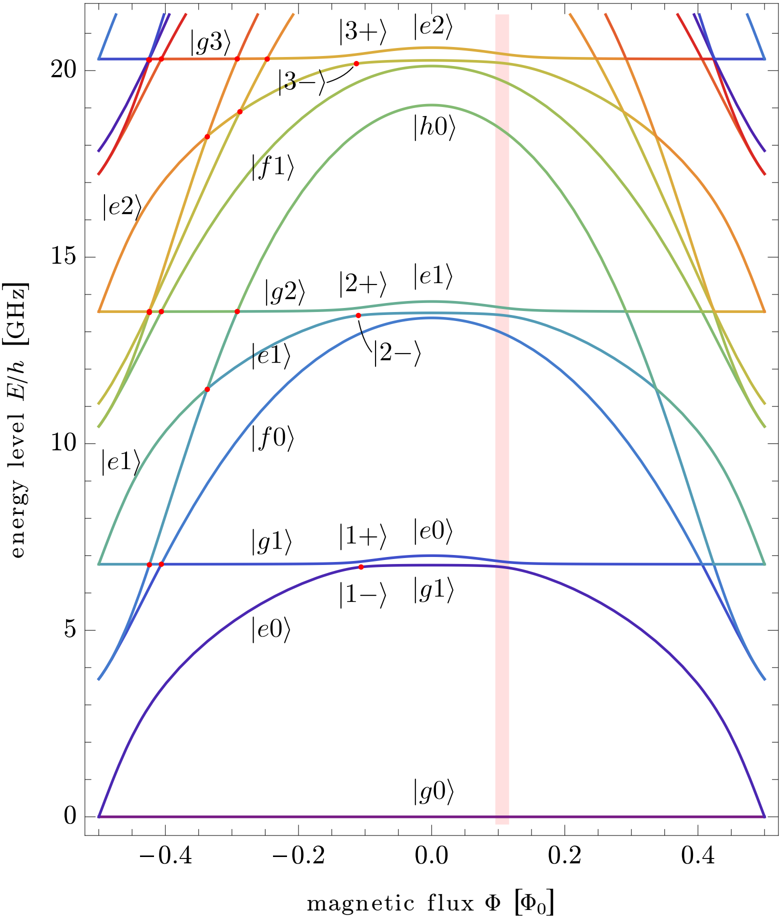

Figure 2.4: Energy level diagram of the coupled resonator transmon system. Each energy level is renamed at the anti-crossings (red dots) as shown for the states $|e0\rangle$ and $|e1\rangle$. The shaded area (also symmetrically around $\Phi = 0$) marks the Jaynes-Cummings ladder. Sample parameters for the calculation: $\nu_\mathrm{r} = 6.77\,\mathrm{GHz}$, $g/2\pi = 72.9\,\mathrm{MHz}$, $E_{\mathrm{J}\Sigma}/h = 15.12\,\mathrm{GHz}$, $E_\mathrm{c}/h = 461.8\,\mathrm{MHz}$.

ifold $|2\pm\rangle = (|g2\rangle \pm |e1\rangle)/\sqrt{2}$, the three-excitation manifold $|3\pm\rangle = (|g3\rangle \pm |e2\rangle)/\sqrt{2}$, and so on which are called together with the ground state $|g0\rangle$ the Jaynes-Cummings ladder, indicated by the red shaded area in Figure 2.4. The energy difference between the states $|n+\rangle$ and $|n-\rangle$, $n = 1, 2, \ldots$, is $\sqrt{n}\, 2\hbar g$ and due to its proportionality to $\sqrt{n}$ called the $\sqrt{n}$-nonlinearity (Carmichael, 2008; Fink *et al.*, 2008). It results from the coupling term of the Jaynes-Cummings Hamiltonian $\hat{H}_{\mathrm{JC}}$ [third term in Equation (2.1)] and with $\hat{\sigma}_+ \hat{A}\, |gn\rangle = \sqrt{n}\, |e, n-1\rangle$. The experiments presented in Chapter 4 are realized at the anti-crossing $|1\pm\rangle$.

Experimentally, we measure the energy difference between two levels, by probing transitions between them. Typically, we start by driving oscillations between the ground state $|g0\rangle$ and a second state, thus populating the respective second state, by irradiating microwaves resonant to the corresponding transition frequency. We find the transition frequencies for $|g0\rangle \leftrightarrow |g1\rangle$, $|g0\rangle \leftrightarrow |e0\rangle$, and the two-photon transition $|g0\rangle \leftrightarrow |f0\rangle$; compare the density plots in Figure 2.5. The measurements are performed by spectroscopy, where we sweep the frequency ν_{spec} of the microwave source while monitoring the population of the ground state $|g0\rangle$. Hereby, we probe the transmission of a very small microwave tone, which is resonant to the transition $|g0\rangle \leftrightarrow |g1\rangle$, through the resonator. A change (dark green areas) of the average transmission amplitude and/or phase directly relates to the average population of the transmon level $|g\rangle$ probed by the measurement (Nakamura, Chen, and Tsai, 1997; Blais *et al.*, 2004; Wallraff *et al.*, 2004; Schuster *et al.*, 2005). When we apply a microwave drive resonant with $|g0\rangle \leftrightarrow |g1\rangle$ additionally to the spectroscopy microwave ν_{spec}, we populate both[4] $|g0\rangle$ and $|g1\rangle$, and thus are able to detect also the transition frequencies for $|g1\rangle \leftrightarrow |e1\rangle$, $|g1\rangle \leftrightarrow |f0\rangle$, and $|g1\rangle \leftrightarrow |g2\rangle$; compare Figure 2.5. It should be pointed out here that the latter level $|g2\rangle$ is populated together with $|g1\rangle$ for all Φ where the transition frequency of $|g0\rangle \leftrightarrow |g1\rangle$ is resonant to $|g1\rangle \leftrightarrow |g2\rangle$. Resonant means here equal transition frequency within

---

[4] If not desired, the population of $|g1\rangle$ can be avoided by implementing pulsed spectroscopy where the microwave tone for the transmission measurement is only turned on directly after the spectroscopy microwave drive.

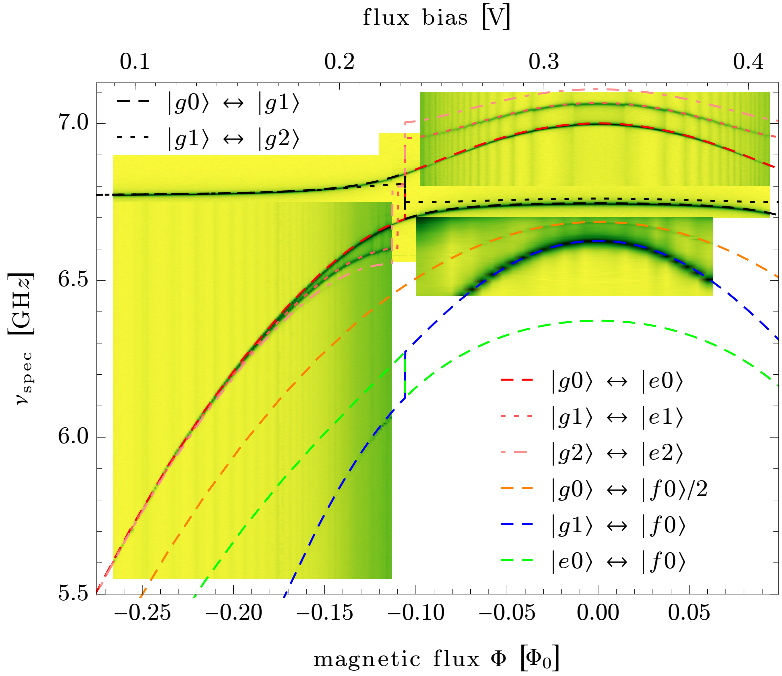

Figure 2.5: Transitions of transmon resonator system. The measurements in the background probe transitions between two energy levels. Dark green areas show that the system is affected by a microwave drive with frequency ν_{spec}. The measurements show the dependence of the transition frequencies to the applied flux bias voltage to a small coil that results in the magnetic flux Φ through the SQUID-loop of the transmon. The lines show the difference between two energy levels for the same sample parameters as in Figure 2.4.

the transitions line width, which is the case for the resonator away from the anti-crossings $|n\pm\rangle$ where resonator and artificial atom have very different frequencies and, hence, are predominantly uncoupled.

All probed transition frequencies agree very well with the numerically diagonalized Hamiltonian, lines in Figure 2.5. This demonstrates that the model introduced in Section 2.2 fits well with the experimental data. Therefore, we have gained some reasonable understanding of the system including the coupling between the resonator and the transmon artificial atom.

2.4 Dispersive Regime

So far we have shown that the coupling between resonator and transmon leads to a non-trivial energy level structure. However, in many cases it is desirable to manipulate the state of either the artificial atom or the resonator alone but not the coupled system of both at a time. In quantum information, for example, the state of the artificial atom is the computational basis, and the resonator is amongst others used to read out that state. Similarly, we need to excite the atom alone to generate pulsed single-photons in Chapters 5 and 6. Even though the artificial atom and resonator are never truly fully decoupled, a sufficient decoupling is typically easily achieved for a large range of the tunable flux Φ. It is the dispersive regime, in which the coupling g is small compared to the detuning $\Delta = \omega_\mathrm{a} - \omega_\mathrm{r}$, i.e. $g \ll |\Delta|$ and $g \ll |\Delta_e|$ where $\Delta_i = \omega_{i,i+1} - \omega_\mathrm{r}$ (Koch *et al.*, 2007). In this section, the transmon is used as a qubit with the two states $|g\rangle$ and $|e\rangle$, hence $\omega_\mathrm{a} = \omega_{ge}$. Consequences for the dispersive regime that arise from this usage are discussed in the following. A detailed description of the dispersive regime for the transmon qubit is presented in Koch *et al.* (2007).

Due to the reduced anharmonicity of the transmon, in comparison to the Cooper pair box, higher excited states need to be taken into account. Virtual transitions through these higher excited states lead to the effective dispersive Hamiltonian

$$\begin{aligned} \hat{H}^\mathrm{D} &= \left(\tfrac{1}{2}\hbar\tilde{\omega}_\mathrm{a}\right)\hat{\sigma}_z + \left(\hbar\tilde{\omega}_\mathrm{r} + \hbar\,\chi\,\hat{\sigma}_z\right)\hat{A}^\dagger\hat{A} \qquad (2.3)\\ &= \left(\tfrac{1}{2}\hbar\tilde{\omega}_\mathrm{a} + \hbar\,\chi\,\hat{A}^\dagger\hat{A}\right)\hat{\sigma}_z + \left(\hbar\tilde{\omega}_\mathrm{r}\right)\hat{A}^\dagger\hat{A}\,, \qquad (2.4)\end{aligned}$$

for the restricted two-dimensional Hilbert space of the qubit (Koch *et al.*, 2007). Here, the qubit transition frequency $\tilde{\omega}_\mathrm{a} = \omega_\mathrm{a} + \chi_{ge}$

and the cavity resonance frequency $\tilde{\omega}_\mathrm{r} = \omega_\mathrm{r} - \chi_{ef}/2$ are renormalized as consequence of the presence of the higher excited states of the transmon. The effective dispersive shift χ is given by $\chi = \chi_{ge} - \chi_{ef}/2$ with $\chi_{ij} = g_{ij}^2/(\omega_{ij} - \omega_\mathrm{r})$ leading to

$$\chi = -g^2 \frac{E_\mathrm{c}/\hbar}{\Delta(\Delta - E_\mathrm{c}/\hbar)} \,. \tag{2.5}$$

Note that the dispersive limit breaks down at the poles of this equation (Koch *et al.*, 2007).

The form of the effective dispersive Hamiltonian (2.4) illustrates the AC-Stark shift of the transmon transition frequency. The presence of each photon $\hat{A}^\dagger \hat{A}$ in the cavity shifts the transmon transition frequency by χ, which is observed in Figure 2.5 as the transitions $|g0\rangle \leftrightarrow |e0\rangle$, $|g1\rangle \leftrightarrow |e1\rangle$, and $|g2\rangle \leftrightarrow |e2\rangle$ are split into three degenerate transition frequencies around $\Phi \approx -0.15\,\Phi_0$. The splitting by χ increases the closer the qubit is operated to the vacuum Rabi mode splitting where the detuning Δ in the nominator of Equation (2.5) becomes small. In Figure 2.5 we can additionally see where the dispersive Hamiltonian $\hat{H}^\mathrm{D}$ is valid, namely for all Φ where the resonator has an harmonic spectrum with equal transition frequency $\tilde{\omega}_\mathrm{r}$ for $|g0\rangle \leftrightarrow |g1\rangle$ and $|g1\rangle \leftrightarrow |g2\rangle$; compare second term of Equation (2.4). Note that Figure 2.5 is obtained from a device which displays no dispersive regime around $\Phi \approx 0\,\Phi_0$ since the maximal qubit frequency $\tilde{\omega}_\mathrm{a}$ is not much larger than the resonator frequency $\tilde{\omega}_\mathrm{r}$. However, many circuit QED experiments use devices with $\tilde{\omega}_\mathrm{a} \gg \tilde{\omega}_\mathrm{r}$ at the flux sweet spot $\Phi \approx 0\,\Phi_0$, especially in experiments that strongly rely on the dispersive Hamiltonian.

2.4.1 Qubit Read-Out

The second term of the effective dispersive Hamiltonian $\hat{H}^\mathrm{D}$ (2.3) shows that there is a shift of the harmonic resonance frequency of $\pm\chi$ depending on the qubit state $|g\rangle$ or $|e\rangle$ as $\hat{\sigma}_z |g\rangle = |g\rangle$ and $\hat{\sigma}_z |e\rangle = -|e\rangle$. This is illustrated in Figure 2.6(a,b) by the stationary resonator

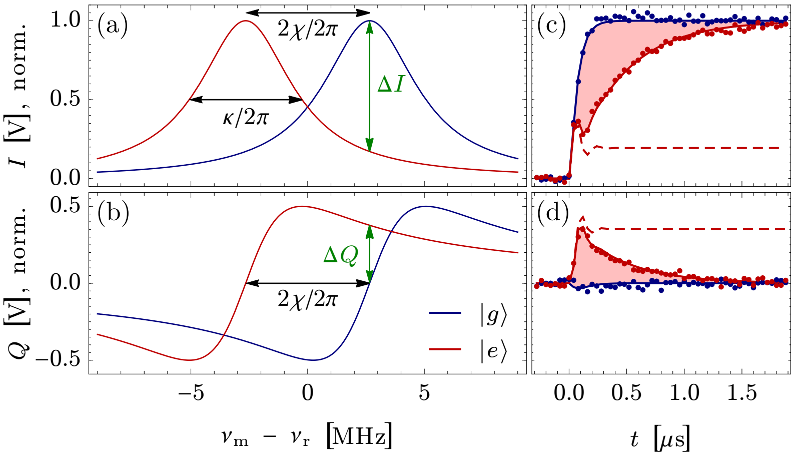

Figure 2.6: Stationary qubit state dependent resonator shift for the (a) in-phase I and (b) quadrature Q component of microwave transmission amplitude. (c,d) Time-dependent ensemble average of a pulsed qubit state read-out signal (dots) for finite qubit lifetime with fit to cavity Bloch equations (lines) and for a hypothetical infinite qubit lifetime (dashed line).

shift. Here, the in-phase (I) and quadrature (Q) component[5] of the resonance frequencies in dependence of a measurement frequency ν_m are shown. We refer to $S = I + i\,Q$ as the *complex amplitude* and to I and Q as *quadratures*. Due to coupling of the resonator to the environment (which is dominated by its input and output lines) with strength κ, the resonance frequencies have a full width at half maximum (FWHM) of $\kappa/2\pi$ in the quantity $|I|^2 + |Q|^2$; compare Section 2.1. The resonance frequency when the qubit is in state $|e\rangle$ is off-set by 2χ compared to the resonance frequency when the qubit in state $|g\rangle$. Depending on the qubit state $|g\rangle$ (blue) or $|e\rangle$ (red) a transmission measurement yields a different stationary amplitude of I and Q at ν_m as indicated by the green arrow. A measurement of the transmission is a quantum non-demolition (QND) measurement of the qubit state because the operator $\hat{\sigma}_z$ is probed by measuring the resonance frequency, and $\hat{\sigma}_z$ commutes with $\hat{H}^\mathrm{D}$, $[\hat{\sigma}_z, \hat{H}^\mathrm{D}] = 0$, which is therefore a constant of motion (Blais *et al.*, 2004). A complex superposition $|\psi\rangle = c_g\,|g\rangle + c_e\,|e\rangle$, where $c_g, c_e \in \mathbb{C}$ and $|c_g|^2 + |c_e|^2 = 1$, will be with probability $|c_g|^2$ or $|c_e|^2$ in the state $|g\rangle$ or $|e\rangle$ respectively, as soon as the state of the resonator field is determined. For a stationary qubit state, i.e. no qubit transition has happened in the meantime, further consecutive measurements of the cavity resonance frequency give the same results. A continuous measurement of the cavity transmission could be integrated long enough to overcome noise in the measurement signal. However, the spontaneous qubit decay rate γ causes qubit transitions, which prevents us to reach arbitrary large measurement accuracy (Blais *et al.*, 2004).

---

[5] A microwave signal is described by a complex amplitude S with amplitude and phase in polar coordinates, or equivalently, with in-phase $I = \Re(S)$ and quadrature $Q = \Im(S)$ component; compare also Section 3.1.

To measure the qubit state a coherent microwave drive with frequency ν_m is applied to the input of the resonator, and the complex amplitude of the signal transmitted through the resonator is detected. The measurement frequency ν_m is chosen to maximize the contrast in either one of the quadratures or both, such as the contrast marked with the green arrows in Figure 2.6(a,b). Typically, we perform a pulsed qubit state read-out for which the microwave drive is switched on at $t = 0$ like a step function. The step function has a bandwidth that is much larger than $\kappa/2\pi$ of the resonator, the rate (here $\approx 4.8\,\mathrm{MHz}$) at which the resonator is populated from the pulsed drive. Input-output theory provides the exact rise time and ringing of the resonator field due to the limited bandwidth of the resonator. Furthermore it states that the output field of the resonator in mode $\hat{a}'(t) = \sqrt{\kappa}\,\hat{A}(t) - \hat{a}'_\mathrm{in}(t)$ is a linear combination of the resonator field $\hat{A}$ and $\hat{a}'_\mathrm{in}$ (Gardiner and Collett, 1985; Walls and Milburn, 2008; Bianchetti *et al.*, 2009; da Silva *et al.*, 2010), where $\hat{a}'_\mathrm{in}$ is incident onto the output of the resonator and ideally in the vacuum state. The quadratures, which are directly proportional to real and imaginary part of the itinerant microwave field $\hat{a}'(t)$, are measured using a linear detection chain, which is discussed thoroughly in Chapter 3. During linear amplification within the detection chain vacuum and thermal fluctuations are necessarily added to the measurement signal. To cancel that noise, which is often much larger than the itinerant microwave field, typically the ensemble average of repeated experiments are analyzed. A measurement example of a pulsed ensemble averaged qubit state read-out is shown in Figure 2.6(c,d). For the blue trace we prepared the qubit in the ground state $|g\rangle$, and for the red trace we prepared the qubit in the excited state $|e\rangle$ immediately before applying the read-out pulse. The first rise of the trace marks the point in time, where we have switched *on* the measurement drive. The traces of the ground state $|g\rangle$ quickly approach the steady-state amplitude of the two quadratures. The trace for $|e\rangle$ is different, since the qubit *spontaneously* decays from the excited state $|e\rangle$ into the ground state $|g\rangle$ by the emission of a photon, a process commonly known as spontaneous emission. For a single read-out the transmission first approaches the steady-state amplitude of the two quadratures corresponding to $|e\rangle$ (dashed line), then the qubit decays and the transmission approaches the amplitude of the two quadratures corresponding to $|g\rangle$. Thus, the red trace is the average of such traces where the decay time of the qubit is exponentially distributed with rate γ (Siddiqi *et al.*, 2006). The expected form of the ensemble averaged read-out signals (lines) are the solution of the cavity Bloch equations (Bianchetti *et al.*, 2009).

When an arbitrary superposition state $|\psi\rangle$ is prepared and then measured, the area between this ensemble average and the ground state trace is a measure for the expected value $\langle\hat{\sigma}_z\rangle = \langle\psi|\,\hat{\sigma}_z\,|\psi\rangle$, and consequently the excited state population $|c_e|^2$. Section 2.4.2 describes how the measurement scheme above can be used to measure the expectation values $\langle\hat{\sigma}_x\rangle$ and $\langle\hat{\sigma}_y\rangle$. Note that using similar techniques the $|f\rangle$ state population of the transmon can be measured (Bianchetti *et al.*, 2010), as well as the states of several qubits in a single resonator by a joint read-out (Filipp *et al.*, 2009).

Of note, recent developments in circuit QED made also single-shot read-out (Siddiqi *et al.*, 2004; Astafiev *et al.*, 2004; McDermott *et al.*, 2005; Steffen *et al.*, 2006; Gambetta *et al.*, 2007; Mallet *et al.*, 2009; Lang, 2009; Vijay, Slichter, and Siddiqi, 2011) of qubit states possible. Hereby, different approaches are used such as using bifurcation amplification (Mallet *et al.*, 2009; Vijay, Devoret, and Siddiqi, 2009), using qubit induced Jaynes-Cummings nonlinearities (Boissonneault, Gambetta, and Blais, 2010; Reed *et al.*, 2010), or implementing quantum limited linear amplifiers [see Eichler and Wallraff (2014) and references therein].

2.4.2 Qubit Control

Not only the read-out but also the control of the qubit state is very important, e.g. to actively run a quantum information protocol. Here, we describe how microwave irradiation close to the qubit frequency $\tilde{\omega}_\mathrm{a}$ is used to coherently control the state $|\psi\rangle$ of a qubit (Blais *et al.*, 2004). The microwave irradiation is either applied via the resonator or the charge gate line, a coplanar waveguide that selectively couples capacitively to the transmon; compare Figure 2.3. In the dispersive regime, a drive tone close to the qubit frequency rotates the qubit state effectively by

$$\hat{H}^\mathrm{d} = \tfrac{1}{2}\hbar\varDelta_\mathrm{d}\,\hat{\sigma}_z + \tfrac{1}{2}\hbar\varOmega_\mathrm{R}\,\hat{\sigma}_{xy}\ , \tag{2.6}$$

here described in the frame rotating at the carrier frequency ω_c of the drive (Blais *et al.*, 2007). Here, $\varDelta_\mathrm{d} = \tilde{\omega}_\mathrm{a} - \omega_\mathrm{c}$ is the detuning of the drive from the qubit frequency and $\varOmega_\mathrm{R}$ is the Rabi frequency and proportional to the microwave drive amplitude ϵ. The operator $\hat{\sigma}_{xy} = \hat{\sigma}_x\cos\phi + \hat{\sigma}_y\sin\phi$ depends on the phase ϕ of the drive, and can be chosen to either be the Pauli x-operator $\hat{\sigma}_x = |g\rangle\langle e| + |e\rangle\langle g|$, the Pauli y-operator $\hat{\sigma}_y = i(|e\rangle\langle g| - |g\rangle\langle e|)$ or any rotation operator between the two.

The coherent control of the qubit state is illustrated on the Bloch sphere in Figure 2.7(a). An arbitrary qubit state can be written as $|\psi\rangle = c_g\,|g\rangle + c_e\,|e\rangle$, where $c_g, c_e \in \mathbb{C}$ and $|c_g|^2 + |c_e|^2 = 1$. The two coefficients can be represented as a vector pointing onto the unit sphere[6], and the qubit state is conveniently rewritten as $|\psi\rangle = \cos(\theta/2)\,|g\rangle + e^{i\phi}\sin(\theta/2)\,|e\rangle$, where $\theta, \phi \in \mathbb{R}$. If the detuning $\varDelta_\mathrm{d}$ in

---

[6] Since typically only relative phases between several qubits but not the global phase factor can be detected, the global phase is typically dropped and chosen such that $c_g \in \mathbb{R}$.

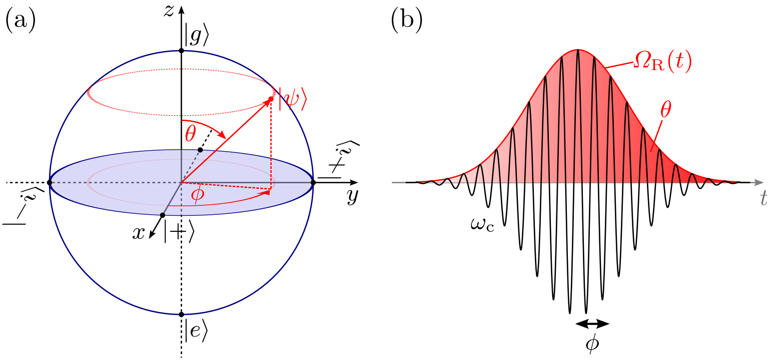

Figure 2.7: Bloch sphere and qubit control. (a) Bloch sphere representation of a qubit state $|\psi\rangle = \cos(\theta/2)\,|g\rangle + \sin(\theta/2)e^{i\phi}\,|e\rangle$. The basis states $|\pm\rangle = (|g\rangle \pm |e\rangle)/\sqrt{2}$ of the $\hat{\sigma}_x$ operator are the intersection points of the Bloch sphere with the x-axis, while the basis states of the $\hat{\sigma}_y$ operator $|\pm i\rangle = (|g\rangle \pm i\,|e\rangle)/\sqrt{2}$ are those with the y-axis. (b) Gaussian shaped resonant qubit pulse with controlled phase ϕ.

the first term of Equation (2.6) is non-zero, the qubit state precesses with rate $\varDelta_\mathrm{d}$ around the z-axis described by the angle ϕ; compare solid red circle in Figure 2.7(a). The second term rotates the qubit state around a ϕ-dependent axis in the xy-plane which increases the Rabi angle θ at rate $\varOmega_\mathrm{R}$.

Specific single-qubit operations which are used later in the text are: (i) the σ_{xy}-gate that performs a $\theta = \pi$ rotation about a given axis in the xy-plane. It is referred to as a π-pulse on the qubit, and prepares a qubit starting from the ground state $|g\rangle$ into the excited state $|e\rangle$. (ii) the $\frac{\pi}{2}$-pulse about an axis in the xy-plane with $\theta = \pi/2$ that prepares a superposition state $|\psi\rangle = (|g\rangle + e^{i\phi}\,|e\rangle)/\sqrt{2}$ when the qubit is initially in the ground state $|g\rangle$. To perform such rotations, we apply a short microwave pulse to the qubit as sketched in Figure 2.7(b). The carrier frequency of the pulse is ω_c and its phase ϕ defines the rotation axis in the xy-plane. The integral over the time-dependent Rabi rate $\varOmega_\mathrm{R}(t)$ over the whole pulse duration (red shaded area) determines the Rabi angle $\theta = \int \Omega_{\mathrm{R}}(t)\,\mathrm{d}t$. Notably, any desired single-qubit gate can be implemented with the control of ϕ, θ, and Δ_{d}.

In Figure 2.7(b), the Rabi pulse $\Omega_{\mathrm{R}}(t)$ has a Gaussian envelope with standard deviation σ and thus is also a Gaussian centered around ω_{c} in its spectral representation. The pulse has a finite bandwidth $\sim 1/\sigma$ and its spectral content decreases monotonically away from ω_{c} which is in contrast to, for example, a square pulse. This has to be taken into account when performing gates on qubits to avoid driving the resonator or transitions to higher transmon levels that are within the bandwidth of the qubit pulse. Typically, the Gaussian pulses used in this thesis' experiments have standard deviations of a few ns. To further improve pulse fidelities for very short pulses, we use a modified Gaussian pulse, a so-called derivative removal by adiabatic gate (DRAG). Hereby, the $|f\rangle$ state of the transmon is only temporarily populated during the pulse (Motzoi *et al.*, 2009; Gambetta *et al.*, 2011; Chow *et al.*, 2010; Lucero *et al.*, 2010); see Baur (2012) for a detailed description and calibration of this gate.

In Section 2.4.1 it was described that the measurement of the resonator in the dispersive regime projects the qubit into $|g\rangle$ or $|e\rangle$ and the ensemble average returns the expectation value $\langle\hat{\sigma}_z\rangle = \langle\psi|\,\hat{\sigma}_z\,|\psi\rangle$. With the single-qubit gates at hand, we are able to measure in any basis. To measure in the $\hat{\sigma}_x(\hat{\sigma}_y)$ basis, we apply a $\frac{\pi}{2}$-pulse about the y-(x-)axis just before the start of the measurement. Thus, the former x-axis is now the z-axis and the ensemble average returns $\langle\hat{\sigma}_x\rangle$. Similarly, any axis can be chosen as measurement basis. This allows us to tomographically reconstruct the density matrix ϱ, for which minimally the three expectation values $\langle\hat{\sigma}_z\rangle, \langle\hat{\sigma}_x\rangle, \langle\hat{\sigma}_y\rangle$ are measured to extract the coordinates of density matrix ϱ in the Bloch sphere as demonstrated for the first time in superconducting circuits by Steffen *et al.* (2006).

2.5 On-Chip Beam Splitter

Consider the chip presented by Figure 2.3, of which all elements have been discussed except the on-chip beam splitter shown in red. In

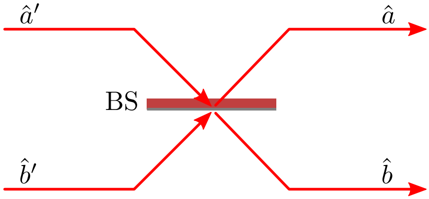

Figure 2.8: Balanced beam splitter (BS) with two inputs modes $\hat{a}'$ and $\hat{b}'$, and two output modes $\hat{a}$ and $\hat{b}$.

this section, I derive the quantum-mechanical beam splitter operation and explain the working principle of the 90°-hybrid beam splitter shown on the sample (Pozar, 2011). The beam splitter is used in this thesis for both Hanbury Brown and Twiss (HBT)-like detection and Hong, Ou, and Mandel (HOM) interference, as outlined in Chapter 1. Therefore, I further describe mathematically the use of the beam splitter operation in the HBT setup and the entanglement generation in HOM two-photon interference.

In the optical frequency domain a beam splitter can be implemented by a half-silvered mirror as shown in Figure 2.8. A beam splitter is a four port device with two input modes $\hat{a}'$ and $\hat{b}'$, and two output modes $\hat{a}$ and $\hat{b}$. In the case that there is incoming radiation only through mode $\hat{a}'$ for a balanced (50/50) beam splitter half of the radiation power is reflected into output mode $\hat{a}$ and the other half is transmitted into mode $\hat{b}$. Similarly, any radiation in the second input mode $\hat{b}'$ is fifty-fifty transmitted and reflected. While the former fulfills energy conservation in the ideally lossless device, unitarity of the beam splitter transformation is ensured by phase changes occurring at reflection and transmission, which depend on the specific implementation of the beam splitter. For simplicity, we assume that there is a phase shift of π upon reflection from mode $\hat{b}'$ into $\hat{b}$, and that there is no phase shift for the other three possible paths[7]. With the phase factor $e^{i\pi} = -1$, the complete beam splitter transformation reads

---

[7] Here, a phase shift of π upon reflection at a optically higher dense medium and no phase shifts upon reflection at the optically less dense medium or upon transmission as deduced by the Fresnel equations.

$$\begin{pmatrix} \hat{a} \\ \hat{b} \end{pmatrix} = \frac{1}{\sqrt{2}} \begin{pmatrix} 1 & 1 \\ 1 & -1 \end{pmatrix} \begin{pmatrix} \hat{a}' \\ \hat{b}' \end{pmatrix} . \tag{2.7}$$

With this choice of phases the transformation matrix is real valued.

A beam splitter operation in the microwave frequency range is implemented by the network of waveguides shown in red in Figure 2.3. Such a network is referred to as a quadrature hybrid or 90°-hybrid (Pozar, 2011; Frey, 2008). Four $\lambda/4$ sections of waveguide with impedances $Z_0 = 50\,\Omega$ and $Z_1 = Z_0/\sqrt{2}$ realize the beam splitter. The different impedances at the T-junctions (compare right inset of Figure 2.3) scatter the correct amount of the field amplitude into each waveguide section, such that there is from each of the input ports destructive interference at the respective other input port and 50 % constructive interference at the two output ports, as discussed below. An incident wave at $\hat{a}'$ picks a phase $\frac{1}{2}\pi$ on the direct path to $\hat{b}'$ and $\frac{3}{2}\pi$ on the clockwise path. Due to the phase difference of π, the two waves of equal amplitudes at port $\hat{b}'$ interfere destructively, so no radiation from $\hat{a}'$ exits the beam splitter on port $\hat{b}'$. Similarly, the incident wave picks a phase $\frac{1}{2}\pi$ on the direct path to $\hat{a}$ and $\frac{3}{2}\pi$ on the counterclockwise path. In contrast to the destructive interference case, however, the amplitude on the direct path is larger than on the counterclockwise path, such that the interference results in an amplitude of $1/\sqrt{2}$ and the phase factor $e^{i\pi/2} = i$ of the direct path with larger amplitude. For the output $\hat{b}$ both paths pick a phase π and thus interfere constructively to an amplitude of $1/\sqrt{2}$ and a phase factor of $e^{i\pi} = -1$. Since the waveguide network is symmetric, the same arguments as above hold for an incident wave at the second input $\hat{b}'$. In summary, we get the unitary beam splitter transformation

$$\begin{aligned} \hat{a} &= \tfrac{1}{\sqrt{2}}(\,i\,\hat{a}' - \hat{b}') & \qquad \hat{a}^\dagger &= \tfrac{1}{\sqrt{2}}(-i\,\hat{a}'^\dagger - \hat{b}'^\dagger) \\ \hat{b} &= \tfrac{1}{\sqrt{2}}(-\hat{a}' + i\,\hat{b}') & \qquad \hat{b}^\dagger &= \tfrac{1}{\sqrt{2}}(\,-\hat{a}'^\dagger - i\,\hat{b}'^\dagger)\,, \end{aligned} \tag{2.8}$$

which is equivalent to the beam splitter model in Equation (2.7) up to constant phase shifts at the four ports (Pozar, 2011). Note that different beam splitter architectures exist, such as the 180°-hybrid or the Lange coupler (Pozar, 2011).

In the present thesis, the beam splitter is used for two purposes: (i) to experimentally demonstrate the single-photon character of a radiation source in an HBT-like setup and (ii) to demonstrate HOM two-photon interference at the beam splitter. The latter is discussed in the paragraph that follows the next one.

Hanbury Brown and Twiss (1956) developed an apparatus to measure photon correlations in two beams of light originally used in astronomy. In quantum optics such intensity interferometers are heavily used to demonstrate by means of a beam splitter that a radiation source emits single-photons. For this, the source under test shall radiate into the first beam splitter input $\hat{a}'$ while the second input $\hat{b}'$ is left in the vacuum state. I denote the input state by $|n'_a m'_b\rangle$ where n and m are the number of photons in mode $\hat{a}'$ and $\hat{b}'$ respectively, and the state $|n_a m_b\rangle$ for the number of photons n and m in the output modes $\hat{a}$ and $\hat{b}$. Suppose now, there is a single-photon in the beam splitter input. Thus, we get the following state at the beam splitter outputs:

$$|1'_a 0'_b\rangle = \hat{a}'^\dagger |00\rangle = \tfrac{1}{\sqrt{2}}(i\,\hat{a}^\dagger - \hat{b}^\dagger)\,|00\rangle \simeq \tfrac{1}{\sqrt{2}}(|1_a 0_b\rangle + i\,|0_a 1_b\rangle)\,,$$

where we have used Equation (2.8) and dropped the global phase factor i in the last step. This corresponds to a quantum superposition of a single-photon in either one of the beam splitter outputs $\hat{a}$ and $\hat{b}$, whereby the respective other output is in the vacuum state. This is different when there are two photons in the beam splitter input:

$$|2'_a 0'_b\rangle = \tfrac{1}{\sqrt{2}}\hat{a}'^\dagger \hat{a}'^\dagger\,|00\rangle \simeq \tfrac{1}{2}(|2_a 0_b\rangle - |0_a 2_b\rangle + i\sqrt{2}\,|1_a 1_b\rangle)\,,$$

which gives us a 50 % probability to detect one photon in each of the beam splitter outputs[8]. Thus, if one demonstrates the absence of photons simultaneously in both outputs, then there are never multiple photons at the beam splitter input. Chapter 3 describes how we rule out the $|1_a 1_b\rangle$ state using linear detection. For the experiments discussed in Chapters 4 and 5 the beam splitter is used in the above discussed HBT-like setup where the second beam splitter input port is left in the vacuum state.

---

[8] A global phase factor $(i)^2 = -1$ is dropped.

The beam splitter can also be used to create spatial entanglement of a two-photon state. To do so, single-photons are sent into both input ports of the beam splitter. If the two photons are indistinguishable, i.e. have the same carrier frequency, arrive at the same time, and their wave packet has the same shape (temporal mode), the state at the beam splitter output is:

$$|1'_a 1'_b\rangle = \hat{a}'^\dagger \hat{b}'^\dagger |00\rangle \simeq \tfrac{1}{\sqrt{2}}(|2_a 0_b\rangle + |0_a 2_b\rangle)\,,$$

which means that the two photons coalesce into a photon pair in either one of the beam splitter outputs[9]. This is known as the HOM effect (Hong, Ou, and Mandel, 1987). There is no state $|1_a 1_b\rangle$ with one photon in each output.

This is in contrast to distinguishable photons. For example, two photons are distinguishable, if the two photons impinge at very different times (arrival time difference much larger than the wave packed duration) at the beam splitter, or the two photons have different frequencies. In such a case we can describe the input state by $|n'_a n'_a, m'_b m'_b\rangle$ with the four photon numbers n, n, m and m in the modes $\hat{a}'$ and $\hat{b}'$, where the two colors shall denote the distinguishable property here exemplary blue and red photons. The output state is described equally. Suppose now two distinguishable photons at the two beam splitter inputs, e.g. in mode $\hat{a}'$ a blue and in $\hat{b}'$ a red photon[10]:

$$\begin{aligned} |1'_a 0'_a, 0'_b 1'_b\rangle &= \hat{a}'^\dagger \hat{b}'^\dagger |00,00\rangle = \tfrac{1}{2}(i\,\hat{a}^\dagger - \hat{b}^\dagger)(-\hat{a}^\dagger + i\,\hat{b}^\dagger)\,|00,00\rangle \\ &\simeq \tfrac{1}{2}(|1_a 1_a, 0_b 0_b\rangle - i\,|1_a 0_a, 0_b 1_b\rangle + i\,|0_a 1_a, 1_b 0_b\rangle + |0_a 0_a, 1_b 1_b\rangle)\,. \end{aligned}$$

Thus, there is a 50 % chance to find one photon in both beam splitter outputs. The first observation of the above discussed HOM two photon interference in the microwave frequency domain is presented in Chapter 6.

---

[9] A global phase factor $-i$ is dropped.

[10] A global phase factor $-i$ is dropped.

2.6 Experimental Setup

In this section I discuss the fundamental concepts of the experimental setup used for all presented measurements. Typically, circuit QED devices to date are cooled down to milli Kelvin temperatures in dilution refrigerators to avoid thermal excitations of the system. I will discuss how the circuit QED device is mounted, and then continue to discuss various types of control lines and connections to room temperature electronics.

2.6.1 Thermal Radiation and Dilution Refrigerator

Cryogenic temperatures are needed to bring the superconductors on the circuit QED device below their critical temperature ($T_\mathrm{c} \approx 1.2\,\mathrm{K}$ for aluminum; $T_\mathrm{c} \approx 9.2\,\mathrm{K}$ for niobium) so that they are lossless, and to ensure that Cooper pairs of electrons form a macroscopic wave function. Even lower temperatures are required due to thermal (Johnson-Nyquist) noise. The thermal population of an electromagnetic mode at frequency ν and temperature T is

$$\langle n \rangle = \frac{1}{e^{h\nu/k_\mathrm{B}T} - 1} \tag{2.9}$$

given by Bose-Einstein statistics, where k_B is the Boltzmann constant (Pozar, 2011). For optical frequencies this quantity is close to zero at room temperature. However, for relevant transition and resonance frequencies in the microwave frequency domain, e.g. $\nu \sim 7\,\mathrm{GHz}$ (typical resonator frequency), and $T = 95\,\mathrm{mK}$ (typical effective temperature) it is already as large as $\langle n \rangle \sim 3\,\%$ thermal excitation. Thus, circuit QED devices are mounted in dilution refrigerators with typical temperatures of 10 to $40\,\mathrm{mK}$. Note that the base temperature is a lower bound, since we need connections to room temperature and other control and detection lines, which may cause additional heat load. Though we make an effort to isolate the sample from thermal radiation in these connections (see later in this section) the isolation cannot be made perfect, and so there are thermal populations of some percents. The corresponding effective temperature is thus typically tens of mK higher than the base temperature due to residual electromagnetic noise in the connections (Fink *et al.*, 2010). Up to now most protocols in pulsed experiments use the quantum-mechanical ground state $|g\rangle$ as initial state. Therefore, it is important that the thermal population of the circuit QED device is as low as possible.

In Figure 2.9(a) the dilution refrigerator[11] (cryostat) is shown, in which the experiments of the present thesis were performed. Here, all shields are unmounted to show the inner parts of the cryostat. The cryostat has six temperature stages which are gradually cooled from room temperature (top) down to the base temperature of 20 mK (base plate). There are four cylindrical shields that protect the inside of the cryostat from thermal radiation present in free space at room temperature. Each shield is thermalized at one of the temperature stages of the cryostat and the shields are arranged in an onion-like structure, except that the layers do not touch each other. Hereby, the base temperature stage is the heart of the onion, and the shields from low to high temperatures are the inner and outer layers of the onion, as indicated in Figure 2.9(a). Thus, each shield encloses any colder part of the cryostat and effectively absorbs or reflects all radiation from the higher temperature stage. Therefore, all components within the cryostat are usually mounted just below the plate to which they thermalize. Components are thermalized to the connected plate via copper connections. Everything within the outermost shield, the enclosure of the cryostat, is evacuated since residual gas creates thermal leaks between the various temperature stages and, thus, increases the heat load onto the low temperature plates.

This cryostat relies on two different refrigeration techniques: a pulse tube refrigerator for the 50 K and 4 K plates, and the dilution refrigerator for the lower temperature stages. The pulse tube cooler is based on a closed-loop refrigerant expansion cycle, where the refrigerant gas is pure helium gas (VeriCold, 2008). The expansion cycles take place in two *cold heads* mounted in the inner of the cryostat, where the compressed refrigerant is periodically expanded adiabatically to remove the heat from the system. With that the attached plates are

---

[11] VeriCold Technologies Cryofree™ DR200-10 (VeriCold, 2008).

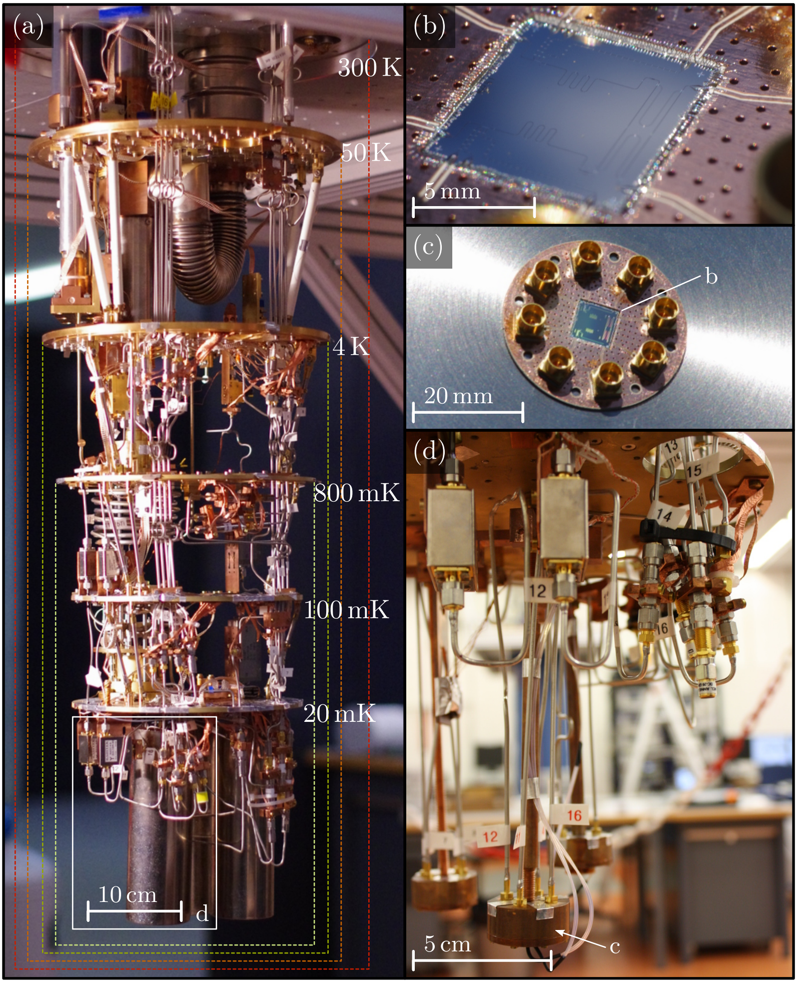
(a)
300 K
50 K
4 K
800 mK
100 mK
20 mK
10 cm
d
(b)
5 mm
(c)
b
20 mm
(d)
13
15
14
12
16
12
16
5 cm
c

Figure 2.9: Experimental setup in the cryostat (a), dashed lines indicate the positions of thermal shields. (b) Sample bonded to PCB. (c) PCB with SMP connectors for in- and output. (d) Sample box on sample holder, magnetic shields from (a) are unmounted.

cooled to cryogenic temperatures of about 50 K and 4 K; compare Figure 2.9(a). The dilution refrigerator is an independent closed-loop system containing a mixture of ^{3}He/^{4}He. The base temperature of the cryostat is achieved in the *mixing chamber*, where a ^{3}He-rich liquid helium phase (concentrated phase) floats on top of a ^{3}He-poor liquid helium phase (dilute phase). Here, heat is extracted from the system by the ^{3}He evaporation from the concentrated phase through the phase boundary into the dilute phase. The ^{3}He-poor liquid helium phase passes through a connection into a second chamber called *still* at the 800 mK plate. In this chamber ^{3}He is evaporated into the gas phase by pumping with an external turbo-molecular pump. The cycle is closed by compressing the gas back into the dilution unit, where it is pre-cooled and liquefied in the 800 mK and 100 mK stage, before it is fed into the mixing chamber to the concentrated phase again (VeriCold, 2008).

2.6.2 Sample Mount and Magnetic Shielding

The circuit QED chip, such as the one shown in Figure 2.3, is glued into a printed circuit board (PCB) as shown in Figure 2.9(b). The PCB acts as an interface between the coplanar waveguides on the chip and the conventional coaxial cables in the cryostat. Similar to the waveguides on the chip the PCB has coplanar waveguides on a larger scale. Respective center conductors and ground planes on chip and PCB are connected via aluminum wire bonds; compare silver lines in Figure 2.9(b). SMP plugs are soldered onto the PCB to connect the PCB waveguides to the coaxial ones of the cryostat; compare Figure 2.9(c). To avoid reflections of microwave radiation or unwanted resonances due to impedance mismatches, both coplanar waveguides and SMP plugs as well as the connected coaxial cables are designed to have impedance close to $Z_0 = 50\,\Omega$.

The completed PCB is connected via the SMP plugs to coaxial cables and tightly enclosed by the sample box made from oxygen-free copper; see Figure 2.9(d). A vertical spacer avoids unwanted resonances that are not perpendicular with the chip (Marx, 2009). Additionally, the sample box provides a good thermal contact for effective cooling. Experiments of Córcoles *et al.* (2011) experienced a reduced qubit decay rate through shielding the sample from external radiation by covering the sample holder with an absorptive medium. However, similar experiments suggest that our sample holder without absorptive medium already effectively shields residual external radiation enough and the qubit decay rate is dominated by other decay processes (Peterer, 2012). Below the sample box we mount up to four superconducting miniature coils, with which static magnetic fields are applied to generate magnetic flux through the SQUID-loop of the transmon qubits; compare Section 2.2.2. The sample box itself is then mounted with a good thermal contact below the base plate of the cryostat, as shown in Figure 2.9(d).

Because of the sensitivity of the transmon to varying magnetic flux through the SQUID-loop the complete sample holder is enclosed from below by two cylindrical magnetic shields; compare Figure 2.9(a). These are made from a low-temperature optimized µ-metal, and effectively shield uncontrolled external magnetic fields at the sample box.

2.6.3 Cabling and Control Signal Generation

To control the circuit QED device using room-temperature electronics, we install coaxial microwave cables [compare the silver lines in Figure 2.9(a)] and superconducting twisted pair cables from the corresponding instruments down to the base plate of the cryostat. The cables are installed in such a way that heat load to the sample is minimized. Furthermore, the device should not be irradiated through the coaxial cables with thermal noise generated at room temperature or at the other temperature stages of the cryostat. Hence, it is necessary to take into account the finite cooling power at each temperature stage. In addition, cables may have specific purposes, and so different strategies are pursued for the connections through the cryostat, shown in Figure 2.10 and explained in the following.

Superconducting miniature coils underneath the sample box are used to generate magnetic flux through the SQUID-loop of the transmon for tuning its transition frequency ν_a at slow timescales. Using

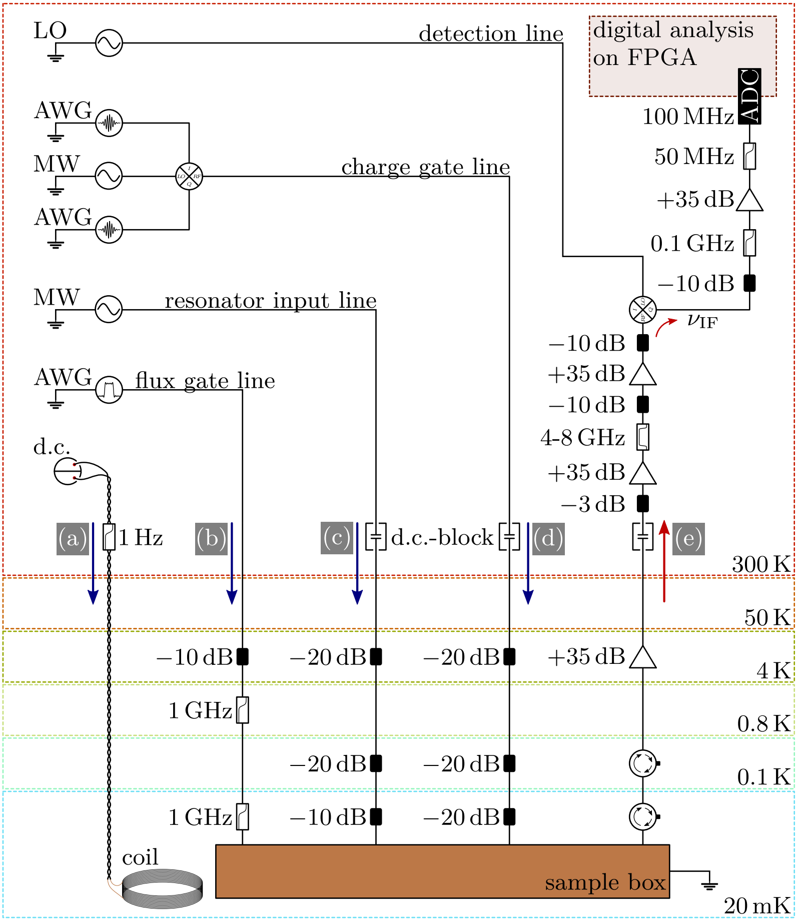
LO
detection line
digital analysis on FPGA
ADC
100 MHz
50 MHz
+35 dB
0.1 GHz
−10 dB
AWG
MW
AWG
charge gate line
MW
resonator input line
ν_{IF}
−10 dB
+35 dB
−10 dB
4-8 GHz
+35 dB
−3 dB
AWG
flux gate line
d.c.
(a)
1 Hz
(b)
(c)
d.c.-block
(d)
(e)
300 K
50 K
−10 dB
−20 dB
−20 dB
+35 dB
4 K
1 GHz
0.8 K
−20 dB
−20 dB
0.1 K
1 GHz
−10 dB
−20 dB
coil
sample box
20 mK

Figure 2.10: Schematic of experimental setup with associated temperature stages. The different line types illustrate: (a) d.c. magnetic flux bias; (b) ns-timescale magnetic flux pulses; (c) resonator and read-out microwave drive; (d) arbitrarily shaped microwave qubit control pulses; (e) linear amplification of measurement microwaves. See Glossary on page 139 for a description of the symbols.

multiple coils we are able to individually control the magnetic flux through different SQUID-loops on the chip. Each coil is connected to room temperature through a twisted pair cable made from superconducting wires; compare Figure 2.10(a). Outside the cryostat, a self-made resistive low-pass filter with cut-off frequencies in the order of 1 Hz converts a battery based voltage source into a d.c. current source. Additionally, the coil itself filters out fast oscillating currents. Of note, the d.c. current does not deposit heat in the cryostat below the 4 K stage, because wires of coil and twisted pair are superconducting. Hereby, it is important to make good superconducting contacts when soldering the superconducting wires, i.e. we do not use plugs here. Further, a superconductor is a good thermal isolator, so that the heat load between temperature stages comes from the material in which the superconductor is embedded.

For microwave frequencies on the order of a few GHz we use coaxial cables which are connected predominantly using SMA connectors. Both the cables and the SMA connectors have an impedance of $Z_0 = 50\,\Omega$. The microwave pulses and signals sent through the input cables Figure 2.10(b-d) are generated by microwave signal generators[12] at room temperature. These signals inevitably include Johnson-Nyquist noise generated by a resistor with two terminals which transfers the power spectral density $h\nu \langle n \rangle$ given by Equation (2.9) in an impedance matched network (Pozar, 2011). However, the used microwave instruments are able to generate orders of magnitude larger signals, such that the signal to noise ratio can easily be made sufficiently large (typically $> 148\,\mathrm{dBc/Hz}$ broadband noise for the here used continues microwave generation). Each $-20\,\mathrm{dB}$ attenuator in an input line [compare Figure 2.10(b-d)] transmits only 1 % of the incoming radiation and adds 99 % of thermal noise $h\nu/(e^{h\nu/k_\mathrm{B}T} - 1)$ [compare Equation (2.9)], where T is the physical temperature of the attenuator (Pozar, 2011). Using a chain of attenuators thermalized at the various temperature stages of the cryostat, one can effectively achieve noise levels close to the vacuum level.

---

[12] Agilent Technologies PSG E8257D Analog Signal Generator and Tektronix AWG5014 Arbitrary Waveform Generator

The attenuators also thermalize the center conductor of the coaxial cables by the resistive link between outer and center conductor. Being an insulator the dielectric in coaxial cables is typically a bad thermal conductor, and thus would thermalize ineffectively without the attenuators. The coaxial cables connecting two stages are made from stainless steel to keep the heat load between two temperature stages small. These have a lower thermal conductivity than copper cables. However, since copper has a better conductance, we use these for the connections to the chip within base temperature and at room temperature, where the connections do not involve temperature gradients.

In addition to static flux control of SQUIDs we apply ns-timescale magnetic flux pulses generated by current pulses through the flux gate line; compare left inset of Figure 2.3 and Figure 2.10(b). To apply magnetic flux through the SQUID-loop in the order of a flux quantum Φ_0, we send mA currents through the flux gate lines. Since the power dissipated in resistive attenuators would exceed the cooling power of the 100 mK stage and base stage, we use low-pass filters. These reflect effectively room temperature noise with frequencies larger than $\sim 1.6\,\mathrm{GHz}$ ($< -40\,\mathrm{dB}$) and allow signals with frequencies up to $\sim 0.78\,\mathrm{GHz}$ ($-1\,\mathrm{dB}$) to pass; compare Figure 2.10(b). The short pulses are generated with an arbitrary waveform generator (AWG) that uses a bandwidth of 500 MHz. However, problems can arise from the filtering, because the generated pulses become distorted. We account for that during the pulse generation as accurate as we know the transfer function of the flux lines, which we calibrate at room temperature but slightly deviates from that after being cooled down.

For the resonator input line and charge gate line we generate typical input signals in the microwave frequency range. For resonator input lines [Figure 2.10(c)] a continuous coherent microwave drive is used, which is digitally modulated[13] if needed, e.g. for qubit state read-out as discussed in Section 2.4.1. Hence, we connect a microwave source directly to the line. The output of the microwave source is modulated by a programmable trigger of the AWG. To manipulate the state of the qubit (see Section 2.4.2) we apply microwave pulses, such as in Figure 2.7(b), to the input of the charge gate line; compare Figures 2.3 and 2.10(d). Signals (I, Q) of an analog output pair generated by an AWG, a microwave source, and an IQ-mixer are used to generate a shaped pulse at a microwave carrier frequency, such as shown in Figure 2.7(b). The signal $I(t) + i\,Q(t)$ generated by the AWG is up-converted to a microwave carrier frequency using the IQ-mixer that multiplies the quadratures with the local oscillator (LO) field of the microwave source. I have developed an automated calibration routine to deal with imperfections of AWG and the IQ-mixer typically occurring in the up-conversion process. The routine calibrates the finite d.c.-offset of each quadrature, the amplitude imbalance between the quadratures, and their imperfect phase difference which is not exactly $\pi/2$ (phase imbalance); see Baur (2012) for a detailed description.

---

[13] The drive is switched between the states *on* and *off* within ns-timescales.

Microwave detection lines [Figure 2.10(e)] are connected to the two beam splitter outputs. Here, I only describe the parts relevant to cryogenic stages and refer to Chapter 3 where the detection principle is discussed in detail. To avoid that noise propagates from the amplifier at the 4 K stage to the sample we use circulators to absorb microwave radiation in the downward direction but pass the measurement signal in the upward direction. A circulator ideally is an impedance-matched, lossless, and nonreciprocal three-port device that directs radiation as indicated by the arrows in the symbol; compare Figure 2.10 (Pozar, 2011). By terminating the third port with a thermally anchored impedance-matched $Z_0 = 50\,\Omega$ resistor, we typically achieve isolations of $\sim 16\,\text{dB}$ and an insertion loss of $\sim 0.5\,\text{dB}$. NbTi superconducting coaxial cables are used instead of stainless steel cables between the two circulators and to the cold amplifier to keep the transmission high while minimizing heat load from the respective higher temperature stage.

2.6.4 Synchronization

All instrumentation in the experimental setup, including microwave sources, AWGs, triggers, and also digital detection electronics, share one common time-base to remain synchronized while performing a measurement which might last several hours. Thus, a certain frequency in that time-base is required to be constant for every instrument, as otherwise, a phase difference would slowly drift which will adversely affect any measurement. In this setup we use a Rubidium atomic clock, which provides multiple 10 MHz reference outputs. We connect all microwave instrumentation, which are consequently *phase-locked* to this reference clock.

To synchronize pulses and measurements in experimental protocols, we use the programmable binary outputs of the AWG to trigger for example the measurement start or the binary modulation of a microwave source output state.

To summarize this chapter, I have introduced the fundamental concepts of circuit QED and the experimental system that was used for the experiments presented in this thesis. I have theoretically described the system, discussed its energy level structure and the dispersive regime where qubit and resonator are decoupled. Further, I have introduced the beam splitter and its use for intensity interferometry and entanglement generation. In the description of the experimental setup, I have skipped the linear detection of the microwave radiation and measurement data analysis methods, which follows in the next self consistent chapter.

3

Quantum Signal Analyzer

In this chapter the detection and the analysis of microwave signals, measured using linear detection, is discussed. We consider a detection process in which the electric *field* (voltage) of the microwave radiation is phase-coherently amplified and then acquired by analog-to-digital conversion. In circuit QED experiments, acquisition of the measurement signals is commonly performed by commercial digitizer boards. Typically, they are used to compute ensemble averages of the digitized field, which are then saved on a computer. Further analysis of the ensemble averages are performed later with computer software. However, to measure incoherent microwave radiation (Houck *et al.*, 2007; Astafiev *et al.*, 2010; Hoffman *et al.*, 2011; Mlynek *et al.*, 2012) and to display unique quantum-mechanical properties in higher order correlations (Bozyigit *et al.*, 2011a; Eichler *et al.*, 2011b,a; Lang *et al.*, 2011; Eichler *et al.*, 2012; Hoi *et al.*, 2012; Menzel *et al.*, 2012; Lang *et al.*, 2013b), either a nonlinear detection or a nonlinear analysis of linearly detected microwave fields is needed. For this purpose, we implemented a novel data analysis approach based on field programmable gate array (FPGA) electronics, which allows a highly parallel and hence fast and efficient signal processing. In this way, signal processing and analysis is performed by the FPGA in real-time before the analyzed data is saved on a computer. Furthermore, real-time signal analysis enables fast feedback (Sayrin *et al.*, 2011; Ristè *et al.*, 2012; Steffen *et al.*, 2013; Ristè *et al.*, 2013), required, e.g., for quantum error correction in the field of quantum information processing. The signal processing and a description of potential data analyses are the topic of this chapter.

In Section 3.1 the detection electronics used to linearly detect the microwave field of interest from the detection chain input to the extraction of its complex amplitude is described. I mathematically describe the detection process in Section 3.2, and illustrate it in the frequency domain in Section 3.3. Further, I present a quantum-mechanical formulation of the linear detection in Section 3.4. In Section 3.5 the detection of averaged power based on the linearly detected fields is addressed. Specific FPGA based analysis applications are described in Sections 3.6 to 3.10. See Appendix A for details about FPGA based data processing, hardware present on the used FPGA board, and a technical overview of the FPGA firmware.

3.1 Heterodyne Detection Chain

Itinerant microwave radiation $S(t)\, e^{i\omega_{\mathrm{d}} t}$ is described by the time-dependent *complex amplitude* $S(t) = I(t) + i\, Q(t)$ defining the envelope of a wave packet with carrier frequency $\omega_{\mathrm{d}}/2\pi$. Here, $I(t) \in \mathbb{R}$ denotes the in-phase and $Q(t) \in \mathbb{R}$ the quadrature component of $S(t)$, which are frequently called *quadratures*. A detection chain is used to measure the complex amplitude $S[t]$ at discretized times t by *demodulating* the microwave from $\omega_{\mathrm{d}}/2\pi$ to $0\,\mathrm{Hz}$ (d.c.). In *homodyne detection* the microwave is demodulated to d.c. before directly recording $S[t]$. In our implementation of *heterodyne detection* a two-step demodulation of the microwave radiation is performed, first to a non-zero *intermediate frequency* $\omega_{\mathrm{if}}/2\pi$ which is recorded using an analog-to-digital converter (ADC), and then digitally to d.c.

In the context of this thesis, the microwave radiation field of interest is generated at cryogenic temperatures. The detection chain consists of several analog microwave components and various digital signal processing stages. Figure 3.1 shows all effective stages. The signal

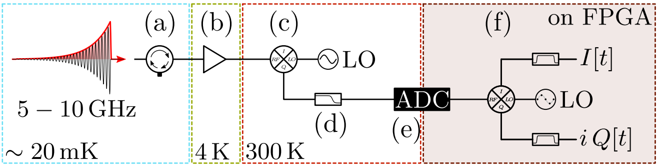

Figure 3.1: Typical simplified representation of a heterodyne detection chain for the acquisition of the complex amplitude $S[t] = I[t] + i\,Q[t]$ of itinerant microwave radiation created at cryogenic temperatures. The detection process consists of the following effective stages: (a) terminated circulator, (b) linear amplification of the electric field, (c) frequency down conversion to ν_{if} by a microwave mixer, (d) anti-aliasing low-pass filter, (e) analog-to-digital conversion, and (f) digital down conversion to d.c. and filtering in FPGA based electronics. See Glossary on page 139 for a description of the symbols.

propagates along a transmission line or coaxial cable with a typical impedance $Z_0 = 50\,\Omega$ through the detection chain from the source to the ADC.

In the first stage of the signal flow, the itinerant microwave radiation, emitted from a source, passes a set of impedance-matched and terminated (Pozar, 2011) circulators or isolators; compare Figure 3.1(a). Thus, the source is isolated from parasitic radiation traveling in backward direction through the detection chain towards the source. Then the microwave radiation is linearly amplified [Figure 3.1(b)] with amplifiers operated both at cryogenic and room temperature. In this process the complex amplitude is scaled by the factor $\sqrt{g}$, where g is the power gain of the amplifier, and thermal noise is added to the signal (Pozar, 2011; da Silva *et al.*, 2010). The amount of noise added in the band of amplification is frequently characterized by the noise temperature T_{n} (Pozar, 2011), which is typically a few Kelvin for commercially available cryogenic high electron mobility transistor (HEMT) based amplifiers. Any loss, that occurs between the source and the first stage of amplification, reduces the total gain of the chain while the added noise remains constant. This results in an increased system noise temperature T_n (Pozar, 2011). Note that much progress has recently been made in realizing and operating quantum limited linear amplifiers; see Eichler and Wallraff (2014) and references therein. With these amplifiers the quantum limit of added noise, set by amplification of (unavoidable) vacuum fluctuations, is achievable (Caves, 1982). Providing also linear amplification these amplifiers can be used similarly, with the advantage of significantly improved signal to noise ratio.

In order to obtain measurable field amplitudes a radiation power on the order of $\sim 0\,\mathrm{dBm}$ is necessary. Since the power of quantum signals at microwave frequencies is on the order of $\sim -140\,\mathrm{dBm}$, a large gain g is required which is typically reached by linearly amplifying the field in multiple stages. However, typical microwave components, in particular amplifiers, perform linearly only below certain input powers, the compression point (Pozar, 2011). To avoid driving any microwave component into compression, we limit the total power (typically mostly defined by the noise) in the detection chain using filtering.

After linear amplification the signal is down converted to an *intermediate frequency* $\nu_\mathrm{if} = \omega_\mathrm{if}/2\pi$ (heterodyne detection) by mixing, i.e. multiplying the amplified signal with a local oscillator of angular frequency $\omega_\mathrm{LO} = \omega_\mathrm{d} \mp \omega_\mathrm{if}$; see Figure 3.1(c). For convenience only negative detunings are discussed here. Heterodyne detection has technical advantages compared to homodyne detection ($\omega_\mathrm{LO} = \omega_\mathrm{d}$) where an IQ-mixer is used to record both quadratures I and Q. Performing homodyne detection it is necessary to calibrate sources of imperfections, which typically occur in IQ-mixing. These are the finite d.c.-offset of each quadrature, the amplitude imbalance between the quadratures, and their imperfect phase difference which is not exactly $\pi/2$ (phase imbalance). Using heterodyne detection we do not suffer from these imbalances as we only use a single quadrature. Additionally, less hardware resources are required. However, a significant drawback is a signal to noise ratio reduced by 50%, as discussed in Section 3.2.

The down converted signal is then digitized by an ADC, which records the voltage $V[t]$; see Figure 3.1(e). The ADC samples the input voltage at a sampling frequency f_s phase-locked to all microwave equipment in the experimental setup. The output is a waveform of digitized voltages $V[t]$ at the discrete points in time $t = nt_\mathrm{s} + t_0$, where $t_\mathrm{s} = 1/f_\mathrm{s}$ is the sampling period, t_0 the start time, and $n \in \mathbb{Z}$. The maximal detection bandwidth is limited to $f_\mathrm{s}/2$, since only frequencies smaller than the Nyquist frequency $f_\mathrm{s}/2$ are correctly identified (Lyons, 2004). Spectral components at frequencies ν larger/smaller than $\pm f_\mathrm{s}/2$ have an *alias* frequency ν' with $-f_\mathrm{s}/2 \leq \nu' < f_\mathrm{s}/2$ that is equivalent with ν under the modulo f_s operation ($\nu' \equiv \nu \mod f_\mathrm{s}$). Therefore, $f_\mathrm{s}/2$ is also referred to as the folding frequency (Lyons, 2004). For this reason the intermediate frequency ν_if in the down conversion described above is chosen to $\nu_\mathrm{if} < f_\mathrm{s}/2$. Analog low-pass filters at the input [see Figure 3.1(d)] suppress spectral components of the signal higher than the Nyquist frequency to avoid aliasing (Lyons, 2004). ADCs, typically used in circuit QED, sample with tens of MHz up to GHz frequencies f_s. The vertical resolution usually ranges from 8 to 16 bits. These digital bits encode the voltage at the input of the ADC in a full scale, i.e. the maximally available peak-to-peak voltage, which is typically of the order of one volt. The total amplification chain discussed above is tailored so that the signal including the noise $V[t]$ is smaller than the full scale of the ADC to prevent clipping and compression. However, the standard deviation of $V[t]$ should be larger than the ADC resolution to avoid discretization errors in averaged quantities. This is usually guaranteed by the presence of the amplifier noise. The effective resolution of averaged quantities is therefore for the applications discussed here not limited by the ADC resolution but the number of averages.

We use FPGA based electronics to process the waveform of sampled voltages $V[t]$. On the FPGA digital signal processing and analysis are (massively) parallelized, and hence we are able to continuously process every sampled voltage $V[t]$ in real-time, as explained in Appendix A.1. In this way, we digitally complete the heterodyne detection performing a digital down conversion (DDC) to d.c. and digital filtering, as depicted in Figure 3.1(f). These two digital steps, described mathematically in the following Section 3.2, allow us to extract the complex amplitude $S[t]$ with a bandwidth of $f_\mathrm{s}/2$.

3.2 Linear Signal Processing

In this section, we mathematically describe the linear signal processing steps outlined as hardware stages in the previous Section 3.1.

Linear amplification increases the magnitude of $S(t)$ by a factor of $\sqrt{g}$ and adds noise to the microwave radiation (da Silva *et al.*, 2010). In the analog down conversion the microwave radiation is effectively multiplied by the complex sinusoid $e^{-i(\omega_\mathrm{d}-\omega_\mathrm{if})t}$ which results in a frequency-shift of the complex amplitude to $\nu_\mathrm{if} = \omega_\mathrm{if}/2\pi$. Thus we get $\sqrt{g}S(t)\,e^{i\omega_\mathrm{if}t}$.

Next, we digitize a single quadrature of this signal. Thus, we gain access to only real valued voltages of the form

$$V[t] = \Re\left(\sqrt{g}S(t)\,e^{i\omega_\mathrm{if}t}\right) = \tfrac{\sqrt{g}}{2}\left(S(t)\,e^{i\omega_\mathrm{if}t} + S^*(t)\,e^{-i\omega_\mathrm{if}t}\right) .$$

This expression illustrates that, at positive frequencies from 0 to $f_\mathrm{s}/2$ in $V[t]$, the spectral content in $S(t)$ from $-\nu_\mathrm{if}$ to $+f_\mathrm{s}/2-\nu_\mathrm{if}$ (first term) is superimposed with its *image*, the complex conjugate spectral content, from $-\nu_\mathrm{if}$ to $-f_\mathrm{s}/2-\nu_\mathrm{if}$ (second term), and vice versa for negative frequencies. Thus, to properly detect $S(t)$, we have to make sure that the spectral content in $S(t)$ is limited to the range between $-\nu_\mathrm{if}$ and $+f_\mathrm{s}/2-\nu_\mathrm{if}$, with a safety margin at the boundaries of the frequency range to prevent that aliasing or analog filter effects distort the signal of interest. Additionally, the superposition with the image implies that we are not able to distinguish noise from positive and negative frequency bands. Hence, in the case of broadband noise that is added by broadband amplification, the signal to noise ratio is effectively reduced by 50% at this point. This could be avoided by the rejection of the undesired image, for example by using an analog image reject mixer (Okean and Kelly, 1977) or by filtering and digitizing both quadratures of the signal.

The digital down conversion frequency-shifts $S(t)$ to d.c. by multiplying $V[t]$ with a digital local oscillator of frequency $-\nu_\mathrm{if} = -\omega_\mathrm{if}/2\pi$:

$$\bar{S}[t] = V[t]\,e^{-i\omega_\mathrm{if}t} = \tfrac{\sqrt{g}}{2}S(t) + \tfrac{\sqrt{g}}{2}S^*(t)\,e^{-i2\omega_\mathrm{if}t} .$$

Finally, a finite impulse response (FIR) filter (Lyons, 2004) is applied to $\bar{S}[t]$ for three purposes: (i) to remove the part of $S^*(t)$

centered around the image carrier frequency $-2\nu_{\text{if}}$; (ii) to remove the quadrature d.c.-offset at $-\nu_{\text{if}}$ that result from both imperfect analog down conversion (the d.c.-offset of a quadrature in *IQ*-mixing) and imperfect analog-to-digital conversion where the reference voltage is not exactly zero volt; (iii) to filter out noise beyond the desired detection band. Mathematically, an FIR filter is realized by the convolution, denoted by $*$, of a signal $\bar{S}[t]$ with a kernel $k[t']$ that represents the filter:

$$S[t] = (\bar{S} * k)[t] \equiv \sum_{t'=0}^{T-t_\text{s}} \bar{S}[t-t']\, k[t']\,, \tag{3.1}$$

where $k[t']$ has N coefficients at $t' = 0, t_\text{s}, 2t_\text{s}, \dots, T - t_\text{s}$ resulting in a total integration time $T = Nt_\text{s}$. For the Dirac delta kernel, with the first coefficient equal to 1 and all others equal to 0, $S[t]$ is equal to the unfiltered complex amplitude $\bar{S}[t]$.

The digitally applied FIR filter defines the detection bandwidth, with which we have determined the complex amplitude $S[t]$ demodulated from the microwave radiation $S(t)\, e^{i\omega_\text{d} t}$ at the input of the detection chain. All steps described so far are linear operations. Hence, the order of operations can be interchanged also with following linear operations such as e.g. time-dependent averaging. Thus it is possible to first average the digitized voltages $V[t]$ and perform the digital down conversion and FIR filtering afterwards, to get the ensemble average of $S[t]$.

3.3 Linear Detection in the Frequency Domain

We schematically illustrate all stages of the heterodyne detection as presented in Sections 3.1 and 3.2 by an exemplary complex amplitude signal $S(t)$ which decays exponentially, as depicted at the input of Figure 3.1. The exponential is a usual characteristic for any spontaneous process, e.g. a single-photon field that exponentially decays out of a cavity (Bozyigit *et al.*, 2011a; Eichler *et al.*, 2011b). The complex amplitude of an exponential decay has a Lorentzian power spectral density (PSD) centered around the demodulation frequency chosen as $\omega_\mathrm{d}/2\pi = 6\,\mathrm{GHz}$ with a FWHM $\kappa/2\pi = 4\,\mathrm{MHz}$, as shown in Figure 3.2(a). The bandwidth of the signal is smaller than $f_\mathrm{s}/2$ and is digitized by a single ADC with a sampling frequency $f_\mathrm{s} = 100\,\mathrm{MHz}$.

The shaded area in Figure 3.2(b) represents the noise, which is added to the microwave signal of interest during linear amplification, above (green) and below (orange) the lower bound of the detection bandwidth. For HEMT based amplification, the noise is approximately white, i.e. frequency independent over the relevant frequency range. Note that typically the noise level is an order of magnitude higher than schematically depicted here, if we consider signals on the order of one photon per $1/\kappa$.

In the down conversion process the spectral content of the signal is shifted from $\omega_\mathrm{d}/2\pi$ to ν_if; compare Figure 3.2(c). We usually choose $\nu_\mathrm{if} = f_\mathrm{s}/4$ which symmetrically distributes the accessible bandwidth of the ADC from d.c. to $f_\mathrm{s}/2$. With that, the green shaded area is now positive and the orange negative frequency noise. Noise at frequencies larger than $f_\mathrm{s}/2$ is suppressed by the analog anti-aliasing low-pass filter. Note that practical filters do not have a completely flat transfer function with infinitely steep edges. Imperfect down conversion (and also digitizing) results in a quadrature d.c.-offset depicted by the red peak at 0 Hz created during analog mixing and digitizing.

A single quadrature of the down converted signal is digitized by the ADC, $V[t]$, the PSD of which is shown in Figure 3.2(d). Due to aliasing, described in Section 3.1, spectral content larger than the Nyquist frequency $f_\mathrm{s}/2$ is folded into the allowed frequency band (Lyons, 2004) between $-f_\mathrm{s}/2$ to $f_\mathrm{s}/2$, shown by the increased noise level at $\pm f_\mathrm{s}/2$ in Figure 3.2(c,d). At this point, we cannot distinguish between signals at positive and negative frequencies; compare Section 3.2. Consequently, one half of the power at negative frequencies appears at the corresponding positive frequencies, and vice versa, which is illustrated pictorially in Figure 3.2(d). The negative frequency noise degrades the signal to noise ratio at ν_if by 50% as positive and negative frequency noise have typically equal power.

The digital down conversion shifts the spectral content by $-\nu_\mathrm{if}$,

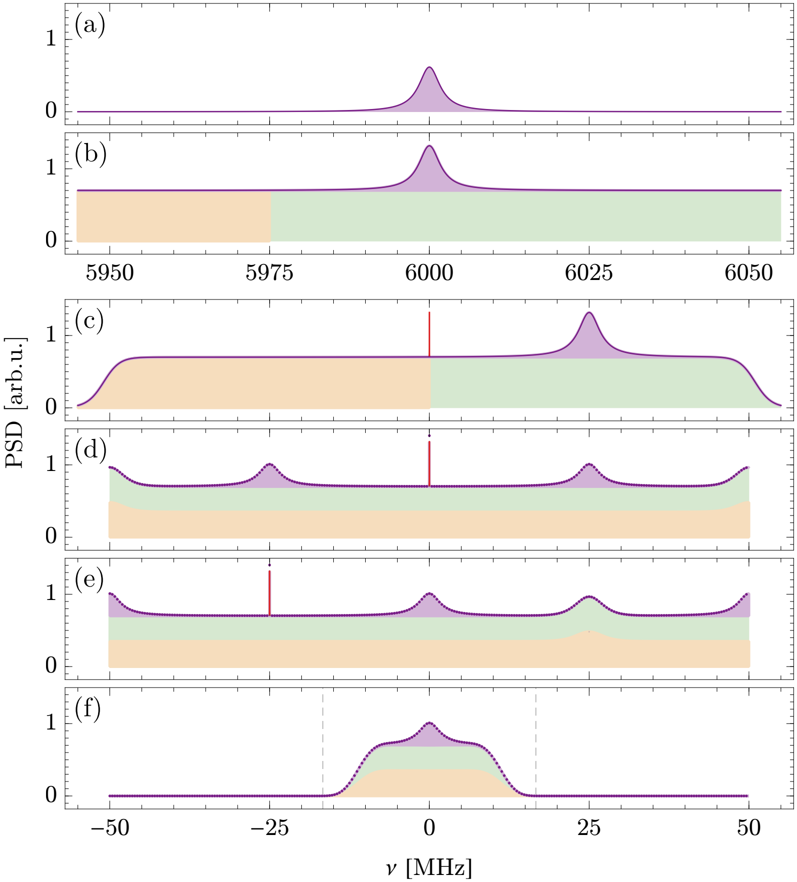

Figure 3.2: Power spectral density (PSD) of signal (purple), noise (green and orange according to their frequency origin), and d.c.-offset (red) after various states of the signal processing: (a) signal of interest, (b) added noise during amplification, (c) analog down conversion to intermediate frequency and analog low-pass filter, (d) digitizing single down converted quadrature, (e) digital down conversion, (f) 25 MHz Chebyshev FIR filter.

compared to the PSD of $\bar{S}[t]$ in Figure 3.2(e), here from 25 to 0 MHz. As a consequence of aliasing, the spectral content is cyclically wrapped around (Lyons, 2004) at $\pm f_\mathrm{s}/2$. Figure 3.2(e) shows the PSD of the demodulated complex amplitude, centered at d.c. Spectral content at frequencies $\nu < -\nu_\mathrm{if}$ and $\nu > \nu_\mathrm{if}$ is filtered out to faithfully extract the complex amplitude. Also the peak at $-\nu_\mathrm{if}$ in the PSD due to the d.c.-offset (red peak) is suppressed using a filter. Otherwise, the extracted complex amplitude would include a strong coherent oscillation with frequency $-\nu_\mathrm{if}$, and the image of the signal of interest modulated with frequency $-2\nu_\mathrm{if}$.

We choose to apply two types of FIR filters to the signal; compare Section 3.2: a N-point square window filter to completely suppress the spectral components at integer multiples of $\pm f_\mathrm{s}/N$, and an FIR filter with N arbitrary coefficients to adjust the detection bandwidth. The square window filter, for which the N filter coefficients are all equal to $1/N$, is a simple FIR filter, also known as a moving average filter (Lyons, 2004). This filter has three main advantages: (i) it requires little resources on the FPGA; (ii) it executes within ns-time scales on the FPGA, and therefore almost only introduces the unavoidable group delay; (iii) it perfectly rejects spectral components originating from the quadrature d.c.-offset and the image carrier frequency $-2\nu_\mathrm{if}$ in the case of $\nu_\mathrm{if} = f_\mathrm{s}/N$. The transfer function of the square window filter has a predetermined shape with a fixed bandwidth, as shown for $N = 4$ in Figure 3.3(a). To implement any other desired transfer functions, we apply an arbitrary FIR filter. The Chebyshev window design method (Lyons, 2004) is used to ensure maximal steepness and good stop band suppression, e.g. < -40 dB and a desired 25 MHz bandwidth (gray) for a limited number of filter coefficients, here 29. Its transfer function (black) is shown in Figure 3.3(b) and, on a linear scale, the PSD of $S[t]$ of the filtered exemplary signal is shown in Figure 3.2(f). Depending on the available resources on the FPGA we implement filters with up to 40 coefficients, which we restrict to symmetric filter coefficients for very limited resources. When perfect rejection of certain spectral components such as $-\nu_\mathrm{if}$, and a customized detection bandwidth is needed, a combination of two filter types can be chosen, as exemplary shown

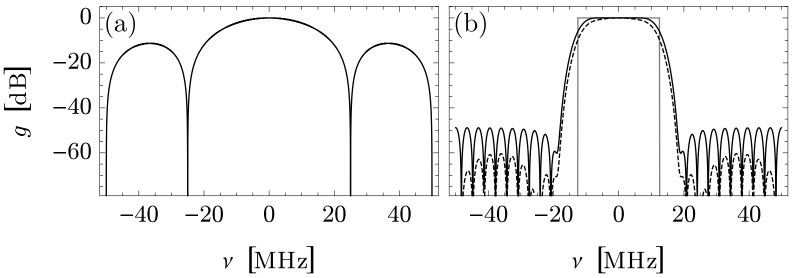

Figure 3.3: Frequency dependent filter gain g of (a) 4-point square window FIR filter, and (b) 29-point Chebyshev FIR filter (black line) and the ideal transfer function for 25 MHz detection bandwidth (gray line). The combination of both filters is shown by the dashed line.

by the dashed line in Figure 3.3(b).

3.4 Operator Formulation of Linear Detection

Next, we formulate the linear detection as presented in Sections 3.1 and 3.2 in terms of quantum-mechanical operators. This formulation keeps the quantum-mechanical characteristics, and thus allows us to assess our measurements based on quantum-mechanical calculations. Further, noise and signal are easy to discriminate in this formulation.

The electric field of interest at the detection frequency ω_d is proportional to $\hat{I}_a \cos(\omega_\mathrm{d} t) + \hat{Q}_a \sin(\omega_\mathrm{d} t) = \Re((\hat{I}_a + i\,\hat{Q}_a) e^{i\omega_\mathrm{d} t})$ (Caves, 1982). Hereby, the in-phase $\hat{I}_a$ and quadrature $\hat{Q}_a$ component operators are commonly defined as:

$$\hat{I}_a = \tfrac{1}{2}(\hat{a} + \hat{a}^\dagger) \qquad\qquad \hat{Q}_a = \tfrac{-i}{2}(\hat{a} - \hat{a}^\dagger)$$

using the photon annihilation and creation operators $\hat{a}$ and $\hat{a}^\dagger$. More convenient than to treat each quadrature separately and to simplify following calculations, we define the quantum complex amplitude $\hat{S}_a$

as

$$\hat{S}_a \equiv \hat{I}_a + i\,\hat{Q}_a = \hat{a}$$

that reduces to the photon annihilation operator $\hat{a}$. Being not hermitian $\hat{S}_a = \hat{a}$ is not an observable and its eigen-values are complex, also explained by the commutation relation $\left[\hat{a}, \hat{a}^\dagger\right] = 1$ for the bosonic field mode. Thus, due to the Heisenberg uncertainty principle, the exact and simultaneous measurement of both quadratures $\hat{I}_a$ and $\hat{Q}_a$ is impossible without introducing at least the Heisenberg uncertainty related to the non-zero commutator $\left[\hat{I}_a, \hat{Q}_a\right] = i/2$.

Prior to mixing to detect the two quadratures, it is crucial that the quantum complex amplitude $\hat{S}_a = \hat{a}$ is amplified by a phase-insensitive linear amplifier, treating both quadratures the same. The equal amplification of both quadratures necessarily adds amplified vacuum fluctuations that ensure the minimally possible Heisenberg uncertainty, however, additionally thermal noise is added. Thus, the linearly amplified field $\hat{a}_\mathrm{g}$ results in a linear combination of signal and noise:

$$\hat{a}_\mathrm{g} = \sqrt{g}\,\hat{a} + \sqrt{g-1}\,\hat{h}_\mathrm{g}^\dagger\,,$$

where $\hat{h}_\mathrm{g}^\dagger$ describes the vacuum fluctuations and the thermal noise added during amplification (Caves, 1982; da Silva *et al.*, 2010); compare Section 3.1.

The detection of both quadratures is performed by mixing. This process is described by, first, beam splitting, and then detecting the in-phase component in one output and the quadrature component in the other output of the beam splitter. Here, we consider the beam splitter operation (2.7) where $\hat{a}' = \hat{a}_\mathrm{g}$ is the input field of the mixer, $\hat{b}' = \hat{h}_m$ is in the vacuum or a weak thermal state, and $\hat{a}_m$ and $\hat{b}_m$ are the two outputs of the beam splitter:

$$\hat{a}_m = \tfrac{1}{\sqrt{2}}(\hat{a}' + \hat{h}_m) \qquad\qquad \hat{b}_m = \tfrac{1}{\sqrt{2}}(\hat{a}' - \hat{h}_m)\,.$$

In each of the two beam splitter outputs one of the two quadratures

$$\hat{I} = \tfrac{1}{2}(\hat{a}_m + \hat{a}_m^\dagger) \qquad\qquad \hat{Q} = \tfrac{-i}{2}(\hat{b}_m - \hat{b}_m^\dagger)$$

is measured (da Silva *et al.*, 2010). Since the two quadratures between the two beam splitter outputs commute, $\left[\hat{I}, \hat{Q}\right] = 0$, due to the added noise mode $\hat{h}_m$, both quadratures $\hat{I}$ and $\hat{Q}$ can be measured simultaneously and the complex amplitude can be defined as

$$\hat{S} \equiv \hat{I} + i\,\hat{Q} = \tfrac{1}{\sqrt{2}}(\hat{a}' + \hat{h}_m^\dagger)\,.$$

Thus, a beam splitter can be used to transform a quantum signal $\hat{a}'$ into a classical signal where both quadratures are simultaneously measurable and the necessary measurement uncertainty is given by the fluctuations added through the second beam splitter input $\hat{b}' = \hat{h}_m$. Note that the principle of detecting both quadratures is the same for the two-step detection in heterodyne detection schemes, however, with increased noise fluctuations due to the superposition of the signal with noise at its image as discussed in Sections 3.2 and 3.3.

Putting amplification and mixing together the complex amplitude is written as

$$\hat{S} = \sqrt{g}\,(\hat{a} + \hat{h}^\dagger)\,, \tag{3.2}$$

where $\hat{h}^\dagger$ composed of $\hat{h}_\mathrm{g}^\dagger$ and $\hat{h}_\mathrm{m}^\dagger$ is the total effective noise added by the linear detection chain[1]. Since the commutator $\left[\hat{S}, \hat{S}^\dagger\right] = 0$, both quadratures of $\hat{S}$ can be measured simultaneously. The vanishing commutator shows also that the order of $\hat{S}$ and $\hat{S}^\dagger$ can be commuted as long as no other operators with non-vanishing commutators are involved. Thus, standard mathematical quantities of these operators can be computed as if they are complex numbers S and S^*, which is the reason to omit a hat on S. Note that due to Heisenberg's uncertainty principle the exact and simultaneous measurement of both quadratures of $\hat{a}$ is not possible. However, S provides a measurement of both quadratures, where uncertainty is given by the noise $\hat{h}^\dagger$.

Equation (3.2) allows to calculate quantum-mechanically the expected measurement outcomes. For example, the expectation value of the complex amplitude

$$\langle \hat{S} \rangle \propto \langle \hat{a} + \hat{h}^\dagger \rangle = \langle \hat{a} \rangle + \langle \hat{h}^\dagger \rangle = \langle \hat{a} \rangle$$

---

[1] For simplicity the missing factor 1/2 is absorbed in the gain factor g.

is proportional to the field $\hat{a}$ of interest. Note that the noise is assumed to be uncorrelated and symmetrically distributed around zero, therefore its expectation value is equal to zero (Agarwal and Chaturvedi, 1994; da Silva *et al.*, 2010).

Similar expressions can be evaluated for correlations of the complex amplitude, for example

$$\langle \hat{S}^\dagger \hat{S} \rangle \propto \langle (\hat{a}^\dagger + \hat{h})(\hat{a} + \hat{h}^\dagger) \rangle = \langle \hat{a}^\dagger \hat{a} \rangle + \langle \hat{h}\hat{h}^\dagger \rangle$$

that contains the expectation value of the photon number operator $\hat{a}^\dagger \hat{a}$ and the noise power $\langle \hat{h}\hat{h}^\dagger \rangle$ added by the linear detection chain. Further correlators and correlation functions are evaluated in Appendix B.

3.5 Measurement of Power

So far, we have described the measurement of the complex amplitude $S[t]$ of itinerant microwave radiation at cryogenic temperatures using a heterodyne detection chain. Frequently an average of $S[t] = M[t]\, e^{i\varphi[t]}$ is measured to evaluate the expectation value of magnitude $M[t]$ and phase $\varphi[t]$ of the complex amplitude. A further common quantity of interest is the power $M^2[t]$ that is, on average, carried in the microwave signal, as measured integrated over time by Houck *et al.* (2007) using a diode as power-law detector.

We distinguish two special cases, coherent and incoherent radiation. For coherent radiation, the microwave has a well defined phase for all times. Hence, the radiation can be repeatedly prepared and then measured to extract the expectation value of $S[t]$, where the noise is canceled. Thus, $M[t]$ is uniquely determined by the expectation value, so that the power $M^2[t]$ follows from a nonlinear operation, however, based an expectation value. This is in contrast to usual incoherent radiation, where the microwave has random phases $\varphi[t]$ and consequently the expectation value of $S[t]$ calculated from repeated preparations is equal to zero. It is therefore not possible to determine the power based on the average of $S[t]$. Instead, we calculate the *power* of $S[t]$, i.e. the square of the absolute $|S[t]|^2 = S^*[t]\, S[t] = M^2[t] \in \mathbb{R}$, before averaging. The random phase factor is dropped in this operation, so that the average of the obtained power is proportional to the power of the itinerant microwave radiation superimposed with the power of the noise added during linear detection.

The measurement of two complex amplitudes $S_a[t]$ and $S_b[t]$ that are at every instance in time extracted in two separate detection chains allows us to calculate the so called *cross-power* $S_a^*[t]\, S_b[t]$. When a microwave field is measured by two detection chains, for example using a microwave beam splitter, the average of the cross-power is proportional to the microwave field power (da Silva *et al.*, 2010; Bozyigit *et al.*, 2011a; Menzel *et al.*, 2010). In contrast to the power calculation where the noise power was still included, here the noise in $S_a[t]$ and $S_b[t]$ have uncorrelated random phases and amplitudes, and hence average out to zero.

Here, we emphasize that in addition to power many other quantities may be calculated within this approach. Let $w[t] : \mathbb{C}^2 \rightarrow \mathbb{C}$ denote a waveform which is continuously calculated for each point in time t based on up to two measured complex amplitudes $S_a[t]$ and $S_b[t]$. A waveform can represent any of the two complex amplitudes, single quadratures thereof, or powers calculated as discussed above. Note that other mathematical operations are feasible and, with that, the measurement of other physical quantities than discussed here.

3.6 Data Reduction

Typically we filter the measured complex amplitudes such that their bandwidth is not much larger than the bandwidth of the physical signal. However, generally the bandwidth of a resulting waveform is not equal to the ADC sampling rate f_s. Hence, the waveform contains redundant sample points that can be removed without loss of information. Thus, for example, disk space on the host computer is reduced, data can be transfered faster, and it is possible to adapt to speed limitations and hardware resources on the FPGA board if required.

If the spectral density of a waveform $w[t]$ is bandwidth limited within $\pm f_\mathrm{s}/d$ with integer *decimation* factor $d \geq 2$, a time resolution faster than $d/f_\mathrm{s} = d\,t_\mathrm{s}$ will not increase information contained in the signal. For example, the power spectral density in Figure 3.2(e) is essentially zero outside the limited bandwidth for $d = 3$ indicated by the dashed lines and thus it is sufficient to restrict the signal to that bandwidth. This is realized by keeping only one out of d sample points for further analysis, which reduces the total maximum bandwidth to f_s/d. Remaining frequency components outside of the introduced folding frequency $\pm(f_\mathrm{s}/2)/d$ are shifted to their alias frequencies within the reduced bandwidth, as discussed in Section 3.1 but using the introduced folding frequency. Thus, the decimation of Figure 3.2(e) results in a superposition of the three regions separated by the dashed lines. After this decimation operation, sampling frequency and period go to $f_\mathrm{s} \to f_\mathrm{s}/d$ and $t_\mathrm{s} \to d\,t_\mathrm{s}$ respectively.

3.7 Scattering Parameter Measurement

In Sections 3.1 to 3.6, we have discussed signal processing that is performed continuously and on every sample point of the discrete-time signal. To access characteristic quantities of the microwave radiation, such as phase, power, or correlations, where the experimental noise in $S[t]$ is averaged out or subtractable, further signal analysis is necessary. We therefore have implemented a variety of *measurement applications* that perform the desired analysis. Unlike the continuous signal processing discussed until now whereas each sample point is processed by the same set of operations, a measurement application analyzes finite intervals of the waveforms $w[t]$ whereas the processing may differ between samples within the interval.

Consider the measurement of scattering parameters, which allows one to investigate the steady state microwave properties of a device under test. A scattering parameter gives information about the magnitude and phase change of a continuous wave, that is elastically scattered by that device in forward or backward direction (Pozar, 2011). Scattering parameters are typically measured with a commercial vector network analyzer in dependence on the frequency of the continuous wave to perform spectroscopy. For measuring a scattering parameter $\langle S\rangle_T$, the complex amplitude $S[t]$ of a continuous wave is detected within a very narrow bandwidth. This guarantees to average out the noise in $S[t]$. Here, narrow bandwidth detection is achieved by averaging a waveform

$$\langle w\rangle_T \equiv \frac{1}{N}\sum_{t=0}^{T-t_\mathrm{s}} w[t]$$

over $N \in \mathbb{N}$ samples in $w[t]$ for a total time $T = Nt_\mathrm{s}$. The integration time T sets the detection bandwidth to f_s/N, as discussed for the square window FIR filter in Section 3.3. No part of the signal is filtered out for any chosen T, since the signal is a continuous wave, i.e. a Dirac delta function in the frequency domain. However, typical noise is not a delta function at d.c. but distributed in frequency (such as the white noise that is added to the signal during amplification) and hence effectively filtered out for small detection bandwidths, i.e. large T.

3.8 Time-Dependent Ensemble Average

A single realization of a pulsed experiment, referred to as a *shot*, is often repeated several times. A prominent application in circuit QED is the ensemble average of the resonator transmission that depends on the qubit state used as dispersive qubit state read-out; compare Section 2.4.1. The measurement traces in Figure 2.6(c,d) show a measured time-dependent ensemble average of repeated read-out pulses (Wallraff *et al.*, 2005; Bianchetti *et al.*, 2009).

To average a time-dependent quantity over R repetitions, we evaluate the ensemble average

$$\langle w\rangle[t] \equiv \langle w\rangle_R[t] \equiv \frac{1}{R}\sum_{r=0}^{R-1} w[t + r\,T_\mathrm{p}]\,,$$

where T_p is the repetition period and $\langle w\rangle[t]$ consists of l sample points at times $t = t_0, \ldots, t_{l-1}$.

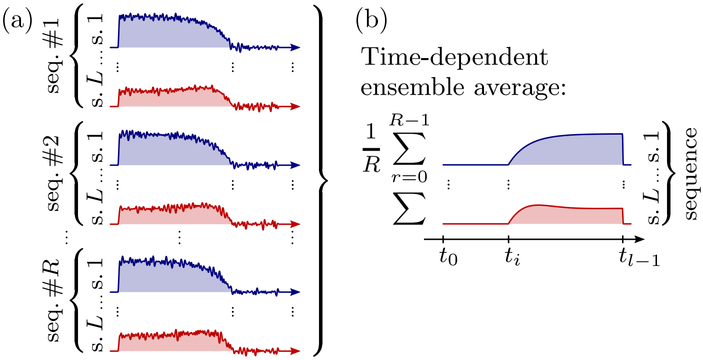

Figure 3.4: Time-dependent ensemble averaging. (a) Repeated measurement *sequence* (seq.) consisting of L settings 's. 1' to 's. L' executed from top to bottom. (b) Time-dependent averaging into L *segments* each corresponding to one setting.

Consider an experimental situation, where the ensemble average is investigated dependent on $L \in \mathbb{N}$ different settings 's. 1' to 's. L', in which, e.g., an experimental parameter is swept. Performing the ensemble average separately for each of the L settings, long term drifts such as amplifier gain may have different influence on the L measurements. To diminish this heterogeneous impact, we set-up a *sequence* that switches from 's. 1' to 's. L' shot by shot and average that *sequence* for the desired R repetitions, as sketched in Figure 3.4(a). Each measured shot is in this way averaged into one of L *segments* that correspond to the settings 's. 1' to 's. L'; compare Figure 3.4(b). Comparable averaging functionalities are also available in commercial digitizer boards, but extended here: in contrast to averaging the bare digitized signal $\langle V\rangle[t]$, we directly average the complex amplitude $\langle S\rangle[t]$ such that no post signal processing and decimation has to be performed on the host computer. Similarly (compare Section 3.5) the ensemble average of the time-dependent power $\langle|S|^2\rangle[t]$ and cross-power $\langle S_a^* S_b\rangle[t]$ can be measured.

Recall that $\langle|S|^2\rangle[t]$ measures the power of the microwave signal superimposed with the mean of the noise power contained in $w[t] = |S[t]|^2$. The noise power can be subtracted from the ensemble average $\langle |S|^2 \rangle [t]$, when an additional setting 's. *off*' is included into the measurement *sequence*, in which the detection chain input is left idle. For 's. *off*', the ensemble average serves as a reference measurement for the noise power. Similarly, residual correlated noise power can be subtracted from the ensemble average of the cross-power $\langle S_a^* S_b \rangle [t]$ using a reference measurement.

3.9 Two-Time Correlations

The characterization of electromagnetic radiation using correlation function measurements is one of the most important tools in the field of quantum optics. The power spectral density, for example, is the Fourier transform of the first-order correlation function, and measures the frequency-dependent power density in an electromagnetic field. However, sources of radiation differ not only by their frequency but also by the statistical properties of the emitted photons (Walls and Milburn, 2008; Lang *et al.*, 2011). Antibunching and sub-Poissonian photon number distribution can be demonstrated by measureing second-order correlation functions (Zou and Mandel, 1990). The measurement of these correlation properties allows one to distinguish quantum from classical radiation, such as coherent or thermal fields, which can be described by Maxwell's equations ignoring field quantization.

The correlation function of two waveforms $w_1[t]$ and $w_2[t]$ is defined as

$$(w_1 \star w_2)[\tau] \equiv \sum_{t=0}^{T-t_\mathrm{s}} w_1^*[t]\, w_2[t+\tau \mod T]\,, \tag{3.3}$$

where $\star$ denotes correlation and T is the total integration time. The time delay τ takes the values $\tau = -\frac{T}{2}, \ldots, -t_\mathrm{s}, 0, t_\mathrm{s}, \ldots, \frac{T}{2} - t_\mathrm{s}$. The time index is cyclically wrapped around the finite interval of the waveform $w_2[t]$ by the modulo operation and hence ensures that the

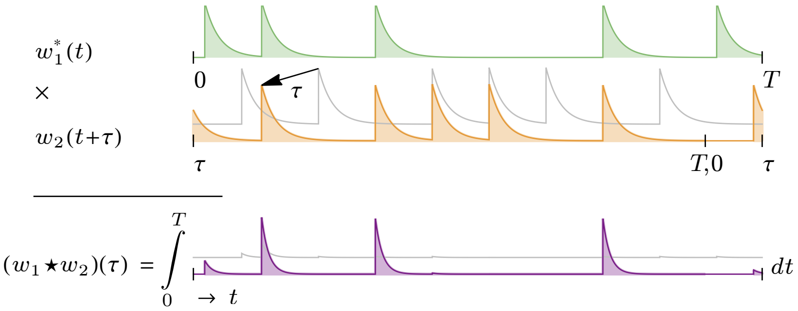

Figure 3.5: Illustration of a continuous-time circular correlation function $(w_1 \star w_2)(\tau)$. Here, $w_2(t)$ (gray waveform) is shifted by τ (orange waveform) and multiplied (×) with $w_1^*(t)$ (green). Then, the result thereof (purple) is integrated. The first pulse in $w_2(t)$ around τ illustrates the circular wrapping of the time by $t+\tau \mod T$. The gray line displays the situation for $\tau = 0$, where no pulse is present in both waveforms. Hence $(w_1 \star w_2)(\tau)$ is approximately equal to 0.

time index is within 0 and $T - t_\mathrm{s}$. In Figure 3.5 correlations for continuous time are illustrated. As the integral increases for pulses present in both waveforms, the correlation function is a measure for the similarity of the two waveforms $w_1[t]$ and $w_2[t+\tau]$ in dependence of the time delay τ.

Equation (3.3) can be written as

$$(w_1 \star w_2)[\tau] = \mathcal{F}^{-1}\big(\mathcal{F}^*(w_1) \cdot \mathcal{F}(w_2)\big)[\tau] \tag{3.4}$$

where the discrete-time Fourier transform is

$$\mathcal{F}(w)[\nu] = \sum_{t=0}^{T-t_\mathrm{s}} w[t]\, e^{-i2\pi t\nu/N} \,,$$

with $N = T/f_\mathrm{s}$, and its inverse: $\mathcal{F}^{-1}(w)[\tau] = \frac{1}{N}\sum_{\nu=0}^{f_\mathrm{s}-\varDelta\nu} w[\nu]\, e^{i2\pi\tau\nu/N}$. Here, the discrete frequencies ν take the values $\nu = -\frac{f_\mathrm{s}}{2}, \ldots, -\varDelta\nu$, $0, \varDelta\nu, \ldots, \frac{f_\mathrm{s}}{2} - \varDelta\nu$ with the frequency bin width $\varDelta\nu = 1/T$. The correlation function measurement is usually averaged over R repetitions, which we denote as $\Gamma[\tau] = \langle w_1 \star w_2 \rangle[\tau]$. If $w_1[t] = w_2[t] = w[t]$ we use the term *auto*-correlation, while if $w_1[t] \neq w_2[t]$ we denote it as *cross*-correlation. When each waveform is a complex amplitude it is called a *first-order* correlation $\Gamma^{(1)}[\tau]$, and *second-order* correlation $\Gamma^{(2)}[\tau]$ when two powers (each power is the product of two complex amplitudes) are correlated; compare Section 3.5. Notably, also other correlations are feasible, such as the correlation of a power with a complex amplitude.

Technically, the direct computation of $(w_1 \star w_2)[\tau]$ as in Equation (3.3) is highly demanding in terms of arithmetic operations, more precisely $O(N^2)$ operations. Computational efficiency improves significantly using Equation (3.4) by taking advantage of fast Fourier transform algorithms and setting N to a power of 2, which reduces the correlation to $O(N \log N)$ complexity. Since the inverse Fourier transform and ensemble average are both linear operations, their order of operation can be interchanged. This simplifies the measurement of $\Gamma[\tau]$ to

$$\Gamma[\tau] = \mathcal{F}^{-1}\big(\langle \mathcal{F}^*(w_1) \cdot \mathcal{F}(w_2) \rangle\big)[\tau]\,, \tag{3.5}$$

where $\mathcal{F}^{-1}$ is performed only once on the ensemble average. In our case, the two Fourier transforms $\mathcal{F}$, the complex multiplication, and the ensemble average are performed on the FPGA. The inverse Fourier transform can be done afterwards by software on the host computer.

A prominent application of correlation function measurements is the determination of the power spectral density $\mathrm{PSD}\,[\nu] = \langle |\mathcal{F}(S)|^2 \rangle[\nu]$ of the complex amplitude $S[t]$. Here, the PSD is evaluated using the ensemble average in Equation (3.5) for a first-order auto-correlation function measurement with $w_1[t] = w_2[t] = S[t]$. The measurement $\mathrm{PSD}\,[\nu]$ returns the total radiation power for each frequency bin ν of width[2] $\Delta\nu$. Notably, the power spectral density of the itinerant microwave signal without noise [Figure 3.2(a)] is restored by the subtraction of a reference PSD measurement, where the detection chain input is left idle, shown by Figure 3.2(d-f) without the purple signal. Idle means that the microwave source of interest is switched *off*, and therefore corresponds to the input of the detection chain being in the vacuum state. We use the suffixes *off* and *on* to distinguish between two types of measurements. The suffix *off* denotes the reference measurement of noise, and the suffix *on* denotes measurements with the microwave signal of interest. Higher-order correlations require a series of measurements to measure several correlation terms. For each term a measurement in *on* and *off* mode is needed to realize noise subtraction. We refer to Appendix B and da Silva *et al.* (2010) for a detailed description and derivation of these terms. In Appendix B we use the operator formulation of the complex amplitude, introduced in Section 3.4, to link the measured correlation functions $\Gamma[\tau]$ with the quantum-mechanical definition of the correlation function $G[\tau]$.

---

[2] Leakage present in discrete-time Fourier transforms is not taken into account here. The phenomenon of leakage describes the fact that radiation power at frequencies not exactly equal to the frequency bin center ν is partially displayed in the nearby bins (Lyons, 2004).

As for the time-dependent ensemble averages, discussed in Section 3.8, we suppress the influence of long term drifts by setting up a differential *sequence* with two experimental settings: 's. *on*' that generates the radiation field of interest and 's. *off*' which leaves the detection chain input idle. Additionally, for noise subtraction in second-order correlation function measurements, we need to evaluate both second- and first-order correlation terms. We therefore alternate not only between 's. *on*' and 's. *off*' but also between the evaluation of all necessary second- and first-order correlation terms[3]. In that manner we get one averaged measurement record for each of the different correlation terms both for *on* and *off* measurements. As shown in Appendix B the noise subtraction can then be performed using these averaged measurement records.

3.10 Measurements of Moments

A further powerful application of our signal analyzer for microwave field correlation analysis is the measurement of complex amplitude moments. For one and two microwave field modes these moments are expectation values of the form

---

[3] In principle all necessary correlation terms could be evaluated in parallel, however, to save resources on the FPGA we alternate between them.

$$\langle (S^*)^n (S)^m \rangle \quad \text{and} \quad \langle (S_a^*)^n (S_a)^m (S_b^*)^k (S_b)^l \rangle \ , \tag{3.6}$$

respectively, for all $n, m, k, l \in \mathbb{N}^0$. Instead of the time-resolution in correlation function measurements, discussed in Section 3.9, arbitrary-order correlations can be investigated. We typically transform $S(t)$ into S by temporal mode matching for the complex amplitude of interest using an appropriate FIR filter, which optimizes the detection efficiency (Eichler, Bozyigit, and Wallraff, 2012). The measured set of all moments gives the full state tomography of itinerant microwaves, which includes joint tomography of field modes separated in space or time.

For the purpose of calculating the moments over $R \in \mathbb{N}$ repetitions, we populate 2D-, 3D- or 4D-histograms with R tuples of the form $\{\Re(S_a), \Im(S_a), \Re(S_b), \ldots\}[t_1 + r\,T_\mathrm{p}]$ of the measured quadratures evaluated at fixed times $t_1 + r\,T_\mathrm{p}$, where r is the shot number and T_p the repetition period. For field modes separated in time the quadratures in the tuple can be evaluated at different times; see Eichler *et al.* (2012). From the populated histograms all moments with $n, m, k, l \in \mathbb{N}^0$ can be extracted. The noise added during detection, that is included in the measured moments, can be canceled when an additional *off*-histogram serving as noise reference is taken into account. Similarly as in Section 3.9, we populate *off*- and *on*-histograms by setting up a differential *sequence*, where the first setting 's. *off*' leaves the detection chain input idle and the second setting 's. *on*' prepares the radiation field of interest. We refer to Eichler, Bozyigit, and Wallraff (2012) for a detailed description of the method to extract the moments from the histograms.

From a technical point of view, we set-up an array of memory cells and initialize all to zero. Each cell is assigned to hold the number of counts in its corresponding histogram bin. A small 2D-example is shown in Figure 3.6. Here the red framed bin holds the counts with $\Re(S) \in \left[0, \frac{1}{4}\right) \vee \Im(S) \in \left[-\frac{3}{4}, -\frac{2}{4}\right)$. For each shot we get one tuple, and consequently the count of the corresponding histogram bin is increased by 1.

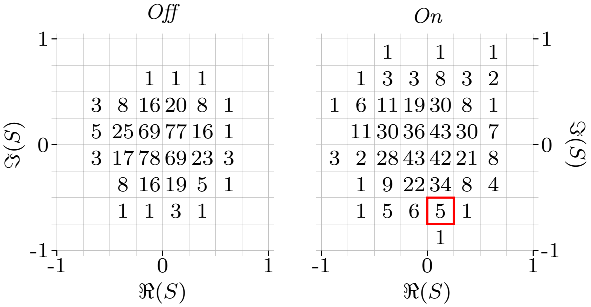

Figure 3.6: Sketch of histogram bins displaying the counts of an *off*- and *on*-histogram. Each measured tuple $\{\Re(S), \Im(S)\}$ falls into the range of a histogram bin (e.g. the bin framed red), whose count is consequently increased by 1.

We run the measurement of the histograms multiple times and extract the moments for each run. Statistical analysis gives the averaged moments and their standard deviations as statistical error estimates (Eichler, Bozyigit, and Wallraff, 2012). Measurements using the histogram method demonstrated anti-bunching and squeezing in quantum microwave radiation (Eichler *et al.*, 2011b,a), entanglement of an itinerant microwave field with a qubit read-out field quadrature (Eichler *et al.*, 2012), and the entanglement of two itinerant microwave fields (Lang *et al.*, 2013b), presented in Section 6.3. Similar analyses measuring the moments of microwave radiation are performed in Menzel *et al.* (2012). There the moments are not evaluated through histograms but are calculated directly as formulated in Equation (3.6).

4

Photon Blockade

Creating a train of single photons, and monitoring the propagation of photons and in particular their interaction with other photons or matter is challenging in most physical systems, because photons generally interact very weakly. For microwave frequency photons confined in a transmission line resonator, qubits embedded in the resonator can be used to mediate effective photon-photon interactions. In this chapter, we discuss the observation of the phenomenon of photon blockade, where radiation with a power corresponding to more than one photon per characteristic time interval is blocked due to strong effective photon-photon repulsion. In particular, resonance fluorescence and Rayleigh scattering in Mollow-triplet-like spectra are investigated (Section 4.2) to confirm the realization of a driven effective two-level system (Mollow, 1969). Also second-order correlation functions are measured (Section 4.3), which clearly demonstrate antibunching in a continuously pumped source of single microwave photons. Antibunching refers to the tendency of photons being preferentially distributed separated in time rather than at random or in bunches (Zou and Mandel, 1990). To show photon statistics other than antibunching, second-order correlation functions are demonstrated for continuous sources of coherent and thermal microwave radiation, which display a random and a bunched photon distribution, respectively (Lang *et al.*, 2011).

4.1 Effective Photon-Photon Interactions

Sources of radiation differ not only by their frequency but also by the statistical properties of the emitted photons (Walls and Milburn, 2008). Thermal sources emit radiation that is characterized by an enhanced probability of emitting photons in bunches. Coherent sources, such as a laser, emit radiation with a Poisson-distributed photon number. The photon-counting statistics of these two sources can be explained classically. In contrast, individual atoms emit photons one by one well separated in time from each other, a phenomenon for which antibunching—a unique quantum characteristic of the field—can be observed.

In strongly nonlinear systems, a phenomenon known as photon blockade (Tian and Carmichael, 1992; İmamoğlu *et al.*, 1997) can be used to generate a train of single photons that displays antibunching. Photon blockade is typically realized in cavity QED setups. Here, coherent radiation at the input of a cavity coupled to an anharmonic system, such as a single atom, is converted into a train of single photons in the transmitted light. The transmitted radiation has two important characteristics: sub-Poissonian photon statistics and photon antibunching. Sub-Poissonian statistics are experimentally demonstrated by showing that the second-order correlation function fulfills the inequality $g^{(2)}(\tau) \leq 1$ for all times τ. Photon antibunching is demonstrated by a rise of $g^{(2)}(\tau)$ with τ increasing from 0 to larger values while $g^{(2)}(0) < g^{(2)}(\tau)$, as discussed in detail by Zou and Mandel (1990).

So far photon blockade has been realized in different setups, however, all suffer from different drawbacks. At optical frequencies, resonant photon blockade—the cavity and atom share the same resonance frequency—was demonstrated with a single trapped atom in an optical cavity (Birnbaum *et al.*, 2005). These measurements suffer from adverse effects of trapping laser beams, micro motion of the atom in its trap, and the necessity of post selecting data for instances of single-atom measurements. In the solid state, resonant photon blockade was demonstrated with a quantum dot in a photonic crystal cavity (Faraon *et al.*, 2008). Those experiments suffer from quantum dot blinking and limited detector time resolution.

Our experiments are realized in the microwave regime with a single superconducting artificial atom resonantly coupled to a transmission line resonator, representing a cavity QED setup (Haroche, 1992) in a circuit reaching the strong coupling limit (Wallraff *et al.*, 2004; Schoelkopf and Girvin, 2008). The artificial atom at rest, which is here well approximated by a two-level system, has a strong, fixed coupling to the resonator. In addition, our setup benefits from high-efficiency emission of photons in the forward direction by employing an asymmetric quasi-one-dimensional resonator dominated by a single mode resonant with the artificial atom. This is in contrast to the atomic case for which the multi-mode structure of the cavity is important (Birnbaum *et al.*, 2005). Also, the effective polarization of the radiation is fixed by the boundary conditions enforced by the superconducting metal forming the resonator and thus does not play a role in our experiments. Photon blockade in superconducting circuits has been independently studied in the dispersive regime by Hoffman *et al.* (2011).

Our experimental setup is composed of a photon source and a complex amplitude detection system from which we extract the photon statistics introduced in Chapter 3. The sample used for the experiments presented here is shown in Figure 2.3. The continuous single-photon source consists of a single transmon with transition frequency ν_a resonantly coupled to a resonator with resonance frequency $\nu_\mathrm{r} = \nu_\mathrm{a} = 6.769\,\mathrm{GHz}$. Thus, transmon and resonator energy levels are hybridized into the Jaynes-Cummings ladder marked by the red shade in Figure 2.4 and schematically shown in Figure 4.1; compare Section 2.3. The coherent dipole coupling strength $g/2\pi = 73\,\mathrm{MHz}$ dominates over the dissipation due to photon loss from the cavity at rate $\kappa/2\pi \approx 4\,\mathrm{MHz}$ and the qubit decay at rate $\gamma/2\pi \approx 0.4\,\mathrm{MHz}$. When radiation impinges on the resonator input at frequency $\omega_\mathrm{d}/2\pi = (\omega_\mathrm{r} - g)/2\pi$, which is the transition frequency from the ground state $|g0\rangle$ to the lower state $|1-\rangle$ of the first Jaynes-Cummings doublet $|1\pm\rangle$, only a single photon can enter at a time; see Figure 4.1. Additional photons are prevented from entering the resonator, as transitions into higher excited states are blocked due

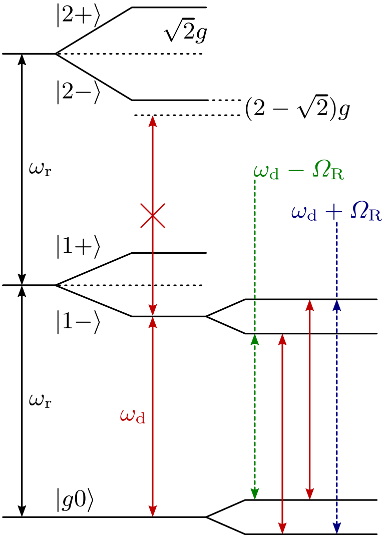
$|2+\rangle$
$\sqrt{2}g$
$|2-\rangle$
$(2-\sqrt{2})g$
ω_r
$\omega_\mathrm{d}-\Omega_\mathrm{R}$
$\omega_\mathrm{d}+\Omega_\mathrm{R}$
$|1+\rangle$
$|1-\rangle$
ω_r
ω_d
$|g0\rangle$

Figure 4.1: Energy level diagram of a resonantly coupled cavity QED system driven with amplitude Ω_R on the lower Jaynes-Cummings doublet. The Mollow-type transitions arising from the dressing of the $|g0\rangle$ and $|1-\rangle$ states by the drive are also indicated on the right hand side.

to the strong nonlinearity of the resonantly coupled qubit-resonator system (Schuster *et al.*, 2008; Hofheinz *et al.*, 2008; Fink *et al.*, 2008). In analogy with measurements in mesoscopic systems, where electron transport is blocked by the strong Coulomb interaction in a confined structure, this process is called *photon blockade* (İmamoğlu *et al.*, 1997). Only once the photon has left the cavity can the next photon enter into the resonator, realizing a single photon turnstile device.

To investigate the statistical properties of our microwave frequency radiation source, we use the scheme for measuring correlation functions presented in Section 3.9. Here, the radiation of the source is passed through the on-chip 50/50 beam splitter; see micrograph of the sample in Figure 2.3. Then the complex amplitude at each output of the beam splitter is extracted using independent heterodyne detection chains, as discussed in Sections 3.1 to 3.4. Expectation values of field amplitude, power, and first- and second-order correlation functions are extracted from the instantaneous values of the measured complex amplitudes; compare Sections 3.5, 3.8 and 3.9.

4.2 Observation of Mollow Triplets

We set-up our continuous single-photon source by tuning the transmon qubit transition frequency ω_{a} into resonance with the resonator using d.c. magnetic flux; compare Sections 2.2.2, 2.3 and 2.6. When probing the resonator transmission (Figure 2.5 at $\Phi \approx -0.11\,\Phi_0$) with a weak coherent tone resulting in an average resonator photon number $\langle n \rangle \ll 1$, we observe the characteristic vacuum Rabi mode splitting (Wallraff *et al.*, 2004; Fink *et al.*, 2008) resulting from the anharmonic level structure shown in Figure 4.1. In many experiments of this type, only the Rayleigh-scattered (elastic and coherent) part of the transmitted amplitude is detected in a heterodyne measurement with a small effective bandwidth of $\sim 50\,\mathrm{kHz}$; compare Section 3.7. Here, however, we have digitally recorded the resulting fields *vs.* time in both arms of the beam splitter with a bandwidth of $\sim 50\,\mathrm{MHz}$. Instantaneous power spectra of the source are then calculated as the product of the Fourier transform of the time-dependent signals in each arm, which are subsequently averaged; compare Section 3.9. Thus, we observe not only the Rayleigh-scattered radiation [narrow high-amplitude peak in Figure 4.2(a)] but also the incoherently scattered resonance fluorescence part of the spectrum [broad low-amplitude triplet in Figure 4.2(a)]. The resonance fluorescence spectrum is characterized by three spectral lines [four transitions (Figure 4.1), two of which are degenerate] forming a Mollow triplet of a resonantly driven effective two-level system (Mollow, 1969); compare Appendix C.1. The two levels are realized by the joint ground state $|g0\rangle$ and the lower energy state of the first doublet $|1-\rangle = (|g1\rangle - |e0\rangle)/\sqrt{2}$ of the Jaynes-Cummings ladder. The dressing of the $|g0\rangle$ and $|1-\rangle$

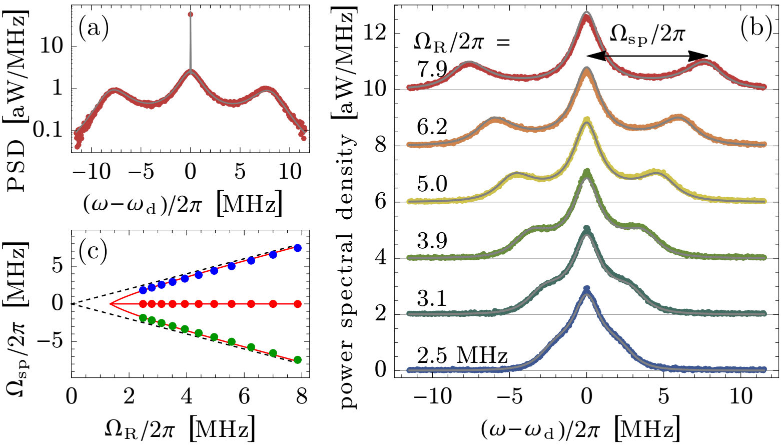

Figure 4.2: Rayleigh-scattering and resonance fluorescence of lower Jaynes-Cummings doublet. (a) Measured resonance fluorescence spectrum including Rayleigh-scattering peak (dots) at fixed drive amplitude of $\Omega_{\mathrm{R}}/2\pi = 7.9\,\mathrm{MHz}$ and the simulated spectrum (solid line). (b) Measured resonance fluorescence spectrum (dots) *vs.* drive amplitude $\Omega_{\mathrm{R}}/2\pi$ (indicated) and analytical spectrum (solid lines). The Rayleigh peak has been omitted in these plots. (c) Measured Mollow side peak frequencies Ω_{sp} *vs.* drive amplitude Ω_{R} (dots), linear dependence $\Omega_{\mathrm{sp}} = \Omega_{\mathrm{R}}$ (dashed black lines) and calculated frequencies Ω_{sp} (solid red lines) are shown.

states by the drive field has been discussed theoretically in Tian and Carmichael (1992) and was experimentally investigated with superconducting circuits considering only the Rayleigh-scattered part of the radiation (Bishop *et al.*, 2009).

All measured spectra are in excellent agreement with the numerically calculated steady-state solution of the master equation taking into account two qubit levels and five resonator levels [solid line in Figure 4.2(a)]. For this calculation, introduced in Appendix C.1.2, we use the device parameters quoted in Section 4.1. The solid lines in

Figure 4.2(b) show the analytically calculated fluorescence spectrum of the coherently driven effective two-level system which is virtually indistinguishable from the master equation calculation and the data. In this calculation, sketched in Appendix C.1.1, we only include four parameters (the decay rate $\tilde{\gamma}$ and dephasing rate $\tilde{\gamma}_\varphi$ of the effective two-level system, the drive strength, and the gain factor of the heterodyne detection) and do not make approximations for the strength of the drive as done for the typically quoted result (Carmichael, 2002; Mollow, 1969). To correctly capture the amplitude of the coherently scattered radiation, the state $|2-\rangle$ is included in the calculation.

We observe that the frequency Ω_{sp} by which the Mollow side peaks are offset from the central peak depends on the drive amplitude Ω_{R} [Figure 4.2(b)]. For large Ω_{R}, Ω_{sp} scales linearly with Ω_{R}, i.e. $\Omega_{\mathrm{sp}} \approx \Omega_{\mathrm{R}}$. For drive amplitudes approaching the characteristic rate of dissipation the deviation of Ω_{sp} from Ω_{R} becomes larger [Figure 4.2(c)]. In addition, the height of the side peaks decreases compared to the central Lorentzian peak such that for small drive amplitudes the side peaks vanish. All these effects are accurately explained by the analytical two-level model [see red solid lines in Figure 4.2(c) and Appendix C.1.1] (Carmichael, 2002). Similar Mollow triplet-like structures were also observed in strongly driven superconducting flux and charge qubits using various detection techniques (Baur *et al.*, 2009; Sillanpää *et al.*, 2009; Astafiev *et al.*, 2010).

We note that, for the measurements of power spectra, the uncorrelated noise added by the two independent detection chains is efficiently averaged out (Agarwal and Chaturvedi, 1994), and the residual noise offset, which is a factor of 10^3 smaller than the noise introduced by a single amplifier and is determined by performing a reference measurement where the system is left in the ground state, is subtracted from the data (da Silva *et al.*, 2010); compare Section 3.9.

4.3 Measurement of Photon Statistics

The experiments discussed above demonstrate the resonance fluorescence emitted from the cavity when it is weakly driven on the lower

Rabi resonance ($\omega_{\mathrm{r}} - g$). In this limit, photon blockade is expected to be observable in measurements of the normalized second-order correlation function $g^{(2)}[\tau]$. We extract $g^{(2)}[\tau]$ from a measurement of the cross-correlation of the power detected between the two outputs of the 50/50 beam splitter (da Silva *et al.*, 2010); compare Section 3.9 and Appendix B.4. The constant offset caused by the noise added by the amplifiers is subtracted and the correlation function is normalized to unity for times $\tau \to \infty$. For all drive amplitudes, photon antibunching is observed since $g^{(2)}[0]$ is at a minimum and $g^{(2)}[\tau]$ rises for increasing τ [Figure 4.3(a)]. For $\tau \to \infty$ we note that $g^{(2)}$ approaches a constant value, as expected. At the two largest drive amplitudes, we find characteristic oscillations in the measured $g^{(2)}[\tau]$ exactly at the frequency $\mathit{\Omega}_{\mathrm{R}}$ and a clear overshoot of $g^{(2)}[\tau]$ at around $\tau = \pi/\mathit{\Omega}_{\mathrm{R}}$. This indicates a correlation between a photon emitted at time t and a second photon emitted with high probability at the later time $(t+\tau)/\mathit{\Omega}_{\mathrm{R}} = \pi$ at which the drive has coherently re-excited the coupled system. At low drive amplitudes ($\mathit{\Omega}_{\mathrm{R}}/2\pi = 2.5\,\mathrm{MHz}$), we observe the transition towards sub-Poissonian photon statistics characterized by $g^{(2)}[\tau] \leq 1$ for all τ as the overshoot approximately vanishes.

We quantitatively compare the measured data to numerical calculations of $g^{(2)}[\tau]$ [see black lines in Figure 4.3(a)] based on a master equation calculation using the known system parameters. Considering the finite bandwidth $\sim 20\,\mathrm{MHz}$ of the digital filter used in the acquisition of the complex amplitude, we find excellent agreement between the measured data and the calculations; see gray lines in Figure 4.3(a) calculated as sketched in Appendix C.1.2. The small residual deviations of the measured $g^{(2)}[\tau]$ from the simulations are due to the noise added by the amplifiers. Note that each data trace was collected over 17 h corresponding to approximately 5.5×10^{10} measured photons and 15.75 Tbyte of analyzed complex amplitude data using the FPGA based electronics introduced in Chapter 3. The presented data clearly demonstrate the phenomenon of photon blockade in the microwave domain detected using second-order correlation function measurements.

For reference we have also measured $g^{(2)}[\tau]$ when populating the resonator with a mean thermal photon number $\langle n_{\mathrm{th}} \rangle \approx 1.4$ [Fig-

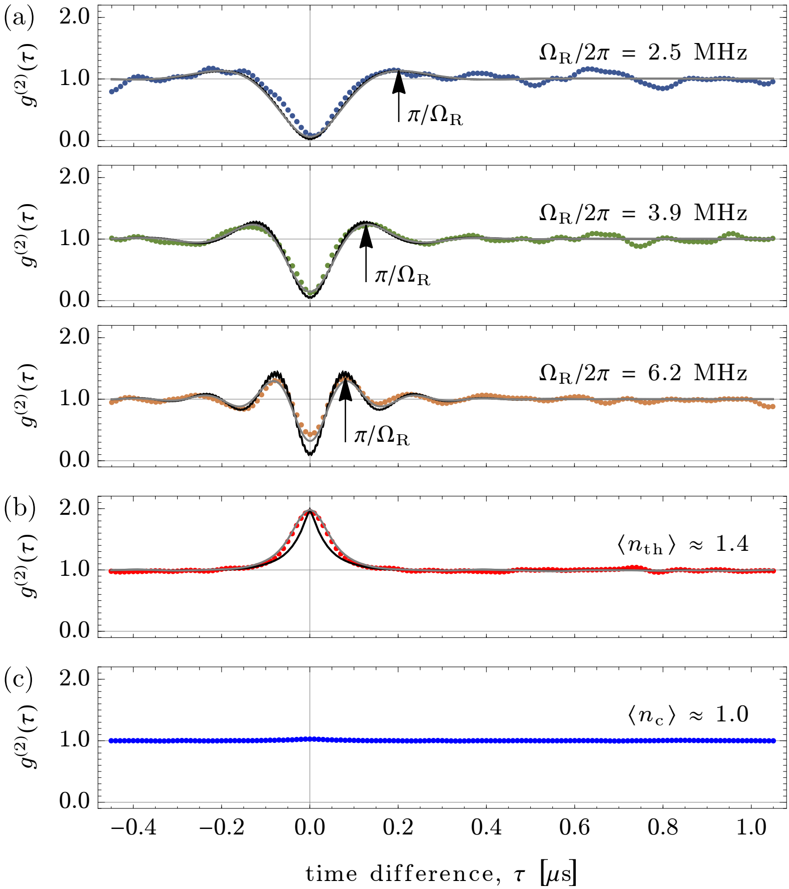

Figure 4.3: Correlation function measurements. (a) Second-order correlation function measurements $g^{(2)}[\tau]$ (dots) for indicated drive amplitudes Ω_R and master equation calculation with and without accounting for finite measurement bandwidth (gray and black lines, respectively), discussed in Appendix C.1.2. (b) $g^{(2)}[\tau]$ for a thermal field with mean photon number $\langle n_{th} \rangle \sim 1.4$ in the resonator. (c) $g^{(2)}[\tau]$ for a coherent drive with $\langle n_c \rangle \sim 1$.

ure 4.3(b)]. The quasi-thermal field distribution was realized by mixing a fixed frequency microwave tone with a large bandwidth white noise source (Fink *et al.*, 2010). We clearly observe bunching $g^{(2)}[0] = 2$ of the thermal radiation emitted from the resonator. $g^{(2)}[\tau]$ approaches unity on the time scale of the cavity decay rate $\kappa/2\pi$ also considering the finite detection bandwidth; compare Appendix C.1.2. Performing a similar experiment with a coherent source derived from a strongly attenuated commercial microwave generator populating the resonator with $\langle n_{\mathrm{c}} \rangle \approx 1.0$, we find $g^{(2)}[\tau] = 1$ everywhere [Figure 4.3(c)], which is in good agreement with the temporal statistics of a coherent source.

In summary, we have performed correlation function measurements with linear quadrature amplitude detectors in the microwave frequency domain demonstrating photon blockade in a circuit QED system. The system effectively behaves as a single two-level atom in free space but Rayleigh scattering and resonance fluorescence is emitted predominantly into a single mode. We have also shown bunching of thermal photons and probed the second-order correlation function of coherent radiation. For the following chapter, we have implemented a triggered single-photon source, which emits not a continuous stream of single-photons as here but pulses each containing a single photon.

5

Pulsed Single Photons

In Chapter 4 we discussed the generation and characterization of a continuous stream of single photons. Here, we implement a triggered single-photon source that emits a radiation pulse on demand containing a single photon. The single photon source is integrated with a 50/50 beam splitter on the same chip. Both outputs of the beam splitter are followed by a independent heterodyne detection chain, as discussed in Sections 3.1 to 3.4. We demonstrate various possibilities of analysis for the field by measuring and efficiently processing the complex amplitude; compare Sections 3.5, 3.8 and 3.9. We investigate the temporal profile of field and power of the triggered single-photons. Further, we clearly observe single-photon coherence in first-order and photon antibunching in second-order correlation function measurements of the propagating fields (Bozyigit *et al.*, 2011a).

5.1 Triggered Single-Photon Source

For our experiments, presented here and in Chapter 6, we integrate microwave frequency single-photon sources, similar to the one presented in (Houck *et al.*, 2007), with a 50/50 beam splitter (Gabelli *et al.*, 2004; Mariantoni *et al.*, 2010) on a chip (Pozar, 2011; Frey,

	(a)	(b)	(c)
ν_r	6.763 GHz	7.2506 GHz	7.2506 GHz
$\kappa/2\pi$	4.0 MHz	4.1 MHz	4.6 MHz
$g/2\pi$	73 MHz	169 MHz	177 MHz
ν_a	8.052 GHz	8.575 GHz	8.970 GHz
$E_{\mathrm{J}\Sigma}$	20.7 GHz	27.3 GHz	26.5 GHz
E_c	462 MHz	416 MHz	419 MHz
σ	3 ns	5 ns	5 ns
$1/\gamma$	1.0 µs	0.9 µs	1.0 µs
$1/\gamma_2^*$	0.4 µs	0.4 µs	0.6 µs

Table 5.1: Experimental parameters of triggered single-photon sources. Parameters in column (a) are used in Sections 5.2 and 5.3 and columns (b) and (c) are used in Chapter 6.

2008) into a single superconducting electronic circuit (Bozyigit *et al.*, 2011a; Lang *et al.*, 2013b). We coherently and controllably couple a single transmon qubit to an asymmetric high quality resonator to emit an individual photon on demand into a single output mode $\hat{a}'$, for which we use the sample shown in Figure 2.3. At the same time, this mode is one of the two input modes of the microwave frequency beam splitter with the other mode $\hat{b}'$ prepared approximately in the vacuum state using an attenuator thermalized at 20 mK. The microwave beam splitter creates two equal amplitude output modes $\hat{a}$ and $\hat{b}$ and obeys the usual quantum optics input-output relations; compare Section 2.5. The transition frequency of the qubit is flux tunable using both a quasi-static magnetic field generated with a miniature coil and an on-chip flux bias line (purple) to generate nanosecond time scale flux pulses; see left inset in Figure 2.3.

We implement the single-photon source using the following scheme with the corresponding experimental parameters listed in Table 5.1. Applying a phase controlled truncated Gaussian microwave pulse of variable pulse amplitude Ω_R, standard deviation σ, and total duration of 4σ resonant to the qubit biased at transition frequency ν_a,

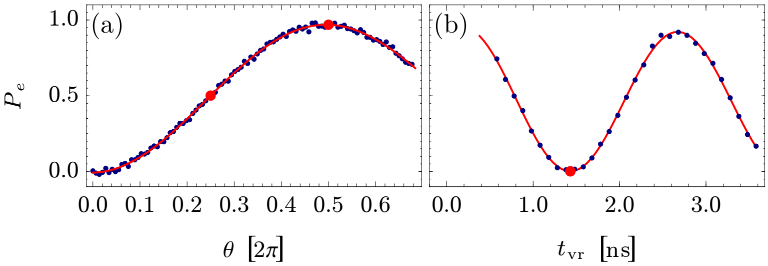

Figure 5.1: (a) Qubit state preparation by applying a resonant microwave pulse with varied pulse amplitude to the charge gate line to prepare any desired Rabi angle θ. The red dots mark the pulse amplitudes for (i) the superposition state $|+\rangle = (|g\rangle + |e\rangle)/\sqrt{2}$ and (ii) the state $|e\rangle$. (b) Vacuum Rabi oscillation when applying a flux pulse with varied length through the flux gate line. The red dot marks the $\pi/2$-vacuum Rabi pulse.

we prepare the qubit in an arbitrary superposition state $|\psi_{\mathrm{a}}\rangle = \cos(\theta/2)\,|g\rangle + \sin(\theta/2)e^{i\phi}\,|e\rangle$; compare Figure 2.7 and Section 2.4.2. We characterize the qubit state using a pulsed dispersive measurement of the resonator transmission (Section 2.4.1) and clearly observe Rabi oscillations in the qubit population P_e *vs.* the amplitude Ω_{R} and thus the Rabi angle θ, shown in Figure 5.1(a). After the qubit state preparation, we apply a current pulse of controlled amplitude and duration to the flux bias line to tune the qubit transition frequency into resonance with the resonator frequency ν_{r}. We time-resolve the resonant vacuum Rabi oscillations of the coupled system at a frequency of $2g/2\pi$ by dispersively measuring the qubit state after it has been tuned back to the frequency ν_{a} strongly detuned from the resonator; see Figure 5.1(b). Adjusting the effective qubit-resonator interaction time $t_{\mathrm{vr}} = \pi/(2g)$ to half a vacuum Rabi period, we coherently map the qubit state $|\psi_{\mathrm{a}}\rangle$ to an equivalent superposition state $|\psi_{\mathrm{r}}\rangle = \cos(\theta/2)\,|0\rangle + \sin(\theta/2)e^{i\phi}\,|1\rangle$ of the $|0\rangle$ and $|1\rangle$ photon Fock states stored in the resonator mode $\hat{A}$. Similar techniques have been used to prepare and measure a wide range of intra-cavity photon superposition states in experiments both with superconducting circuits (Hofheinz *et al.*, 2009) and with Rydberg atoms (Deleglise *et al.*, 2008). The resonator excitation $|\psi_\mathrm{r}\rangle$ in mode $\hat{A}$ is then emitted with rate κ into mode $\hat{a}'$ to the beam splitter input. The radiation at the output modes $\hat{a}$ and $\hat{b}$ of the beam splitter is measured simultaneously by two independent heterodyne detection chains as pioneered by Gabelli *et al.* (2004). Although the heterodyne detection necessarily adds noise to the signal, we are able to use the two complex amplitudes $S_a[t]$ and $S_b[t]$ to acquire valuable information about the properties of the quantum radiation sources as demonstrated in the following.

5.2 Time Dependence of Field and Power Measurements

As a first example, we present a measurement of the time dependence of the complex amplitude of the electric field in one output mode $\hat{a}$ of the beam splitter. Ensemble averaging over 10^7 realizations gives us access to the expectation value of the annihilation operator of the cavity field $\langle S_a\rangle[t] \propto \langle\hat{A}\rangle[t]$ (da Silva *et al.*, 2010). Similar measurements performed directly at the output of the cavity without a beam splitter were presented in Houck *et al.* (2007), where the cavity photon was created by Purcell limited spontaneous emission. Figure 5.2(a) shows the real part of $\langle S_a\rangle[t]$ *vs.* time t after the preparation of the photon superposition state $|\psi_\mathrm{c}\rangle$ characterized by the Rabi angle θ used for its preparation. We find excellent agreement with the expected ensemble average of the field $\langle\hat{a}\rangle \propto \sin(\theta)/2$ [Figure 5.2(c)]. In particular, we observe the largest signals for the superposition states $|\pm\rangle = (|0\rangle \pm |1\rangle)/\sqrt{2}$ prepared using $\theta = \pi/2$ and $3\pi/2$, respectively. As expected from the uncertainty principle, the Fock states $|0\rangle$ and $|1\rangle$ prepared with $\theta = 0$ and π, respectively, do not show any signal in the average complex amplitude [Figure 5.2(a)] since the phase of these number states is completely uncertain. For all of the above measurements, the overall global phase of the signals is adjusted such that the imaginary part of $S_a(t)$ is equal to zero which therefore

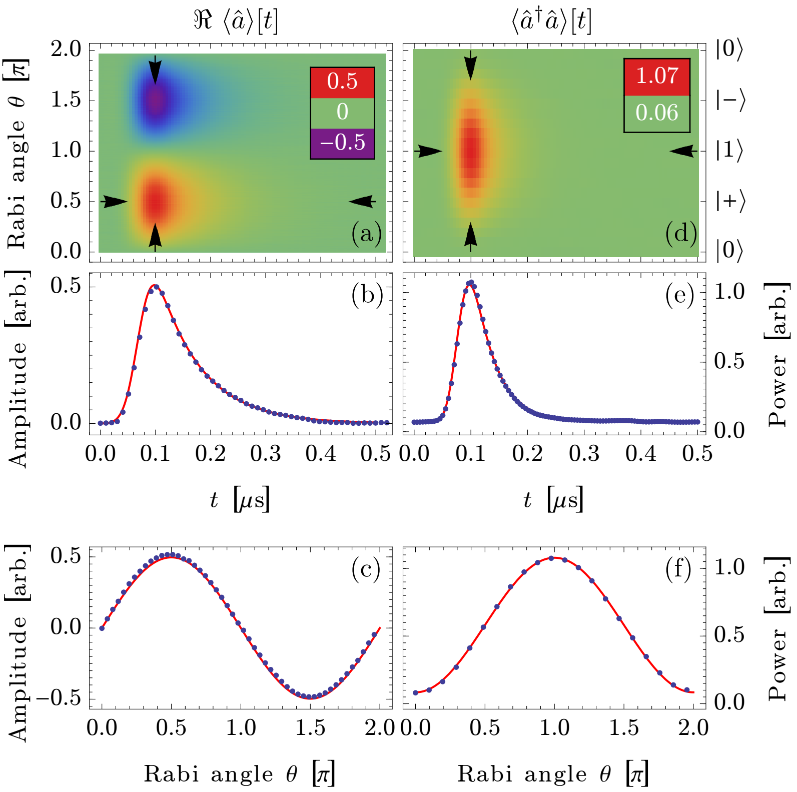

Figure 5.2: Complex amplitude and cross-power measurements. (a) Real part of $\langle S_a\rangle[t]$ for zero and one photon superposition states characterized by the Rabi angle θ (left axis) or equivalently the generated state (right axis). (b) Trace at $\theta = \pi/2$ corresponding to $|+\rangle$ [horizontal arrows in (a)]. (c) Dependence on θ at time t indicated by vertical arrows in (a). (d) Cross-power $\langle S_a^* S_b\rangle[t]$ for the same preparation as in (a). (e) Trace at $\theta = \pi$ corresponding to $|1\rangle$ [horizontal arrows in (d)]. (f) Dependence on θ at time t indicated by vertical arrows in (d). Blue dots are data, red lines are models explained in the text.

is not displayed. We also note that the amplifier noise averages to zero in the complex amplitude measurement.

Moreover, the time dependence of all measurement traces is well understood; see for example the state $|+\rangle$ in Figure 5.2(b). A model, introduced in Appendix C.2.1, accounting for an exponential decay with time constant $2T_\kappa = 2/\kappa = 80\,\mathrm{ns}$ and the limited detection bandwidth of 15 MHz explains the temporal shape of the data accurately (red line). Note that the rise time is not limited by the state-preparation time $t_{\mathrm{vr}} = 3.4\,\mathrm{ns}$ but by the detection bandwidth.

In our measurement scheme, we simultaneously record the time dependent complex amplitudes $S_a[t]$ and $S_b[t]$ detected at both output ports of the beam splitter continuously for *each* single photon generated. Using input-output theory (Gardiner and Collett, 1985), one can show that the full information about the intra-cavity mode $\hat{A}$ is contained in the moments and cross-correlations of $S_a[t]$ and $S_b[t]$ (da Silva *et al.*, 2010). Conventionally, the statistical moments of this kind of complex amplitude data are associated with the statistical moments of antinormally ordered field operators (Walls and Milburn, 2008). In many cases, however, one is used to work with normally ordered expectation values such as photon number, first- and second-order correlation functions. We demonstrate that these moments can be obtained efficiently by applying the correct algebraic transformations on the full measurement record $S_a[t]$ and $S_b[t]$ of the two detection chains before performing ensemble averaging (da Silva *et al.*, 2010; Grosse *et al.*, 2007), which we realize as presented in Chapter 3.

Taking advantage of this versatile scheme, we digitally calculate—instead of using a diode as a power meter in which the detection and the averaging is realized within the detector (Houck *et al.*, 2007)—the expectation value of the instantaneous power $\langle S_a^* S_a\rangle[t]$ transmitted into one output mode $\hat{a}$ of the beam splitter with the cavity mode $\hat{A}$ prepared in the Fock state $|1\rangle$ (not shown). In the direct power measurement, the detected noise power of the amplifier dominates by a factor of about 700 over the single photon power which is still observable using sufficient averaging. From this measured background noise we determine the system noise temperature $T_{\mathrm{n}} \approx 11\,\mathrm{K}$ of our detection chain with respect to the output of the resonator. T_n is substantially higher than the noise temperature of the amplifiers because of absorption in the cables and insertion loss of components in the detection chain.

Calculating the cross-power $\langle S_a^* S_b \rangle[t]$ between the two output modes of the beam splitter instead of the direct power detected in just a single mode, we can effectively reject the noise added by the amplifiers in our measurement scheme. The detected cross-power is related to the average photon number in the cavity as

$$\langle S_a^* S_b \rangle[t] \propto \langle \hat{A}^\dagger \hat{A} \rangle[t] + P(N_{ab})$$

(da Silva *et al.*, 2010), where $P(N_{ab})$ is the power of correlated noise between channels $\hat{a}$ and $\hat{b}$. In these measurements, the detected noise cross-power has a characteristic noise temperature of only 80 mK, much smaller than the characteristic noise temperature of the direct noise power of each amplifier, indicating that the two detection chains add predominantly uncorrelated noise. The residual correlations result from weak thermal radiation at the vacuum port $\hat{b}'$ and technical origins, such as insufficient isolation of the two detection chains.

We have characterized the measured cross-power of our single photon source for the same set of cavity superposition states as used for the complex amplitude measurements averaging over 6.7×10^8 photon state preparations [Figure 5.2(d)]. We find excellent agreement of the temporal evolution of the cavity photon number [Figure 5.2(e); compare Appendix C.2.1 for the expected power] in dependence on the preparation angle of the photon state $\langle \hat{a}^\dagger \hat{a} \rangle \propto \sin^2(\theta/2)$ [Figure 5.2(f)]. The maximum cross-power is measured for the Fock state $|1\rangle$ $(\theta = \pi)$ and the minimum power for the $|0\rangle$ state ($\theta = 0$ or 2π) [Figure 5.2(d)].

5.3 Measurement of Correlation Functions

We have characterized our single photon source using measurements of the time-dependent first-order cross-correlation

$$\mathit{\Gamma}_{ab}^{(1)}[\tau] = \langle S_a \star S_b \rangle[\tau]$$

of the signals S_a and S_b in the two output modes and the auto-correlation of the cross-power

$$\Gamma_{ab}^{(2Y)}[\tau] = \langle (S_a^* S_b) \star (S_a S_b^*) \rangle [\tau] \ ;$$

compare Section 3.9. Here, $\Gamma_{ab}^{(1)}$ is a direct measure of the first-order correlation function $G^{(1)}$ while $\Gamma_{ab}^{(2Y)}$ is a direct measure of the second-order correlation function $G^{(2)}$ of the resonator field as derived in Appendices B.2 and B.5.

For the measurement, we generate a 20.48 µs long train of 40 single photon pulses each generated using the procedure described above and with a photon repetition period $t_\mathrm{r} = 512\,\mathrm{ns}$ which is much greater than the cavity decay time. To remove a small correlated noise background, we subtract the measured correlation function $H_{ab}^{(1)}[\tau]$ in the resonator steady-state from the signal $\Gamma_{ab}^{(1)}[\tau]$ acquired when performing the photon state preparation sequence. From the recorded quadrature amplitude data, we calculate

$$\Gamma_{ab}^{(1)}[\tau] - H_{ab}^{(1)}[\tau] \propto G^{(1)}[\tau] \ ,$$

which gives us access to the first-order correlation function $G^{(1)}[\tau]$ of the resonator field $\hat{A}$ (da Silva *et al.*, 2010). To measure each trace in Figure 5.3(a), 64×10^6 trains of 40 photons were prepared in a specific state and $G^{(1)}[\tau]$ was calculated in real-time using our FPGA based electronics, corresponding to approximately 0.5 Tbyte of data that have been evaluated in about 30 min.

The $G^{(1)}[\tau]$ data [Figure 5.3(a)] is characterized by a set of peaks that are separated by the repetition time t_r of the single-photon generation. The amplitude of $G^{(1)}[nt_\mathrm{r}]$ at integer non-zero multiples of t_r, representing the correlation between a pulse i and $i+n$, depends in a characteristic fashion on θ. For the Fock state $|1\rangle$ (at $\theta = \pi$) the correlation function $G^{(1)}[0]$ is at a maximum and vanishes at $G^{(1)}[nt_\mathrm{r}]$ as there is no coherence between photons emitted from the source at different times. In fact, $G^{(1)}[0] \propto \langle \hat{A}^\dagger \hat{A} \rangle = \sin^2(\theta/2)$ oscillates sinusoidally with the preparation angle, as it essentially measures the average photon number of the generated field [Figure 5.3(b)]. However,

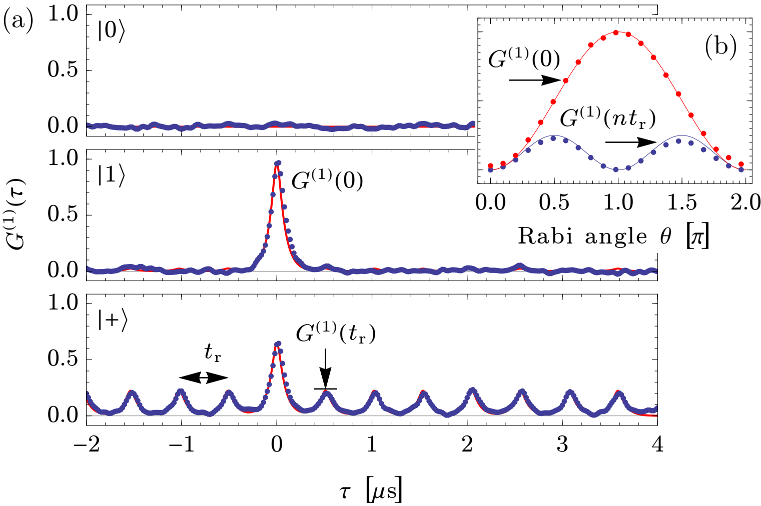

Figure 5.3: (a) Time dependence of first-order correlation function $G^{(1)}[\tau]$ of the cavity field for indicated states. (b) $G^{(1)}(0)$ and $G^{(1)}(nt_r)$ *vs.* θ. In all panels dots are data and lines are theoretical predictions (da Silva *et al.*, 2010).

for photon superposition states, the expectation values of $\langle \hat{A}^\dagger \rangle$ and $\langle \hat{A} \rangle$ of subsequently generated photon states have non-vanishing values, as discussed in Section 5.2. Since photons from different repetitions of the experiments are uncorrelated, $G^{(1)}[nt_r] \propto \langle \hat{A}^\dagger \rangle \langle \hat{A} \rangle$ has a finite value and oscillates at half the period. Thus, $G^{(1)}[nt_r] \propto \sin^2(\theta)/4$ is maximized for the states $|\pm\rangle$ [Figure 5.3(b)].

The observed features of the first-order correlation function together with the results in Figure 5.2 confirm that the procedure implemented for generating single-photon pulses performs as expected. Measurements of the second-order correlation function $G^{(2)}[\tau]$ then do provide unambiguous proof of the quantum character of the generated propagating field, independent of any prior knowledge about its source (Walls and Milburn, 2008). Based on the results presented

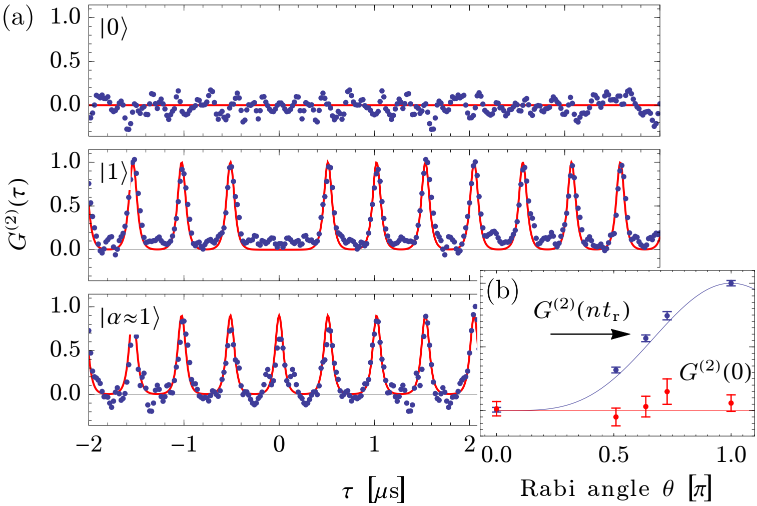

Figure 5.4: (a) Measured second-order correlation function $G^{(2)}[\tau]$ of the states $|0\rangle$ (top trace), $|1\rangle$ (middle trace) and a coherent state $|\alpha \approx 1\rangle$ (bottom trace). Note that the noise in these measurements is symmetric around $\tau = 0$. (b) $G^{(2)}(0)$ and $G^{(2)}(nt_r)$ *vs.* qubit preparation angle θ. Blue error bars are the inferred standard deviation of the mean $G^{(2)}(nt_r)$. Red error bars are the estimated standard deviation of $G^{(2)}(0)$. In all panels dots are data and lines are theoretical predictions, discussed in Appendix C.2.2 (da Silva *et al.*, 2010).

in da Silva *et al.* (2010) we obtain the second-order correlation function $G^{(2)}[\tau]$ by measuring

$$\Gamma_{ab}^{(2Y)}[\tau] - H_{ab}^{(2Y)}[\tau] \propto G^{(2)}[\tau]\,,$$

where $H_{ab}^{(2Y)}[\tau]$ is the steady-state measurement, as shown in Appendix B.5. Measurements of $G^{(2)}[\tau]$ averaged over 5×10^9 to 9×10^9 trains of 40 photon state preparations are shown in the three panels of Figure 5.4(a). For the vacuum state $|0\rangle$ we find $G^{(2)}[\tau] = 0$

everywhere, as expected. For the Fock state $|1\rangle$ we observe a characteristic set of peaks in $G^{(2)}[\tau]$ spaced by the repetition time t_{r} of the source with a strongly suppressed peak $G^{(2)}[0] \approx 0.1 \ll 1$ at zero delay time τ, as expected from theoretical predictions (red line) calculated in Appendix C.2.2 (da Silva *et al.*, 2010). This measurement clearly demonstrates antibunching of the radiation emitted by our single-photon source as $G^{(2)}[0] \ll G^{(2)}[nt_{\mathrm{r}}]$. At the same time these measurements demonstrate that the non-classical properties of the radiation are fully retained in the detection process in form of statistical correlations between the single-shot complex amplitudes detected behind the beam splitter.

To further compare our results with the theoretical predictions, we have performed the same $G^{(2)}[\tau]$ measurement for three additional photon superposition states as parameterized by the Rabi angle θ. Here we note that $G^{(2)}[\tau]$ is normalized such that the average peak height for the prepared state $|1\rangle$ is equal to unity. For all prepared states we observe the expected scaling of $G^{(2)}[nt_{\mathrm{r}}] \propto \sin^4(\theta/2)$ and $G^{(2)}[0] \approx 0$ [see Figure 5.4(b)] confirming the measurement of antibunching.

Finally, we have applied short coherent pulses at ν_{r} to the resonator input to realize a coherent source with approximately the same average intensity as the single photon source. In a measurement of $G^{(2)}[\tau]$ we find the expected periodic pattern with a peak of amplitude ≈ 0.9 present also at $\tau = 0$ [Figure 5.4(a) bottom trace] which is in stark contrast to the $|1\rangle$ photon Fock state.

In summary, the experiments presented in this chapter clearly demonstrate that correlation function measurements based on quadrature amplitude detection are a powerful tool to characterize quantum properties of propagating microwave frequency radiation fields. Even in the presence of noise added by the amplifier, two-channel detection and efficient data processing techniques allow for the measurements of higher statistical moments of the fields. Two of such triggered single-photon sources that were investigated here are used in the next chapter to explore the interference of two independently generated single microwave photons at a beam splitter.

6

Hong-Ou-Mandel Experiments

The Hong, Ou, and Mandel (HOM) effect describes a two-photon interference effect observable in quantum optics. The effect was first experimentally observed by Hong, Ou, and Mandel (1987) and occurs, when two indistinguishable single photons impinge at the two inputs of a balanced beam splitter. Due to the bosonic nature of photons, they coalesce into a pair of photons appearing in either one of the two outputs of the beam splitter. Here, we describe the observation of the HOM effect with two independent, triggered single-photon sources in the microwave frequency domain. We probe the indistinguishability of single photons, created with a controllable delay, in time-resolved second-order cross- and auto-correlation function measurements. Using independent heterodyne detection chains at the outputs of the beam splitter we are able to resolve different photon numbers and detect coherence in and between the output arms. This measurement scheme allows us to observe the HOM effect and, in addition, to fully characterize the two-mode entanglement of the spatially separated beam splitter output modes (Lang *et al.*, 2013b). Our experiments constitute a first step towards using two-photon interference at microwave frequencies for quantum communication and information processing, e.g. for distributing entanglement between nodes of a quantum network (Kimble, 2008; Duan and Monroe, 2010) and for linear optics quantum computation (Knill, Laflamme, and Milburn, 2001; O'Brien, Furusawa, and Vučković, 2009).

6.1 Two-Photon Interference

Up until the experiments presented in this thesis, HOM two-photon interference has been demonstrated exclusively using photons at optical or telecom wavelengths. Experiments were performed with photons emitted from a single source using parametric down conversion (Hong, Ou, and Mandel, 1987), trapped ions (Duan and Monroe, 2010), atoms (Legero *et al.*, 2004), quantum dots (Santori *et al.*, 2002) and single molecules (Kiraz *et al.*, 2005). The HOM effect has also been observed with two independent sources (Riedmatten *et al.*, 2003; Kaltenbaek *et al.*, 2006; Beugnon *et al.*, 2006; Maunz *et al.*, 2007; Flagg *et al.*, 2010; Patel *et al.*, 2010; Lettow *et al.*, 2010) realizing indistinguishable single-photon states which are required as a resource in quantum networks or linear optics quantum computation. Such experiments have also been performed using donor impurities as sources (Sanaka *et al.*, 2009) including NV-centers in diamond (Sipahigil *et al.*, 2012; Bernien *et al.*, 2012). Furthermore, the HOM effect has been employed to create entanglement between ions (Moehring *et al.*, 2007) and atoms (Hofmann *et al.*, 2012) in spatially separated traps, between separated NV-centers (Bernien *et al.*, 2013), and to realize a controlled-NOT gate in a small-scale photonic network (Shadbolt *et al.*, 2012). Similar physics is also actively explored with ballistic electrons in solids; see Bocquillon *et al.* (2013) and references therein.

We demonstrate the HOM interference of two indistinguishable microwave photons emitted from independent triggered sources realized in superconducting circuits, as presented in Section 5.1 having experimental parameters listed in Table 5.1 columns (b) and (c). The photons are prepared in two separate microwave resonators $A\,(B)$ using transmon-type qubits and decay exponentially at rate $\kappa/2\pi = 4.1\,(4.6)\,\mathrm{MHz}$ through their strongly coupled output ports into the input modes $\hat{a}'$ and $\hat{b}'$ of the beam splitter; see Figures 6.1 and 6.2. The

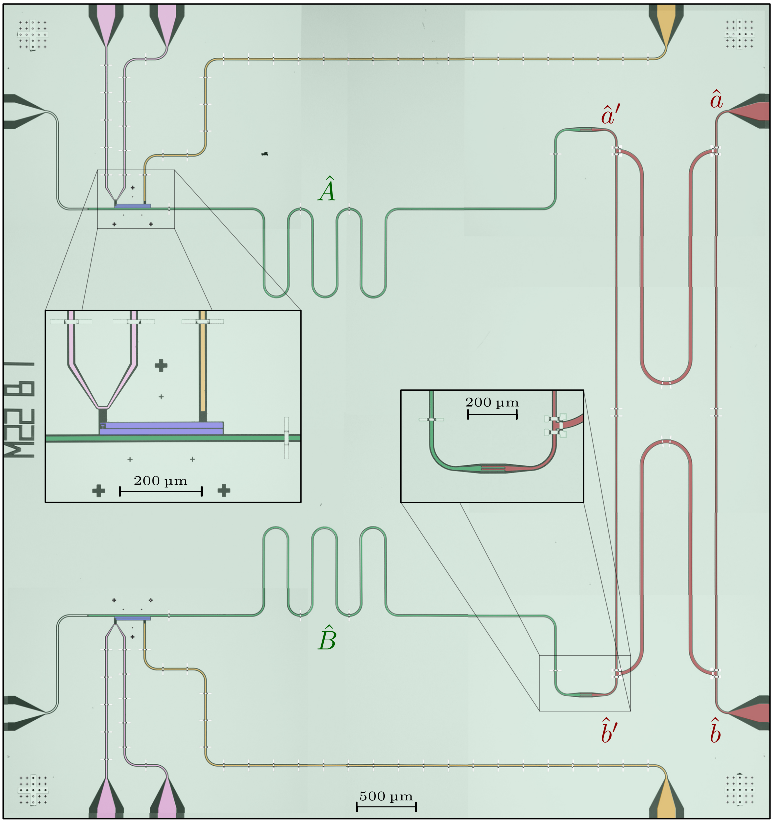

Figure 6.1: False color micrograph of the HOM device. A transmon qubit (blue, left inset) controlled by a flux (purple) and charge gate line (orange) through which current or microwave pulses are applied, respectively, is coupled to each coplanar waveguide resonator (green) with fundamental mode $\hat{A}\,(\hat{B})$. The coupling rate of the input port of the asymmetric resonator is by a factor of 10^3 smaller than at the output port. Each resonator output is coupled to the input mode $\hat{a}'$ $(\hat{b}')$ (right inset) of a microwave beam splitter (dark red) with two output modes $\hat{a}\,(\hat{b})$.

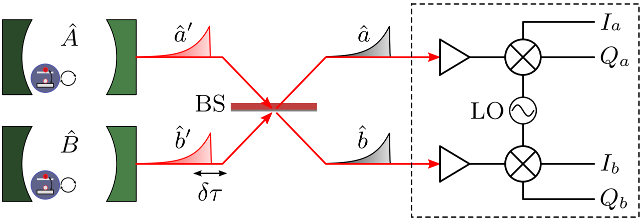

Figure 6.2: Schematic of the HOM experiment with two individual cavity QED systems for photon generation, a beam splitter (BS), and linear amplification and heterodyne detection.

two photons then interfere at the beam splitter and are emitted into the output modes $\hat{a}$ and $\hat{b}$; see Figure 6.1. Using the dispersive interaction between qubit and resonator, we tune the emission frequencies of the two sources to an identical value of $\nu_\mathrm{r} = 7.2506\,\mathrm{GHz}$. Thus, the measured power spectral densities PSD$[\nu]$ of the generated photons from the two sources match well, as shown in Figure 6.3. A small discrepancy is explained due to different photon emission rates κ and generation efficiency. For our experiments, we sequentially create 20 single photons in each source at a rate $1/t_\mathrm{r} = 1/512\,\mathrm{ns} \sim 1.95\,\mathrm{MHz}$ in a sequence repeated every $T_\mathrm{p} = 12.5\,\mu\mathrm{s}$.

To probe the photon statistics in the beam splitter output modes $\hat{a}$ and $\hat{b}$ we use two spatially separated heterodyne detection chains; see dashed box in Figure 6.2. Each chain extracts the two quadratures $I_{a/b}[t]$ and $Q_{a/b}[t]$ corresponding to the time-dependent complex amplitude $S_{a/b}[t] = I_{a/b}[t] + i\,Q_{a/b}[t]$; compare Sections 3.1 to 3.4. In contrast to many other HOM experiments in which photons in the beam splitter outputs are detected by single-photon counters, our measurement of the complex amplitude is intrinsically photon-number resolving for averaged measurements and allows us to measure coherences of the electromagnetic field. The complex amplitudes $S_{a/b}[t]$ are used to compute the statistics required to extract all relevant quantum correlations measured here; see Sections 3.5, 3.9 and 3.10. The noise added by the detection chain is fully characterized by measuring its

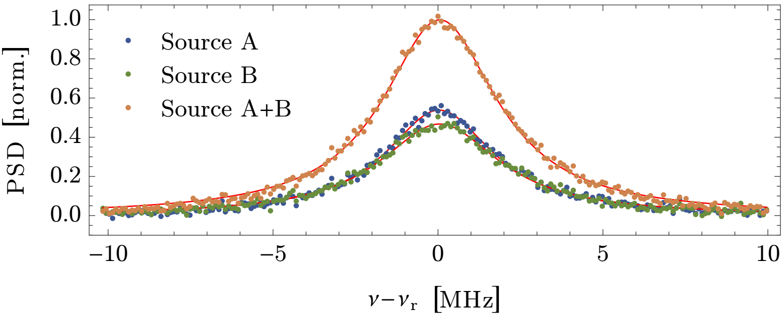

Figure 6.3: Power spectral density (PSD) of triggered single-photon sources for each source individually and both sources simultaneously. Dots are data and the lines are fits to a Lorentzian with amplitude, center frequency, and $\kappa/2\pi$ as free parameters.

statistical properties when the output modes $\hat{a}$ and $\hat{b}$ of the beam splitter are left in the vacuum state with both sources idle (da Silva *et al.*, 2010; Eichler, Bozyigit, and Wallraff, 2012). To verify the single-photon character of each source individually, we have measured their second-order cross-correlation functions $G^{(2)}_{ab}[\tau]$, which display clear antibunching [Figure 6.4(a,b)] as expected from Section 5.3.

6.2 Measurement of Photon Statistics

To investigate two-photon quantum interference, we simultaneously generate two indistinguishable photons ideally realizing a two-mode entangled state $(|20\rangle + |02\rangle)/\sqrt{2}$ at the beam splitter outputs. The measured cross-correlation of the beam splitter output powers is observed to vanish $G^{(2)}_{ab}[\tau] \approx 0$ for all τ between $-t_\mathrm{r}/2$ and $t_\mathrm{r}/2$; see colored region in Figure 6.4(c). This means that both microwave frequency photons coalesce at the beam splitter, which is the HOM effect with microwave photons. In our experiments the temporal coherence of the single-photon states is governed by resonator decay

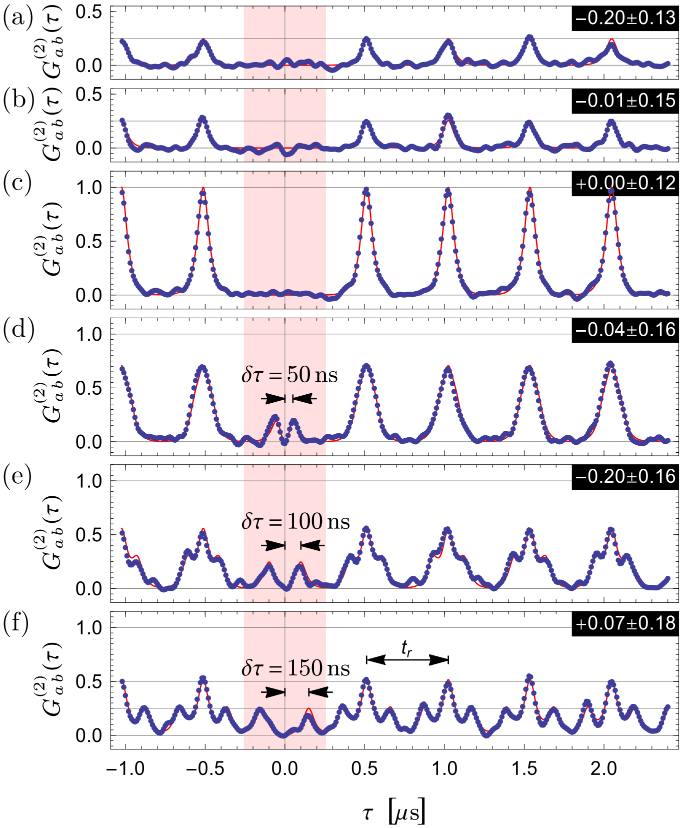

Figure 6.4: Cross-correlation $G_{ab}^{(2)}[\tau]$ of individual single photon sources displaying single photon antibunching, source A in panel (a) and B in panel (b). (c-f) $G_{ab}^{(2)}[\tau]$ when operating both sources simultaneously with delay times $\delta\tau = 0, 50, 100, 150\,\mathrm{ns}$ displaying the HOM effect and its dependence on the temporal photon overlap at the beam splitter. Blue dots are data and red lines are theory. Residual offsets with their confidence intervals subtracted from the data are indicated in the upper right corner of each panel.

alone, and shows no significant additional dephasing. This is in stark contrast to many other experiments in which decoherence resulting in random frequency differences between interfering photons causes finite correlations at $\tau \sim 0$ (Legero *et al.*, 2004; Beugnon *et al.*, 2006; Flagg *et al.*, 2010). At $\tau = n\,t_\mathrm{r}$ ($n = \pm1, \pm2, \ldots, \pm10$), the peak at integer non-zero multiples of the photon generation period reflects the product of the power in each output $\langle \hat{a}^\dagger \hat{a} \rangle \langle \hat{b}^\dagger \hat{b} \rangle$ which we have normalized to one.

All measured second-order correlation functions in Figures 6.4 and 6.5 are reconstructed as shown in Appendices B.3 and B.4, and are normalized by a common scaling factor and a relative gain between the two amplification channels. A remaining small offset subtracted from the reconstructed correlation functions is indicated together with its standard deviation (extracted from multiple measurements) in the upper right corner of each panel. This offset results from the finite statistical uncertainty of measured first-order correlation terms (da Silva *et al.*, 2010) and is expected to vanish in the limit of infinite averaging. The measured second-order correlation functions are in good agreement with analytical calculations (solid lines), see Appendix C.2.2 and Woolley *et al.* (2013), taking into account the cavity decay rates κ extracted from independent measurements and a fixed detection bandwidth of 20 MHz chosen to reject experimental noise outside the desired band.

To explore the level of indistinguishability between the two interfering photons we introduce a time delay $\delta\tau$ on the order of the photon decay time $1/\kappa \sim 37\,\mathrm{ns}$. For $\delta\tau = 50\,\mathrm{ns}$ [Figure 6.4(d)] the second-order cross-correlation function remains close to zero at $\tau = 0$, indicating the coalescence of those photons detected with vanishingly small time difference (Woolley *et al.*, 2013; Legero *et al.*, 2003, 2004). Typically this effect is difficult to observe with detectors of insufficient bandwidth or sources with significant dephasing rates (Flagg *et al.*, 2010). The small positive correlations observed at $\tau \sim \delta\tau$ are due to the decreased temporal overlap of the single-photon temporal mode functions at the beam splitter, i.e. the increased distinguishability of the two photons. At $\tau \sim n\,t_\mathrm{r}$ we observe broadened, lower amplitude correlations. All features are in agreement with theoretical predictions

(Appendix C.2.2); compare solid lines in Figure 6.4(d).

For $\delta\tau = 100\,\mathrm{ns}$ and $\delta\tau = 150\,\mathrm{ns}$ the envelopes of the two single-photon mode functions barely overlap at the beam splitter, resulting in fully distinguishable single photons. At $\tau = \pm\delta\tau$ and $\tau = n\,t_\mathrm{r} \pm \delta\tau$ [see Figure 6.4(f)] we observe positive correlations with an amplitude 1/4, which originate from single photons impinging on the beam splitter at different times and at different input arms described by lines two and three in Equation (C.3); compare Figure 6.4(a,b). At $\tau = n\,t_\mathrm{r}$ the correlations between photons in the same beam splitter input arm sum up to 1/2, as expected from the first two terms in Equation (C.3).

To clearly distinguish between single-photon antibunching and two-photon coalescence in time-resolved correlation function measurements, we also measured the second-order auto-correlation function $G^{(2)}_{aa}[\tau]$ of mode $\hat{a}$. When operating only one single-photon source $G^{(2)}_{aa}[0]$ is expected to vanish. However, in the HOM configuration with $\delta\tau = 0$ we find $G^{(2)}_{aa}[0] = G^{(2)}_{aa}[n\,t_\mathrm{r}] = G^{(2)}_{ab}[n\,t_\mathrm{r}] = 1$ [see Figure 6.5(a)] as there is a 50% probability of detecting two photons in mode $\hat{a}$. All measurements of $G^{(2)}_{aa}[\tau]$ are in good agreement with calculations (Appendix C.2.2), both for $\delta\tau = 0$ and for $\delta\tau = 100\,\mathrm{ns}$ (solid lines in Figure 6.5). Here, it is interesting to note that a second-order auto-correlation function is rarely directly measured, because of the the lack of sufficiently fast single-photon detectors (Steudle *et al.*, 2012). In contrast, using our detection scheme, presented in Chapter 3, we are capable of measuring $G^{(2)}_{aa}[\tau]$ for multi-photon states.

6.3 Observation of Spatial Entanglement

To distinguish between an equal mixture of the states $|20\rangle$ and $|02\rangle$, compatible with the observed correlations, and their coherent superposition $(|20\rangle + |02\rangle)/\sqrt{2}$, we fully characterize the two-photon states created in our HOM experiment by quantum state tomography. This allows us to probe the entanglement generated between the coalescing two-photon states in the two output ports of the beam splitter. The

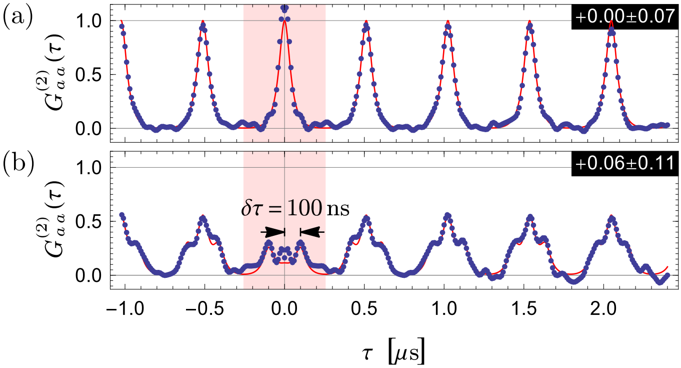

Figure 6.5: Second-order auto-correlation $G^{(2)}_{aa}[\tau]$ of mode $\hat{a}$ for $\delta\tau = 0$ in panel (a) displaying two-photon coalescence and $\delta\tau = 100\,\mathrm{ns}$ in panel (b). Blue dots are data and red lines are theory. Residual offsets with their confidence intervals subtracted from the data are indicated in the upper right corner of each panel.

created states are also referred to as NOON states. In contrast to the NOON states of propagating photons investigated here, NOON states have also been investigated in superconducting circuits with photons localized in resonators (Wang *et al.*, 2011; Nguyen *et al.*, 2012).

To perform full quantum state tomography on propagating photons in the two spatially separated modes, we record four-dimensional histograms of the measured quadratures I_a, Q_a, I_b, and Q_b, as discussed in Section 3.10. From these measurements we extract all moments of the two-mode field, i.e. expectation values of the form $\langle(\hat{a}^\dagger)^n\hat{a}^m(\hat{b}^\dagger)^k\hat{b}^l\rangle$ with $n, m, k, l \in \{0, 1, 2\}$. The total gain of the detection chain is calibrated by preparing an equal superposition state $(|0\rangle + |1\rangle)/\sqrt{2}$ in only one mode ($\hat{b}'$), for which we expect half a photon in mode $\hat{b}'$. In the analysis we take a residual thermal steady-state population of 0.03 in modes $\hat{a}$ and $\hat{b}$ into account.

We observe that the first-order moments and all other odd-order moments are zero since all single-photon Fock states are characterized by a fixed photon number and consequently a fully random phase; see Figure 6.6(a). Since each mode carries exactly one photon on average, $\langle \hat{a}^\dagger \hat{a} \rangle$ and $\langle \hat{b}^\dagger \hat{b} \rangle$ are close to unity, while all other second-order moments vanish. The fourth-order moment $\langle \hat{a}^\dagger \hat{a}\, \hat{b}^\dagger \hat{b} \rangle$ is observed to be zero, while $\langle \hat{a}^\dagger \hat{a}^\dagger\, \hat{a}\hat{a} \rangle$ and $\langle \hat{b}^\dagger \hat{b}^\dagger\, \hat{b}\hat{b} \rangle$ are unity, consistent with the coalescence of the two photons into either output. The above observations are consistent with the ones based on the correlation function measurements in Figures 6.4 and 6.5. Most importantly, the two-mode entanglement is indicated by the moment $\langle \hat{a}\hat{a}\hat{b}^\dagger \hat{b}^\dagger \rangle$ which is close to 1, as expected. All measured moments of the two-mode entangled state created in our HOM experiment are in good agreement with the predicted ones; see wire frames in Figure 6.6(a). Note that moments of order five and higher are all close to zero within their statistical errors.

In addition, we have determined the most likely density matrix ϱ characterizing the created two-mode entangled propagating photon state from the measured moments and their respective standard deviation following Eichler, Bozyigit, and Wallraff (2012). We have restricted the evaluation of moments to less than three photons per output mode, since we create no more than two single photons with our sources. Note that a related analysis has recently been performed by Israel *et al.* (2012). The real part of ϱ is shown in Figure 6.6(b), all elements of the imaginary part of ϱ are smaller than 0.02 (not shown). We extract a fidelity of the NOON type state of $F = \langle \psi | \varrho | \psi \rangle = 84\%$ and a negativity $\mathcal{N}(\varrho) = 0.39$ (Vidal and Werner, 2002). Inefficiencies arise predominantly from residual thermal populations of qubits and resonators which we estimate to be approximately 3%, from finite qubit coherence times and the associated imperfect cavity state preparations, as well as slight differences in the linewidth of the two resonators.

6.4 Superposition State Interference

Finally, to explore the interplay between single- and two-photon interference, we have performed experiments with modes $\hat{A}$ and $\hat{B}$ prepared

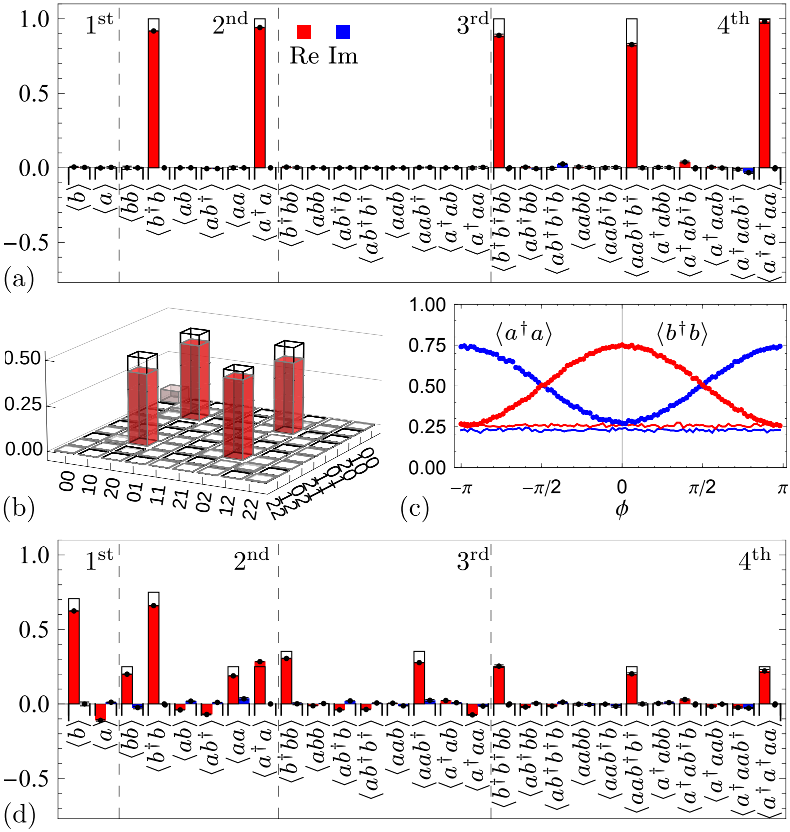

Figure 6.6: Full quantum state tomography. (a) Measured moments $\langle(\hat{a}^\dagger)^n\hat{a}^m(\hat{b}^\dagger)^k\hat{b}^l\rangle$ with $n,m,k,l\in\{0,1,2\}$ up to fourth order, and (b) density matrix (real part) for $(|20\rangle+|02\rangle)/\sqrt{2}$. Colored bars are extracted from data, error bars indicate the standard deviation and wire frames represent ideal state. (c) Power detected in the two output modes ($\langle\hat{a}^\dagger\hat{a}\rangle$, blue) and ($\langle\hat{b}^\dagger\hat{b}\rangle$, red) for operating only source B (line) or both sources (dots) creating superposition states with relative phase angle ϕ. (d) Measured moments for $(\sqrt{2}\,|00\rangle+2\,|01\rangle+|20\rangle+|02\rangle)/\sqrt{8}$.

in superpositions of $|0\rangle$ and $|1\rangle$ photon Fock states, i.e. $(|0\rangle - i\,|1\rangle)/\sqrt{2}$ and $(|0\rangle + e^{i\phi}\,|1\rangle)/\sqrt{2}$ with variable phase ϕ, ideally creating the state $\left(\sqrt{2}\,|00\rangle - i(1-e^{i\phi})\,|10\rangle + (1+e^{i\phi})\,|01\rangle + e^{i\phi}(|20\rangle + |02\rangle)\right)/\sqrt{8}$ at the beam splitter output. With these input states, we have first measured the power in the beam splitter output modes $\hat{a}$ (blue line) and $\hat{b}$ (red line) when only operating source B and keeping source A idle; see Figure 6.6(c). In this case, we observe a power level corresponding to 1/4 of a single photon independent of the phase angle ϕ, as expected for an equal superposition of $|0\rangle$ and $|1\rangle$ impinging on a balanced beam splitter. Operating both sources A and B, we observe a sinusoidal interference with phase ϕ of the two superposition states in the beam splitter output power of mode $\hat{a}$ (blue dots) and $\hat{b}$ (red dots), respectively. The sinusoidal oscillation is a result of the interference between one photon in either output port while the offset in power of 1/4 is the result of two-photon coalescence.

For the phase angle $\phi \approx 0$ we have also performed full quantum state tomography; see Figure 6.6(d). As for the two-photon NOON state we observe antibunching, coalescence, and entanglement in the moments $\langle \hat{a}^\dagger \hat{a}\, \hat{b}^\dagger \hat{b} \rangle$, $\langle \hat{a}^\dagger \hat{a}^\dagger \hat{a}\hat{a} \rangle$ and $\langle \hat{b}^\dagger \hat{b}^\dagger \hat{b}\hat{b} \rangle$, and $\langle \hat{a}\hat{a}\hat{b}^\dagger \hat{b}^\dagger \rangle$, respectively with close to expected amplitudes (wire frames). The interference of the superposition states is revealed not only in the power $\langle \hat{a}^\dagger \hat{a} \rangle$ and $\langle \hat{b}^\dagger \hat{b} \rangle$ but also in the coherences with an unbalanced number of creation and annihilation operators. The corresponding state has a fidelity of 84% with respect to the ideal one.

In summary, the flexibility of circuit design and the high level of control achievable in circuit QED enables us to implement independent sources that emit indistinguishable single photons at microwave frequencies. Making use of an integrated beam splitter we observed the HOM effect and demonstrated the hereby generated entanglement of spatially separated propagating microwave radiation. Our results suggest that multiple on-demand single-photon sources emitting indistinguishable single photons could be used for creating non-local entanglement in quantum repeater or quantum communication applications based on microwave photons.

7

Summary and Outlook

This thesis presents and describes the development of a real-time microwave frequency signal analyzer based on linear detection of complex amplitudes. Compared to commercially available digitizer boards with averaging capabilities, our framework provides customizable signal analysis, and extends the measurement possibilities to computationally intensive nonlinear signal analyses. Correlation analyses allow to investigate radiation properties unique to quantum fields including non-local correlations. At optical frequencies second-order correlation function measurements are very important for characterizing many sources of light in particular single-photon emitters. We have developed two types of microwave frequency single-photon emitters, a triggered single-photon source and a continuous source of single-photons based on photon blockade, and used our signal analyzer to display the quantum nature of the emitted radiation. The experiments performed throughout this thesis work clearly demonstrate that the linear detection of complex amplitudes combined with effective digital signal processing is a very versatile and powerful tool to characterize quantum properties of propagating microwave frequency radiation fields, even in the presence of noise added by linear amplifiers. The flexible and efficient signal processing of our signal analyzer has made it possible, to set-up a single detection framework, with which we have measured the temporal profile of field and power, and first- and second-order correlation functions of the triggered single-photon source. Furthermore, we demonstrated photon blockade by measuring power spectral densities and second-order correlation functions of the continuous single-photon source. We have also shown bunching of thermal photons and probed the second-order correlation function of coherent radiation. The developed single-photon emitters have the potential to inspire new work controlling the flow of photons, generating and detecting individual photons and investigating single-photon effects in superconducting circuits. In particular, the observation of photon blockade will enable future experimental work on photon interactions in cavity arrays that are actively theoretically investigated (Schmidt *et al.*, 2010; Hartmann, Brandao, and Plenio, 2008; Koch and Le Hur, 2009; Angelakis, Santos, and Bose, 2007; Greentree *et al.*, 2006). In these proposals, the array elements are typically nonlinear cavities, such as the ones realized in photon blockade systems. Performing a cross-correlation analysis, as presented here, of the radiation emitted from the two ends of the cavity array with the appropriate drives, may lead, for example, to the observation of Majorana-like modes of radiation in the array (Bardyn and İmamoğlu, 2012).

Finally, we demonstrated the quality and flexibility of our triggered single-photon source by implementing two independent sources emitting indistinguishable single photons integrated on a single chip with linear optics elements, such as a beam splitter. The Hong, Ou, and Mandel (HOM) single-photon interference at the beam splitter was fully characterized and the created non-local entanglement was investigated. Our results suggest that multiple of such single-photon sources together with exploiting HOM interference could be used as the key element for quantum computation protocols based on microwave photons (Knill, Laflamme, and Milburn, 2001; Kimble, 2008; O'Brien, Furusawa, and Vučković, 2009; Duan and Monroe, 2010), when effective single-photon detectors at microwave frequencies become available or with the development of new protocols exploiting other nonlinear effects in superconducting circuits.

The microwave frequency signal analyzer developed in this thesis is a useful measurement device not only within the circuit QED community but also for any system in science where a source of microwave radiation is investigated (Frey *et al.*, 2011; Puebla-Hellmann and Wallraff, 2012). The real-time processing core of our signal analyzer is a field programmable gate array (FPGA) with custom-made firmware. Thus, the signal analyzer was successfully used for real-time feedback (Steffen *et al.*, 2013) and is suitable to address future challenges, such as calibration routines, feedback loops (Ristè *et al.*, 2012), and the complete control of quantum algorithms. For characterizing propagating microwave radiation, correlations and entanglement thereof, our signal analyzer is able to use the measurement time with close to unit efficiency. I am convinced that ongoing experiments will take advantage of the versatile and flexible analysis possibilities helping to uncover unexplored phenomena of quantum microwave radiation.

A

FPGA

In most circuit QED experiments the electric field of a linearly amplified and down converted microwave signal is measured by commercially available digitizer boards with averaging capabilities. After averaging multiple realizations of an experiment, the data are transferred to a computer which analyzes the averaged signal in software. With our FPGA based electronics, we interchange the order of signal processing/analysis and averaging; see Chapter 3. After being processed by a specific analysis application which also runs on the FPGA, each single shot is analyzed individually and eventually averaged. Thus, we are able to digitally perform nonlinear operations that do not commute with the averaging process. Additionally, customized signal processing and data analysis is performed in real-time on the FPGA, which reduces data transfer and data processing time on the host computer, enabling fast real-time feedback.

In Appendix A.1, FPGA based data processing is described. Hardware details of the FPGA board programmed and used for the experiments of this thesis are given in Appendix A.2. A technical design overview of the firmware, that executes on the FPGA is presented in Appendix A.3. This firmware controls all hardware on the FPGA board and allows for in-firmware PCI communications for measurement customizations and data transfer.

A.1 Principles of FPGA Data Processing

An FPGA allows highly parallel processing and is thus perfectly suited for fast and real-time digital signal analysis. The FPGA itself is a re-configurable piece of electronic hardware, that mainly consists of programmable interconnect matrices, lookup tables, and, in our case, memory cells and dedicated multipliers. For a detailed description of these components I refer to Yalamanchili (2001). One can configure an FPGA such that it implements a pre-designed digital circuit to perform the desired signal processing and data analysis task. The digital circuit is designed using the basic logic gates (AND, OR, NOT, . . .), packages of these (counters, comparators, multiplexers, adders, multipliers, accumulators, . . .), and memory cells of the FPGA. Once the digital circuit is designed it must be synthesized and stored in a file. By copying the file to the FPGA all needed components and their interconnections are configured accordingly to this *firmware*-file, and the designed signal processing and analysis continuously runs on the FPGA.

Most parts of our firmware implement a synchronous digital circuit, i.e. the circuit is divided into sub-circuits where in- and outputs are updated synchronously to a clock with period $t_\mathrm{s} = 10\,\mathrm{ns}$. The operation performed by each sub-circuit completes within one clock period and repeats indefinitely for new inputs in each clock cycle. Thus, we can implement a arithmetic pipeline with signal processing and analysis operations. The arithmetic pipeline is divided into multiple (k) stages that complete within a clock period, as sketched in Figure A.1. Each digitized voltage $V[t]$ from the ADC, termed sample point, passes consecutively all stages of the pipeline. An ADC sampling point influences the output of the arithmetic pipeline after a short and *fixed* time $k \times t_\mathrm{s}$, enabling real-time reactions based on the analysis. As each ADC sampling point passes through every stage, the outcome of the pipeline is based on the full time record of the ADCs, which is in contrast to many other circuit QED experiments where only averages over multiple realizations of an experiment are analyzed. The analysis of the full time record extends the analysis possibilities enormously, e.g. to measurements of power or correlation

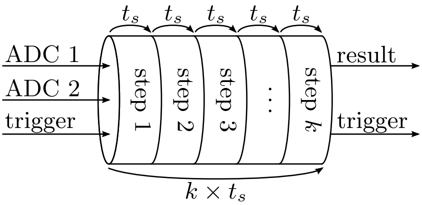

Figure A.1: Arithmetic pipeline: digital signal processing is divided into k stages that complete within a single clock cycle $t_\mathrm{s} = 10\,\mathrm{ns}$ of the FPGA. Each digitized voltage $V[t]$ from the ADCs is processed by the identical set of operational stages. The analysis of the single shot is finished at a fixed time delay, namely $k \times t_\mathrm{s}$, after the last ADC sample point has entered the FPGA.

functions. Note that the transfer of the full time record to the host computer not including the analysis itself is already very time costly and the data transfer and analysis would cause varying time delays, i.e. the analysis would not be real-time any more. In contrast, using the FPGA we are able to sample and analyze in real-time a TB of digitized voltages per hour into files of some hundred KB.

A.2 FPGA Board Hardware

Figure A.2 shows a photograph of the FPGA board used for the experiments of this thesis. The FPGA board consists of three FPGAs (*user FPGA*, *clock FPGA*, *PCI FPGA*), an analog interface (two ADCs, two DACs, reference clock input), a memory component, and a triggering/synchronization module.

User FPGA: The *user FPGA*, a XC4VSX35 (Xilinx, 2010), is the core of our quantum signal analyzer where all digital signal processing and analysis takes place. The *user FPGA* comprises amongst others 3840 configurable logic blocks as the main resource for implementing sequential and combinatorial logic, 192 XtremeDSP slices each with

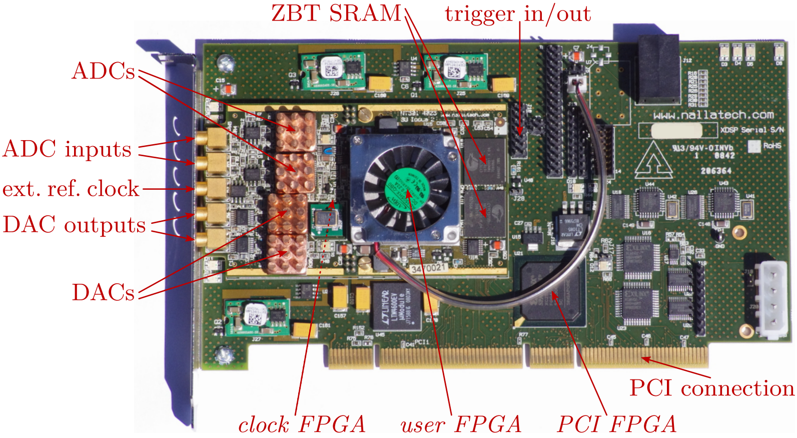

Figure A.2: Photograph of the FPGA board used in this thesis with main hardware elements labeled: *user FPGA* with attached fan, two ADCs, two DACs, external reference clock input (ext. ref. clock), trigger in/out, *clock FPGA* (located at the backside of the module), 2×2 MiB RAM, *PCI FPGA*, PCI connection.

a dedicated 18×18 bit multiplier, and 192 dual-port 18 Kibit[1] RAM blocks.

Clock FPGA: Most parts on the *user FPGA* and nearly all other components used on the board are synchronized to a $f_\mathrm{s} = 100\,\mathrm{MHz}$ clock. As ADCs, DACs and triggers need to be phase-locked to the microwave equipment of the experiment, we derive a clock from an external frequency standard, compare Section 2.6.4. The *clock FPGA* receives a sinusoidal 10 MHz or 50 MHz signal through the external reference clock input. Subsequently, the *clock FPGA* converts the reference into a 100 MHz sampling clock, which is distributed to the ADCs and DACs and to the *user FPGA* having a clock period of $t_\mathrm{s} = 10\,\mathrm{ns}$. The clock is distributed to the external RAM so that the whole board with the exception of the PCI communication runs phase-locked to the frequency standard. A finite crosstalk of the reference clock (and its possible higher harmonics) to the ADC line is present in the used system due to the small distance of the reference clock input to the ADC input. To minimize the crosstalk amplitude we attenuate the reference clock as much as possible. The advantage of the 50 MHz compared to the 10 MHz reference clock is that all frequency components are at the edges of the detection band 0–50 MHz. To prevent damage of the *user FPGA* due to overheating, the 100 MHz clock is switched off once a maximally allowed temperature is exceeded.

---

[1] Binary prefix kibi: $1\,\mathrm{Kibit} = 2^{10}\,\mathrm{bit} = 1024\,\mathrm{bit}$

Analog interface: The analog interface consists of two ADC and two DAC channels. Each ADC digitizes the input voltage with nominal resolution of 14 bit within a full scale (FS) between $-1.1\,\mathrm{V}$ and $1.1\,\mathrm{V}$ at its single-ended $50\,\Omega$ impedance input. While the maximum rate is 105 MHz we use 100 MHz as a convenient frequency. Mostly due to crosstalk of the reference clock signal, the effective number of bits (ENOB) of the ADC is reduced to around 10. As our measurements are dominated by other noise sources our resolution obtained after filtering and averaging is much better than the ENOB. Each DAC channel converts 14 bit numbers into analog voltages with $\mathrm{FS} = \pm 1\,\mathrm{V}$ at its single-ended $50\,\Omega$ impedance output.

Triggering/synchronization module: For triggering and synchronization we connected BNC plugs to four pins of the header (trigger in/out) in Figure A.2. Each of these pins can be configured as a digital one-bit input or output within the FPGA firmware during runtime, and serve as trigger in- and outputs. For example, the detection of a raising edge at a specific trigger input marks the start point of an experimental shot while the raising edge on a second trigger input marks the first pattern in a sequence, compare Section 3.8. A trigger configured as output, for example, can trigger another part of the experiment based on a specific measurement result for real-time feedback (Steffen *et al.*, 2013).

External memory: A zero-bus-turnaround static random-access memory (ZBT SRAM) extends the limited FPGA internal RAM. The latter is a true dual-port RAM that allows two parallel memory accesses in a single clock cycle, e.g. for averaging into the RAM with a net rate of one point per clock period. The ZBT SRAM allows only a single memory access per clock cycle, but has no overhead time when switching between a read and a write access. This is a technical advantage compared to current computer DDR SDRAM that needs multiple clock cycles to switch from reading mode to writing mode and vice versa. The present two banks of ZBT SRAM can be addressed individually and in parallel. They consist of 2^{19} memory cells each with a depth of 32 bit which are also clocked by the phase-locked 100 MHz clock. Using the ZBT SRAM we get in each bank a net averaging rate of one 32 bit word per two clock cycles. We use the ZBT SRAM not only for averaging but also to store the measurement results before the data are transfered to the host computer.

PCI FPGA: The hardware responsible for PCI communication is the only part on the FPGA board that runs at a clock rate of 40 MHz different from all other clock rates. The interface between *user FPGA* and PCI port of the host computer is established by a *PCI FPGA*. This FPGA has a fixed firmware loaded during power-on. It allows to load firmwares onto the *user FPGA* and the *clock FPGA* and is able to read (write) words of 32 bit from (to) the *user FPGA*, as schematically shown in Figure A.3. The transition between the 40 MHz (purple) and 100 MHz (green) clock is realized on the *user FPGA* with first-in first-out (FIFO) buffers and logic.

A.3 FPGA Communications

One critical component for the successful use of the FPGA board as a standard measurement device is a working communication channel, to read out the external ZBT SRAM, for example. Hence, each FPGA measurement firmware requires logic to set-up communication over PCI with the host computer, so that measurements can be controlled and measurement data can be transferred, see Figure A.3.

For this purpose several registers located on the *user FPGA* (each 32 bit wide) have been implemented which can be read and set by both the host computer over the PCI bus and the *user FPGA*. These registers allow to parameterize the digital signal processing, parameterize the measurement applications, start and stop the measurements,

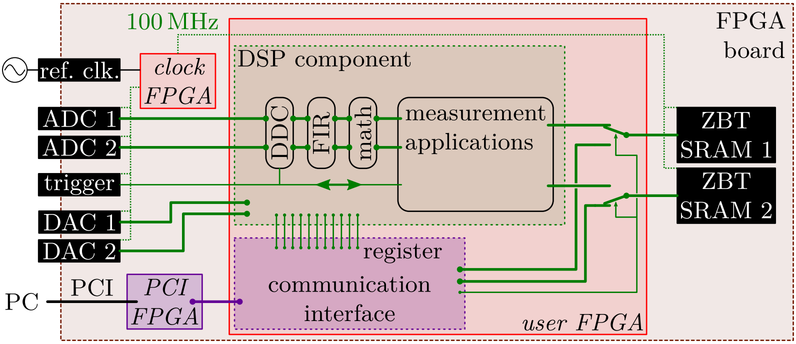
100 MHz
FPGA board
ref. clk.
clock FPGA
DSP component
ADC 1
ADC 2
trigger
DAC 1
DAC 2
DDC
FIR
math
measurement applications
ZBT SRAM 1
ZBT SRAM 2
register
communication interface
PC
PCI
PCI FPGA
user FPGA

Figure A.3: Schematic FPGA firmware for communication and hardware connections to the main components of the FPGA board, compare Figure A.2. Digital signal processing and analysis, as discussed in Chapter 3, is performed within the DSP component.

and retrieve status information of running applications.

The external RAM is used to transfer the measurement data from the FPGA to the host computer. Here, it is important that both *user FPGA* and host computer have access to the external RAM. Two bits of one of the registers above are used to switch the RAM control between the DSP component and the PCI communication interface, as shown in Figure A.3. Parallel to the start of a measurement we connect the RAM to the DSP component. All applications write their status (running/finished) into a status register that we monitor within the measurement software. When the measurement is finished we switch the RAM back to the PCI communication interface and use dedicated register to transfer the desired content of the RAM over the PCI bus to the host computer. A next measurement can immediately be started afterwards.

To control the FPGA from our measurement software, I implemented a C-library that sets up the communication to the FPGA board from the host computer. Most programming or scripting languages support library function calls, such as LabVIEW or Python.

Thus, from within our measurement software we are able to program the *user* and *clock FPGA*, to read and write all registers, and to read and write the ZBT SRAM on the FPGA board. Additionally, we are able to read the critical *user FPGA* temperature and set its maximally allowed temperature. When this temperature is exceeded, the *user FPGA* is automatically stopped to prevent permanent damage of the device.

B

Reconstruction of Two-Time Correlations

In the measurements presented in this thesis, we are interested in the quantum-mechanical properties of electromagnetic microwave radiation, in particular their correlation functions. Even though we compute the correlation functions based solely on calculations involving complex numbers, as shown in Section 3.9, we are able to extract quantum-mechanical correlations. Depending on the type of correlation function, we are considering we use different strategies to measure them. In this appendix, I present an overview of these strategies and discuss their advantages and disadvantages.

During linear detection, noise is added to the microwave radiation of interest due to amplifying vacuum and thermal fluctuations in the amplification process; compare Sections 3.1 to 3.4. The measurement of correlation functions includes that noise. To reconstruct the correlation function $G[\tau]$ of the microwave radiation of interest, reference measurements have to be taken into account; compare Section 3.9. Here, I derive the correlation terms that need to be measured to correct for the noise in different order correlation functions. I use the operator formulation for the measured complex amplitude S, as introduced in Section 3.4.

In the following, I distinguish between the measured correlation function $\Gamma[\tau]$ and the noise reference correlation function $H[\tau]$ that is measured when the detection chain input is left idle, ideally in the vacuum state. The quantum-mechanical definitions of the first- and second-order auto-correlation are

$$\begin{aligned} G^{(1)}[\tau] &= \langle \hat{a} \star \hat{a} \rangle [\tau] \\ G^{(2)}[\tau] &= \langle : \hat{a}^\dagger \hat{a} \star \hat{a}^\dagger \hat{a} : \rangle [\tau] \,, \end{aligned}$$

respectively. Correlation ($\star$) of operators is equally defined as in Equation (3.3), however, we replace complex conjugation (*) by Hermitian conjugation (†), and order normally ($\langle : : \rangle$). Note that this definition, analogous to the mathematical correlation given in Equation (3.3), implies the Hermitian conjugation of the first correlation argument, which is thus hidden in the $\star$-operator. For all correlation functions, and especially for cross-correlations, subscripts indicate the quantities that are correlated. For example,

$$G^{(2)}_{ab}[\tau] = \langle \hat{a}^\dagger \hat{a} \star \hat{b}^\dagger \hat{b} \rangle [\tau]$$

is the second-order cross-correlation of radiation mode $\hat{a}$ with $\hat{b}$.

B.1 Power Spectral Density

The measurement of the power spectral density was already discussed in Section 3.9. The reconstruction approach of correlation functions $G[\tau]$ is illustrated by the following measurement of the first-order auto-correlation function, which is the power spectral density in the time domain. The evaluation of $\mathit{\Gamma}^{(1)} = \langle S \star S \rangle$ shows that

$$\begin{aligned} \mathit{\Gamma}^{(1)} = \langle S \star S \rangle &= g \, \langle (\hat{a} + \hat{h}^\dagger) \star (\hat{a} + \hat{h}^\dagger) \rangle \\ &= g \, \langle \hat{a} \star \hat{a} + \hat{h}^\dagger \star \hat{h}^\dagger + \hat{a} \star \hat{h}^\dagger + \hat{h}^\dagger \star \hat{a} \rangle \\ &= g \left(\langle \hat{a} \star \hat{a} \rangle + \langle \hat{h}^\dagger \star \hat{h}^\dagger \rangle \right) , \end{aligned} \tag{B.1}$$

where g is the gain factor of the linear detection chain. Note that we use here and also in the following, that all terms with an odd number of noise operators can be removed as the noise is assumed to be symmetrically distributed around zero (Agarwal and Chaturvedi, 1994; da Silva *et al.*, 2010). Subtracting the noise reference measurement $H^{(1)} = g\,\langle \hat{h}^\dagger \star \hat{h}^\dagger \rangle$ from Equation (B.1) results in the first-order auto-correlation function

$$gG^{(1)}[\tau] = \mathit{\Gamma}^{(1)}[\tau] - H^{(1)}[\tau]$$

of $\hat{a}$. For $\tau = 0$, $G^{(1)}[0]$ provides the integrated intensity $\langle \hat{a}^\dagger \hat{a} \rangle$ whereas $H^{(1)}[0]$ the integrated intensity of the noise fluctuations $g\,\langle \hat{h}\hat{h}^\dagger \rangle$.

B.2 Cross-Power Spectral Density

The cross-power spectral density is obtained by measuring the first-order cross-correlation function. This measurement has the advantage that uncorrelated noise averages to zero. When measuring a single field $\hat{a}'$ using two separate and independent detection chains, we obtain the first-order auto-correlation $G^{(1)}_{a'a'}[\tau]$ of that field $\hat{a}'$. Consider, for example, an HBT-like setup with a beam splitter (Section 2.5, Figure 2.8), where the second beam splitter input $\hat{b}'$ is in the vacuum state. The two detection chains add uncorrelated noise $\hat{h}_a^\dagger$ and $\hat{h}_b^\dagger$ to the complex amplitudes S_a and S_b. Thus, the correlation of the measured classical complex amplitudes S_a and S_b yields:

$$\begin{aligned}\mathit{\Gamma}^{(1)}_{ab} &= \langle S_a \star S_b \rangle \\ &= \sqrt{g_a g_b}\, e^{i\varphi}\, \langle \hat{a} \star \hat{b} + \hat{h}_a^\dagger \star \hat{h}_b^\dagger + \hat{a} \star \hat{h}_b^\dagger + \hat{h}_a^\dagger \star \hat{b} \rangle \\ &= \sqrt{g_a g_b}\, e^{i\varphi} \left(\langle \hat{a} \star \hat{b} \rangle + \langle \hat{h}_a^\dagger \star \hat{h}_b^\dagger \rangle \right) ,\end{aligned}$$

where φ denotes a possible path length difference of the two detection chains. The correlations of mode $\hat{a}'$ are included in $\langle \hat{a} \star \hat{b} \rangle = \frac{i}{2} \langle \hat{a}' \star \hat{a}' + i\hat{a}' \star \hat{b}' + \hat{b}' \star i\hat{a}' - \hat{b}' \star \hat{b}' \rangle = \frac{i}{2} \langle \hat{a}' \star \hat{a}' \rangle$ for mode $\hat{b}'$ ideally in the vacuum state. Parasitic noise correlations $H^{(1)}_{ab}[\tau] = \sqrt{g_a g_b}\, e^{i\varphi}\, \langle \hat{h}_a^\dagger \star \hat{h}_b^\dagger \rangle [\tau]$ are usually small compared to the correlations of $\hat{a}'$. We get

$$\tfrac{\sqrt{g_a g_b}}{2}\, G^{(1)}_{a'a'}[\tau] = -ie^{-i\varphi}\, \mathit{\Gamma}^{(1)}_{ab}[\tau] \, .$$

Small parasitic noise correlations $H_{ab}^{(1)}[\tau]$ can be subtracted as discussed in Appendix B.1. In contrast to the auto-correlation, a path length difference of the two detection chains rotates the correlation function $G_{a'a'}^{(1)}[\tau]$ by the phase factor $e^{i\varphi}$. Since the phase φ is measured easily, this rotation is usually no drawback. The power spectral density is the Fourier transform of $G_{a'a'}^{(1)}[\tau]$ and is demonstrated in Section 4.2 for characterization of a continuous single-photon source (Lang *et al.*, 2011).

B.3 Second-Order Auto-Correlation

The second-order correlation function using only a single detection chain (Steudle *et al.*, 2012) is measured by the auto-correlation of the intensities $\varGamma^{(2)} = \langle |S|^2 \star |S|^2 \rangle$ and is demonstrated in Section 6.2 (Lang *et al.*, 2013b). As in Appendix B.1, we evaluate $\varGamma^{(2)}[\tau]$ and remove all terms with an odd number of noise operators as their expectation values are zero (Agarwal and Chaturvedi, 1994; da Silva *et al.*, 2010; Menzel *et al.*, 2010):

$$
\begin{aligned}
\varGamma^{(2)} &= \langle |S|^2 \star |S|^2 \rangle \\
&= g^2 \big(\langle : \hat{a}^\dagger \hat{a} \star \hat{a}^\dagger \hat{a} : \rangle + \langle \text{“}\, \hat{h}\hat{h}^\dagger \star \hat{h}\hat{h}^\dagger \,\text{”} \rangle + 2 \langle \hat{a}^\dagger \hat{a} \rangle \langle \hat{h}\hat{h}^\dagger \rangle \\
&\qquad + \langle : \hat{a}^\dagger \star \hat{a}^\dagger : \rangle \langle \hat{h}^\dagger \star \hat{h}^\dagger \rangle + \langle \hat{a} \star \hat{a} \rangle \langle \text{“}\, \hat{h} \star \hat{h} \,\text{”} \rangle \\
&\qquad + \langle \hat{a}^\dagger \star \hat{a} \rangle \langle \hat{h}^\dagger \star \hat{h} \rangle + \langle \hat{a} \star \hat{a}^\dagger \rangle \langle \hat{h} \star \hat{h}^\dagger \rangle \big) ,
\end{aligned}
$$

where the correlations of field and noise are separated, and the noise operators are ordered anti-normally ($\langle \text{“ ”} \rangle$)[1]. Additionally, we remove the last two terms as the expectation values $\langle \hat{h}^\dagger \star \hat{h} \rangle$ and $\langle \hat{h} \star \hat{h}^\dagger \rangle$ are zero for all τ. Thus, the second-order auto-correlation of $\hat{a}$ is obtained as

$$
\begin{aligned}
g^2 G^{(2)}[\tau] = \varGamma^{(2)}[\tau] - H^{(2)}[\tau] - 2g G^{(1)}[0] H^{(1)}[0] \\
- g G^{(1)}[-\tau] H^{(1)}[\tau] - g G^{(1)}[\tau] H^{(1)}[-\tau] \,.
\end{aligned}
$$

---

[1] Definition from Mandel and Wolf (1995).

To evaluate this expression, we measure the four correlation functions $\mathit{\Gamma}^{(2)}[\tau]$, $H^{(2)}[\tau]$, $\mathit{\Gamma}^{(1)}[\tau]$ and $H^{(1)}[\tau]$. To diminish heterogeneous impact due to long term drifts, all four correlation functions are measured and averaged successively in rotation as explained in Sections 3.8 and 3.9.

Note that the single-shot second-order correlation functions have a signal to noise ratio (snr) squared compared to the signal to noise ratio (snr) of the first-order correlation functions (da Silva *et al.*, 2010). Since the standard deviation of the noise in the measurement diminishes only by $1/\sqrt{R}$ with the number of repetitions R, $\mathit{\Gamma}^{(2)}[\tau]$ and $H^{(2)}[\tau]$ have to be averaged exponentially longer than any first-order correlation function to obtain equivalent accuracy. Even though the first-order terms appear as products its uncertainty scales only linearly with the uncertainty of the two factors, as shown with error propagation.

B.4 Second-Order Cross-Correlation

Evaluating the expression $\mathit{\Gamma}_{ab}^{(2)} = \langle |S_a|^2 \star |S_b|^2 \rangle$ allows us to investigate second-order cross-correlations between $\hat{a}$ and $\hat{b}$. A well-known example is HOM two-photon coalescence (Hong, Ou, and Mandel, 1987), which we have demonstrated in Section 6.2 (Lang *et al.*, 2013b). The evaluation of $\mathit{\Gamma}_{ab}^{(2)}$

$$\begin{aligned}\mathit{\Gamma}_{ab}^{(2)} &= \langle |S_a|^2 \star |S_b|^2 \rangle \\ &= g_a g_b \big(\langle \hat{a}^\dagger \hat{a} \star \hat{b}^\dagger \hat{b} \rangle + \langle \hat{h}_a \hat{h}_a^\dagger \star \hat{h}_b \hat{h}_b^\dagger \rangle + \langle \hat{a}^\dagger \hat{a} \rangle \langle \hat{h}_b \hat{h}_b^\dagger \rangle + \langle \hat{b}^\dagger \hat{b} \rangle \langle \hat{h}_a \hat{h}_a^\dagger \rangle \\ &\qquad + \langle \hat{a}^\dagger \star \hat{b}^\dagger \rangle \langle \hat{h}_a^\dagger \star \hat{h}_b^\dagger \rangle + \langle \hat{a} \star \hat{b} \rangle \langle \hat{h}_a \star \hat{h}_b \rangle \\ &\qquad + \langle \hat{a}^\dagger \star \hat{b} \rangle \langle \hat{h}_a^\dagger \star \hat{h}_b \rangle + \langle \hat{a} \star \hat{b}^\dagger \rangle \langle \hat{h}_a \star \hat{h}_b^\dagger \rangle \big)\end{aligned} \tag{B.2}$$

shows that $G_{ab}^{(2)}$ is obtained by

$$\begin{aligned} g_a g_b G_{ab}^{(2)}[\tau] = \mathit{\Gamma}_{ab}^{(2)}[\tau] - H_{ab}^{(2)}[\tau] \\ - g_a G_{aa}^{(1)}[0] H_{bb}^{(1)}[0] - g_b G_{bb}^{(1)}[0] H_{aa}^{(1)}[0] \,. \end{aligned}$$

In contrast to second-order auto-correlation function measurements (Appendix B.3), we only have to subtract a constant offset (second line) composed of first-order correlations. This is because the cross-correlations $H^{(1)}_{ab}[\tau]$ of the noise [in terms five and six of Equation (B.2)] in the two detection chains are in our setup negligible as expected. If needed $H^{(1)}_{ab}[\tau]$ could also be measured and corrected for. Similarly in term seven and eight of Equation (B.2), the noise is assumed to be symmetrically distributed around zero, with the consequence that these two terms are equal to zero.

The same advantage can be exploited when a single field $\hat{a}'$ is measured by two separate detection chains in an HBT-like setup, as discussed in Appendix B.2. As no correlated radiation enters through the second beam splitter input $\hat{b}'$, which is in the vacuum state, the second-order correlation function of $\hat{a}'$ is

$$G^{(2)}_{a'a'}[\tau] = 4\, G^{(2)}_{ab}[\tau]\,.$$

We have demonstrated such measurements in circuit QED for a pulsed (Bozyigit *et al.*, 2011b) and a continuous single-photon source discussed in Section 4.3 (Lang *et al.*, 2011).

B.5 Cross-Power Auto-Correlation

The detection of the two complex amplitudes $S_a[t]$ and $S_b[t]$ allow also to measure the second-order *cross-power* (quasi-)auto-correlation function $G^{(2Y)}_{ab}[\tau] = \langle (S^*_a S_b) \star (S_a S^*_b)\rangle[\tau]$. This is not a real auto-correlation since the second argument is not equal but the complex conjugate of the first argument. In the case of HBT-like setups, such a setting serves as a measurement of the second-order correlation function $G^{(2)}_{a'a'}[\tau]$ that is not offset due to the noise power, which is in contrast to the $\Gamma^{(2)}_{ab}[\tau]$ case (da Silva *et al.*, 2010). The evaluation

$$\begin{aligned}\Gamma^{(2Y)}_{ab} = \big(&\langle \hat{a}^\dagger \hat{b} \star \hat{a}\hat{b}^\dagger\rangle + \langle \hat{h}_a \hat{h}^\dagger_b \star \hat{h}^\dagger_a \hat{h}_b\rangle + \langle \hat{a}^\dagger \hat{b}\rangle \langle \hat{h}^\dagger_a \hat{h}_b\rangle + \langle \hat{a}\hat{b}^\dagger\rangle \langle \hat{h}_a \hat{h}^\dagger_b\rangle \\ &+ \langle \hat{a}^\dagger \star \hat{a}\rangle \langle \hat{h}^\dagger_b \star \hat{h}_b\rangle + \langle \hat{b} \star \hat{b}^\dagger\rangle \langle \hat{h}_a \star \hat{h}^\dagger_a\rangle \\ &\quad + \langle \hat{a}^\dagger \star \hat{b}^\dagger\rangle \langle \hat{h}^\dagger_b \star \hat{h}^\dagger_a\rangle + \langle \hat{b} \star \hat{a}\rangle \langle \hat{h}_a \star \hat{h}_b\rangle\big) g_a g_b e^{-2i\varphi} \qquad \text{(B.3)}\end{aligned}$$

shows, assuming that terms three to eight are zero as discussed in Appendix B.4, that

$$\tfrac{g_a g_b}{4}\, G^{(2)}_{a'a'}[\tau] = e^{2i\varphi}\big(\varGamma^{(2Y)}_{ab}[\tau] - H^{(2Y)}_{ab}[\tau]\big)\;,$$

where the second-order correlations of the noise fluctuations $H^{(2Y)}_{ab}[\tau]$ are expected to be small for all τ. Similar to the cross-power spectral density (Appendix B.2), $G^{(2)}_{a'a'}$ is rotated by a phase 2φ. Again, small finite cross-correlations of the noise, which usually are negligible in our setup, can be measured and be corrected for. This was done for the second-order correlation function measurements in Section 5.3 (Bozyigit *et al.*, 2011a).

C

Theoretical Expressions

To validate the experimental measurements presented in this thesis, we compared them with the theoretically expected values, plotted as a line underneath the measurement data. The theory is based on analytical calculations and also master equation simulations. This appendix shows the equations used in the main graphics, such as Figures 4.2, 4.3, 5.4, 6.4 and 6.5, to illustrate first- and second-order correlations. Derivations of these equations are sketched giving appropriate references for further reading.

C.1 Photon Blockade

C.1.1 Resonance Fluorescence Spectrum

To cover the physics of the photon blockade system, it is the most simple, but also sufficient, to consider a single driven two-level system. This approximation to the two lowest energy levels of the anharmonic Jaynes-Cummings ladder of resonantly coupled qubit and resonator can be done because the drive is slow enough so that the system is not excited significantly into other levels; compare Section 2.3. The physics of resonance fluorescence from a driven two-level system is well understood and often discussed in quantum optics lectures as well as books (Mollow, 1969; Carmichael and Walls, 1976; Carmichael, 2002; Scully and Zubairy, 1997). To calculate the expression of the resonance fluorescence spectrum in Figure 4.2(b), I followed the steps presented in Chapter 2 of Carmichael (2002), including dephasing and without approximating the strength of the drive that is typically considered to be strong or weak compared to the relaxation rate of the two-level system. The steps are compatible to those discussed by Woolley *et al.* (2013) as well, where more detailed explanations can be found in a more compact manner than in Carmichael (2002).

The Hamiltonian of the driven two-level system shall be

$$\hat{H}^{\mathrm{d}}_{\mathrm{TLS}} = \tfrac{1}{2}\tilde{\omega}_{\mathrm{a}}\hat{\sigma}_z - \Omega_{\mathrm{R}}(\hat{\sigma}_+ + \hat{\sigma}_-)\,,$$

where the transition frequency $\tilde{\omega}_{\mathrm{a}} = \omega_{\mathrm{d}}$ is equal to the drive frequency, and the drive strength Ω_{R} is chosen to be real valued, without loss of generality. The first term represents the two-level system Hamiltonian, and the second term the Hamiltonian for the drive.

The coupling to the environment is described by two parameters for the decay rate $\tilde{\gamma}$ and the dephasing rate $\tilde{\gamma}_\varphi$ of the two-level system. Hereby, we expect that $\tilde{\gamma}$ is dominated by photon decay through the output of the cavity. The time evolution of the two-level system density operator ϱ is then given by the master equation in Lindblad form

$$\tfrac{\mathrm{d}}{\mathrm{d}t}\varrho = -i\big[\hat{H}^{\mathrm{d}}_{\mathrm{TLS}}, \varrho\big] + \tfrac{1}{2}\tilde{\gamma}(2\hat{\sigma}_-\varrho\hat{\sigma}_+ + \hat{\sigma}_+\hat{\sigma}_-\varrho - \varrho\hat{\sigma}_+\hat{\sigma}_-) + \tfrac{1}{2}\tilde{\gamma}_\varphi(\hat{\sigma}_z\varrho\hat{\sigma}_z - \varrho)\,.$$

Using the master equation we can write down the so-called optical Bloch-equations through the expectation value of the time evolution

$$\begin{aligned}
\tfrac{\mathrm{d}}{\mathrm{d}t}\left\langle\hat{\sigma}_-\right\rangle &= -\tilde{\gamma}_2\left\langle\hat{\sigma}_-\right\rangle && -\tfrac{1}{2}i\Omega_{\mathrm{R}}\left\langle\hat{\sigma}_z\right\rangle\\
\tfrac{\mathrm{d}}{\mathrm{d}t}\left\langle\hat{\sigma}_+\right\rangle &= && -\tilde{\gamma}_2\left\langle\hat{\sigma}_+\right\rangle + \tfrac{1}{2}i\Omega_{\mathrm{R}}\left\langle\hat{\sigma}_z\right\rangle\\
\tfrac{\mathrm{d}}{\mathrm{d}t}\left\langle\hat{\sigma}_z\right\rangle &= -i\Omega_{\mathrm{R}}\left\langle\hat{\sigma}_-\right\rangle + i\Omega_{\mathrm{R}}\left\langle\hat{\sigma}_+\right\rangle && -\tilde{\gamma}\left\langle\hat{\sigma}_z\right\rangle - \tilde{\gamma}\,,
\end{aligned}$$

where we have introduced the total dephasing rate $\tilde{\gamma}_2 \equiv \frac{1}{2}(\tilde{\gamma} + 2\tilde{\gamma}_\varphi)$. To solve the set of differential equations, the optical Bloch-equations are typically written in matrix form and subsequently diagonalized.

This allows one to find the steady state solutions

$$\langle\hat{\sigma}_{\mp}\rangle_{\mathrm{ss}} = \pm\frac{i\Omega_{\mathrm{R}}\tilde{\gamma}}{2(\Omega_{\mathrm{R}}^2+\tilde{\gamma}\tilde{\gamma}_2)} \quad \text{and} \qquad \langle\hat{\sigma}_z\rangle_{\mathrm{ss}} = -\frac{\tilde{\gamma}\tilde{\gamma}_2}{\Omega_{\mathrm{R}}^2+\tilde{\gamma}\tilde{\gamma}_2}\,,$$

for which $\frac{\mathrm{d}}{\mathrm{d}t}\langle\hat{\sigma}_j\rangle = 0$ for all $j \in \{-,+,z\}$. Based on the steady state solutions an initial condition is found to solve the optical Bloch-equations. The form of the solution allows us to apply the quantum regression formula, with which two-time correlation functions can be evaluated such as the first-order correlation function

$$G^{(1)}(\tau) = \lim_{t\to\infty}\langle\hat{\sigma}_+(t)\,\hat{\sigma}_-(t+\tau)\rangle$$

between the two-level system raising ($\hat{\sigma}_+$) and lowering ($\hat{\sigma}_-$) operator, which expresses the correlations that are discussed throughout Section 4.2 in the frequency domain. Evaluating the expression for $G^{(1)}(\tau)$ it follows

$$G^{(1)}(\tau) = \frac{\Omega_{\mathrm{R}}^2}{4(\tilde{\gamma}\tilde{\gamma}_2+\Omega_{\mathrm{R}}^2)}\left(\frac{\tilde{\gamma}^2}{(\tilde{\gamma}\tilde{\gamma}_2+\Omega_{\mathrm{R}}^2)} + e^{-\tau\tilde{\gamma}_2} + \right.$$
$$\left. + e^{-\tau(\tilde{\gamma}+\tilde{\gamma}_2)/2}\left(\lambda_+ e^{i\tilde{\Omega}\tau} + \lambda_- e^{-i\tilde{\Omega}\tau}\right)\right)\,, \qquad \text{(C.1)}$$

where we have introduced the notation

$$i\tilde{\Omega} \equiv \sqrt{-\Omega_{\mathrm{R}}^2 + \tfrac{1}{4}(\tilde{\gamma}-\tilde{\gamma}_2)^2}$$
$$\lambda_\pm \equiv \frac{(2\Omega_{\mathrm{R}}^2 \mp 2i\tilde{\Omega}\tilde{\gamma} - \tilde{\gamma}^2 + \tilde{\gamma}\tilde{\gamma}_2)(2\tilde{\Omega} \mp i(\tilde{\gamma}-\tilde{\gamma}_2))}{8\tilde{\Omega}(\tilde{\gamma}\tilde{\gamma}_2+\Omega_{\mathrm{R}}^2)}\,.$$

The power spectral density of the field emitted from the two-level system is the Fourier transform of $G^{(1)}(\tau)$:

$$\mathrm{PSD}(\omega) = \int_0^\infty G^{(1)}(\tau)\,e^{i(\omega-\omega_{\mathrm{d}})\tau}\,\mathrm{d}\tau\,.$$

Expanding Equation (C.1), the first summand results in a δ-function for the Rayleigh-scattering peak in $\mathrm{PSD}(\omega)$, and the second summand in the central Lorentzian peak of the Mollow triplet with characteristic width $\tilde{\gamma}_2$. Summand three and four represent left and right side peak in the Mollow triplet structure, and are only Lorentzian peaks for strong driving. The solid lines in Figure 4.2(b) show the resonance fluorescence spectrum PSD(ω) omitting the Rayleigh-scattering peak for a set of drive amplitudes $\varOmega_\mathrm{R}$.

C.1.2 Master Equation Simulation

The simple model of a driven two-level system deviates from the measured data in the predicted strength of the coherently scattered radiation. This is mostly due to the presence of the $|2-\rangle$ state in the Jaynes-Cummings ladder. To correctly capture the amplitude of the Rayleigh-scattered peak, we compare the measured spectrum in Figure 4.2(a) with a master equation simulation, which is subsequently also used in Figure 4.3(a) to validate the measured second-order correlation functions.

For the master equation simulation, the Hamiltonian is extended compared to the one in Appendix C.1.1 to get the Jaynes-Cummings ladder energy level structure. Therefore, we use the Jaynes-Cummings Hamiltonian $\hat{H}_\mathrm{JC}$ (2.1) and add a coherent drive to the resonator

$$\hat{H}_\mathrm{JC}^\mathrm{d} = \hat{H}_\mathrm{JC} - \varOmega_\mathrm{R}(\hat{A}^\dagger + \hat{A}) \,,$$

where we set in the known system parameters. As in Appendix C.1.1 we set up the master equation in Lindblad form using $\hat{H}_\mathrm{JC}^\mathrm{d}$ and the coupling to the environment using the decay rate γ and dephasing rate γ_φ of the qubit, and the decay rate κ of resonator excitations. Subsequently, the master equation is numerically solved, where we restrict the density matrix ϱ from 0 to 4 photons. The solution for ϱ is then used to extract the theoretically expected PSD(ω) shown in Figure 4.2(a), and the unfiltered second-order correlation functions shown in Figure 4.3(a) by the black line.

The gray lines in Figure 4.3(a) take into account limited detection bandwidth, i.e. filtering of the measurement signal, for the expected second-order correlation functions. A strictly correct way of including filtering, would be to calculate the expected unfiltered 4-time-point second-order correlation function, apply the global 4-time-point filter function, and integrate out all times but the time delay τ (da Silva *et al.*, 2010). In this case, we would need too much computing power since two more dimensions would be introduced into the numerical calculations. Instead, we approximate the effect of filtering for the case in which the measured signal is strongly dominated by white noise added in the detection chain. For white noise $h[t]$ with constant power spectral density $|\bar{H}|^2$, the effective bandwidth of a filtered second-order correlation function is calculated straight forwardly. To do so, we calculate the correlation functions in the frequency domain [compare Equation (3.4)] and filter by convolution [compare Equation (3.1)] as we do it in our quantum signal analyzer; compare Section 3.9. Using the convolution theorem $\mathcal{F}(w \star k)[\nu] = \mathcal{F}(w)[\nu]\ \mathcal{F}(k)[\nu]$ we can rewrite each of the inner Fourier transforms in Equation (3.4) exemplary for the waveform calculating the power $w[t] = S[t]\, S^*[t]$ of the filtered white noise $St = (h \star k)[t]$:

$$\mathcal{F}(w) = \mathcal{F}(S\, S^*) = \mathcal{F}\big(\mathcal{F}^{\text{-}1}(K\, \mathcal{F}(h)) \cdot \mathcal{F}^{\text{-}1^*}(K\, \mathcal{F}(h))\big)\,, \qquad \text{(C.2)}$$

where the filter kernel $k[t']$ is padded with zeros to the same length as $S[t]$ and $K[\nu] = \mathcal{F}(k)[\nu]$. For white noise, each frequency bin of $\mathcal{F}(h)[\nu]$ is on average $|\bar{H}|$ and has a random phase that is common in both factors of Equation (C.2). Therefore, we factor out the constant $\bar{H}$ and approximate $\mathcal{F}(w)[\nu]$ as

$$\mathcal{F}(w) \approx \mathcal{F}\big(\bar{H}\, \bar{H}^*\ \mathcal{F}^{\text{-}1}(K)\ \mathcal{F}^{\text{-}1^*}(K)\big) = |\bar{H}|^2\ \mathcal{F}(|k|^2)\,.$$

Comparing this with the convolution theorem, we see that the calculated power of white noise is effectively filtered by a kernel $|k[t']|^2$. Also a numerical simulation of noise with the filter that was used in the experiments showed similar results. In Figure 4.3(a), we convoluted the unfiltered second-order correlation functions (black lines) with the squared filter kernel $|k[t']|^2$ twice, once for each Fourier transform in Equation (3.4), to approximate the limited detection bandwidth (gray lines). Please keep in mind that this filtering of the second-order correlation function is only an approximation in the limit of very small signal to noise ratio.

C.2 Pulsed Photons and their Interference

In Chapters 5 and 6 we presented the generation and interference of triggered single-photons. We measured their temporal profiles, and first- and second-order correlation functions. The theoretical basis for these measurements using linear detection is published by da Silva *et al.* (2010) and Woolley *et al.* (2013), and sketched here. Since all following calculations are included in the second-order correlation function for the two-photon HOM interference, the equations include indices A and B, naming the two source resonators, and the photon generation delay time $\delta\tau$. For a single source only, as in Chapter 5, please consider only source A and $\delta\tau = 0$. The calculations are presented using all parameters necessary for Figures 6.4 and 6.5, and as they are developed by Woolley *et al.* (2013), where more profound details can be found.

C.2.1 Temporal Mode Function

In order to trigger the emission of a single-photon, a qubit is used to bring the resonator into its first excited state, as described in Section 5.1. The time needed to excite the resonator is here considered to be instantaneous, since the excitation process cannot be resolved due to the limited detection bandwidth. The excitation then decays exponentially out of the resonator at rate $\kappa_{A/B}$. For the temporal mode function, proportional to the field amplitude, we get an exponential decay at rate $\kappa/2$

$$\xi_{A/B,n}(t) = \begin{cases} \sqrt{\kappa_{A/B}}\, e^{-(t-n\,t_\mathrm{r}\pm\delta\tau/2)\,\kappa_{A/B}/2} & \text{if } n\,t_\mathrm{r}\mp\delta\tau/2 \le t\,, \\ 0 & \text{else,} \end{cases}$$

in the rotating frame of the photon frequency $\omega_\mathrm{r} = \omega_\mathrm{d}$ after the photon release time $n\,t_\mathrm{r} \mp \delta\tau/2$. Here, n is the pulse number in the single-photon pulse train generated with a repetition period of t_r. We refer to Woolley *et al.* (2013) for the case of photons with frequencies ω_r other than the detection frequency ω_d.

To incorporate the limited detection bandwidth of the linear detection chain, we apply an FIR filter to $\xi_{A/B,n}(t)$. We use a simple square window FIR filter, since this continuous-time filter provides comparable properties as the discrete-time one used in the experiment. Additionally, all further calculations can be solved analytically. Similarly as the discrete-time FIR filter kernel in Equation (3.1), the kernel is here

$$k(t') = \begin{cases} 1/T & \text{if } 0 \leq t' < T\,, \\ 0 & \text{else,} \end{cases}$$

with the window length T. The continuous-time convolution of the temporal mode function $\xi_{A/B,n}(t)$ with the kernel $k(t')$ results in the filtered temporal mode function

$$\zeta_{A/B,n}(t) = \int_{-\infty}^{\infty} \xi_{A/B,n}(t - t')\, k(t')\, \mathrm{d}t' \,.$$

The solid line in Figure 5.2(b) shows a filtered single-photon pulse $\zeta(t)$ with the decay rate of $\kappa/2$, whereas the rise time of the pulse is limited by the FIR filter.

Having the filtered mode function, we can easily calculate the temporal profile of a power measurement

$$U_{A/B,n}(t) = \zeta^*_{A/B,n}(t)\, \zeta_{A/B,n}(t)$$

resulting in the expected decay rate κ of the cavity photon number, for which an example is shown in Figure 5.2(e). We also introduce the product of mode functions

$$V_{A/B}(t,\tau) = \zeta^*_{A/B,0}(t)\, \zeta_{A/B,0}(t+\tau)$$

evaluated at different times in order to write compact expressions for the expected second-order correlation function measurements, presented in the next section.

C.2.2 Second-Order Correlations and Interference

For the calculation of second-order correlation functions, we need to evaluate a sum, where each summand is the product of four temporal mode functions, two at time t and two at $t+\tau$. As shown below, the detection time t is subsequently integrated out and summed over the whole pulse train of N photons to get the expected $G^{(2)}(\tau)$ (Woolley *et al.*, 2013).

Assuming essentially no overlap of the temporal mode function between two subsequent photons of a source ($t_\mathrm{r} \gg 1/\kappa$) and evaluating the expected single-photon input states, we can exploit symmetries and further simplify the complete expression given in Equation (27) of Woolley *et al.* (2013). When operating only a single single-photon source as in Figures 5.4 and 6.4(a,b), the second-order correlation function $G^{(2)}_{A/B}(\tau)$ of source A and B respectively is expected to be

$$G^{(2)}_{A/B}(\tau) = \frac{1}{4} \sum_{n=-N/2}^{N/2} \big(1-\delta(n)\big)\Big(\int V_{A/B}(t,\tau)\, V^*_{A/B}(t,\tau)\, \mathrm{d}t \\ + \int U_{A/B,0}(t)\, U_{A/B,n}(t+\tau)\, \mathrm{d}t\Big)\,,$$

where $\delta(n)$ is the Kronecker delta being 0 for $n=0$ and 1 otherwise. Note that the only experimental parameter is the photon decay rate κ, measured in independent experiments, and all others are design parameters.

In the expression for the second-order cross- and auto-correlation function including two-photon interference, more terms are added:

$$G^{(2)}_{ab/aa}(\tau) = G^{(2)}_{A}(\tau) + G^{(2)}_{B}(\tau) + \frac{1}{4} \sum_{n=-N/2}^{N/2} \Big(\\ \int U_{A,0}(t)\, U_{B,n}(t+\tau)\, \mathrm{d}t + \int U_{B,0}(t)\, U_{A,n}(t+\tau)\, \mathrm{d}t \\ \pm \int V_{A}(t,\tau)\, V^*_{B}(t,\tau)\, \mathrm{d}t \pm \int V^*_{A}(t,\tau)\, V_{B}(t,\tau)\, \mathrm{d}t\Big)\,. \tag{C.3}$$

The cross-correlation function $G_{ab}^{(2)}(\tau)$ of the beam splitter outputs is shown in Figure 6.4(c-f) for different delay times $\delta\tau$ as tuning parameter for photon distinguishability. The second-order auto-correlation function $G_{aa}^{(2)}(\tau)$ in a single beam splitter output is presented in Figure 6.5.

List of Figures

2.1 Cavity QED system 10
2.2 Circuit QED scheme 13
2.3 Circuit QED sample 17
2.4 Energy level diagram of transmon resonator system . . 23
2.5 Transitions of transmon resonator system 25
2.6 Qubit state dependent resonator shift 28
2.7 Bloch sphere and qubit control 32
2.8 Beam splitter 34
2.9 Experimental setup 40
2.10 Schematic of experimental setup 43

3.1 Effective heterodyne detection chain 51
3.2 PSD illustration of heterodyne detection 57
3.3 FIR filter 59
3.4 Time-dependent ensemble averaging 66
3.5 Circular correlation function 68
3.6 Sketch of histogram bins 72

4.1 Dressed energy level diagram 76
4.2 Mollow Triplet 78
4.3 Second-order correlation function measurements for continuous sources 81

5.1 Qubit state preparation and vacuum Rabi oscillation . 85
5.2 Complex amplitude and cross-power measurements . . 87
5.3 First-order correlation function measurements 91
5.4 Second-order correlation function measurements 92

6.1 Micrograph of HOM device 97
6.2 Schematic of the HOM experiment 98
6.3 Power spectral density of triggered single-photon sources 99
6.4 Second-order cross-correlation function measurements of HOM experiments 100
6.5 Second-order auto-correlation function measurements of HOM experiments 103
6.6 Full quantum state tomography 105

A.1 Arithmetic pipeline 113
A.2 Photograph of the FPGA board 114
A.3 FPGA firmware functional blocks 117

Glossary

∿ microwave source.

⌇ arbitrary waveform channel for voltage pulse.

⎍ arbitrary waveform channel for current pulse.

⊝ battery, d.c. voltage source.

ADC analog-to-digital converter.

DAC digital-to-analog converter.

⏚ ground.

⏜ inductor.

⫲ capacitance.

⊠ Josephson junction, combination of Josephson inductance and intrinsic capacitance.

⊤ floating ground.

IQ-mixer.

attenuator.

circulator with one impedance matched load.

low-pass filter.

band-pass filter.

d.c.-block.

linear amplifier.

$\hat{A}$ annihilation operator of a cavity mode excitation.

$\hat{a}$ annihilation operator of beam splitter output mode excitation.

$\hat{a}'$ annihilation operator of a cavity output mode excitation.

$\hat{a}'^{\dagger}$ creation operator of a cavity mode excitation.

$\hat{A}^{\dagger}$ creation operator of a cavity mode excitation.

$\hat{a}^{\dagger}$ creation operator of beam splitter output mode excitation.

$\varDelta$ detuning of artificial atom angular transition frequency ω_a from the resonator angular frequency ω_r.

$\varDelta\nu$ frequency bin width of discrete spectrum.

$\delta\tau$ delay time between single-photon generation.

E_c charging energy of the transmon.

E_J Josephson energy of the transmon.

$E_{\mathrm{J}\Sigma}$ maximum Josephson energy at zero flux through SQUID-loop.

$\mathcal{F}$ fast (discrete) Fourier transform.

$\mathcal{F}^{\text{-}1}$ inverse of the fast (discrete) Fourier transform.

f_s sampling frequency.

G quantum-mechanical correlation function.

g coupling rate between atom and cavity field.

$G^{(1)}$ quantum-mechanical first-order correlation function.

$G^{(2)}$ quantum-mechanical second-order correlation function.

$g^{(2)}$ normalized second-order correlation function.

$\mathit{\Gamma}$ measured ensemble average of correlation function.

γ decay rate of atom.

$\mathit{\Gamma}^{(1)}$ measured first-order correlation function.

$\mathit{\Gamma}^{(2)}$ measured second-order correlation function.

H expected correlation function of noise.

h Planck constant.

$H^{(1)}$ expected first-order correlation function of noise.

$H^{(2)}$ expected second-order correlation function of noise.

$\hbar$ reduced Planck constant $h/2\pi$.

$\hat{H}_\mathrm{JC}$ Jaynes-Cummings Hamiltonian.

I in-phase component of a complex amplitude.

κ cavity decay rate.

ν_a two-level atom transition frequency.

ν_if intermediate frequency.

ν_m carrier frequency of coherent measurement signal.

ν_r resonator frequency.

ω_a two-level atom angular transition frequency.

ω_c carrier angular frequency of microwave drive tone.

ω_d demodulation angular frequency.

ω_i artificial atom angular transition frequency between states $|g\rangle$ and $|i\rangle$.

ω_if intermediate angular frequency.

ω_LO local oscillator angular frequency.

$\mathit{\Omega}_\mathrm{R}$ Rabi rate.

ω_r resonator angular frequency.

$\mathit{\Omega}_\mathrm{sp}$ Mollow triplet side peak angular frequency.

Φ magnetic flux through SQUID-loop.

ϕ phase of a Rabi rotation.

Φ_0 superconducting flux quantum $\Phi_0 = h/2e$.

PSD power spectral density.

Q quadrature component of a complex amplitude.

S complex amplitude $I + i\,Q$ of a microwave signal.

$\hat{\sigma}_i$ atom lowering operator $|i\rangle\langle i+1|$.

$\hat{\sigma}_i^\dagger$ atom raising operator $|i+1\rangle\langle i|$.

$\hat{\sigma}_-$ qubit lowering operator $|g\rangle\langle e|$.

$\hat{\sigma}_+$ qubit raising operator $|e\rangle\langle g|$.

$\hat{\sigma}_x$ Pauli x-operator, $\hat{\sigma}_x = |g\rangle\langle e| + |e\rangle\langle g|$.

$\hat{\sigma}_y$ Pauli y-operator, $\hat{\sigma}_y = i(|e\rangle\langle g| - |g\rangle\langle e|)$.

$\hat{\sigma}_z$ Pauli z-operator, $\hat{\sigma}_z = |g\rangle\langle g| - |e\rangle\langle e|$.

θ Rabi angle.

T_p repetition period.

t_r repetition period of photon pulse generation.

t_s sampling period.

Z_0 waveguide impedance.

Acronyms

ADC analog-to-digital converter.

AWG arbitrary waveform generator.

BS beam splitter.

d.c. direct current, 0 Hz.

DAC digital-to-analog converter.

DDC digital down conversion.

ENOB effective number of bits.

FIR finite impulse response.

FPGA field programmable gate array.

FWHM full width at half maximum.

HBT Hanbury Brown and Twiss (1956).

HEMT	high electron mobility transistor.
HOM	Hong, Ou, and Mandel (1987).
HWHM	half width at half maximum.
IQ-mixer	passive four-port microwave component that mixes the two quadrature in/outputs I and Q or the radio frequency (RF) out/input with an local oscillator (LO).
LO	local oscillator.
PCB	printed circuit board.
QED	quantum electrodynamics.
QND	quantum non-demolition.
snr	signal to noise ratio.
SQUID	superconducting quantum interference device.

Bibliography

Agarwal, G. S. and S. Chaturvedi. *Scheme to measure the positive P distribution*. Phys. Rev. A **49**, R665 (1994).

Angelakis, D. G., M. F. Santos, and S. Bose. *Photon-blockade-induced Mott transitions and XY spin models in coupled cavity arrays*. Phys. Rev. A **76**, 031805 (2007).

Astafiev, O., Y. A. Pashkin, T. Yamamoto, Y. Nakamura, and J. S. Tsai. *Single-shot measurement of the Josephson charge qubit*. Phys. Rev. B **69**, 180507 (2004).

Astafiev, O., A. M. Zagoskin, A. A. Abdumalikov Jr., Y. A. Pashkin, T. Yamamoto, K. Inomata, Y. Nakamura, and J. S. Tsai. *Resonance Fluorescence of a Single Artificial Atom*. Science **327**, 840 (2010).

Bardeen, J., L. N. Cooper, and J. R. Schrieffer. *Theory of superconductivity*. Phys. Rev. **108**, 1175 (1957).

Bardyn, C.-E. and A. İmamoğlu. *Majorana-like Modes of Light in* *a One-Dimensional Array of Nonlinear Cavities.* Phys. Rev. Lett. **109**, 253606 (2012).

Baur, M. *Realizing quantum gates and algorithms with three superconducting qubits.* Ph.D. thesis, ETH Zurich (2012).

Baur, M., S. Filipp, R. Bianchetti, J. M. Fink, M. Göppl, L. Steffen, P. J. Leek, A. Blais, and A. Wallraff. *Measurement of Autler-Townes and Mollow Transitions in a Strongly Driven Superconducting Qubit.* Phys. Rev. Lett. **102**, 243602 (2009).

Bennett, C. H. and G. Brassard. *Quantum cryptography: public key distribution and coin tossing.* Int. Conf. on Computers, Systems and Signal Processing 175 (1984).

Bernien, H., L. Childress, L. Robledo, M. Markham, D. Twitchen, and R. Hanson. *Two-Photon Quantum Interference from Separate Nitrogen Vacancy Centers in Diamond.* Phys. Rev. Lett. **108**, 043604 (2012).

Bernien, H., B. Hensen, W. Pfaff, G. Koolstra, M. S. Blok, L. Robledo, T. H. Taminiau, M. Markham, D. J. Twitchen, L. Childress, and R. Hanson. *Heralded entanglement between solid-state qubits separated by three metres.* Nature **497**, 86 (2013).

Beugnon, J., M. P. A. Jones, J. Dingjan, B. Darquié, G. Messin, A. Browaeys, and P. Grangier. *Quantum interference between two single photons emitted by independently trapped atoms.* Nature **440**, 779 (2006).

Bianchetti, R., S. Filipp, M. Baur, J. M. Fink, M. Göppl, P. J. Leek, L. Steffen, A. Blais, and A. Wallraff. *Dynamics of dispersive single-qubit readout in circuit quantum electrodynamics.* Phys. Rev. A **80**, 043840 (2009).

Bianchetti, R., S. Filipp, M. Baur, J. M. Fink, C. Lang, L. Steffen, M. Boissonneault, A. Blais, and A. Wallraff. *Control and Tomography of a Three Level Superconducting Artificial Atom.* Phys. Rev. Lett. **105**, 223601 (2010).

Birnbaum, K. M., A. Boca, R. Miller, A. D. Boozer, T. E. Northup, and H. J. Kimble. *Photon blockade in an optical cavity with one trapped atom.* Nature **436**, 87 (2005).

Bishop, L. S., J. M. Chow, J. Koch, A. A. Houck, M. H. Devoret, E. Thuneberg, S. M. Girvin, and R. J. Schoelkopf. *Nonlinear response of the vacuum Rabi resonance.* Nat. Phys. **5**, 105 (2009).

Blais, A., J. Gambetta, A. Wallraff, D. I. Schuster, S. M. Girvin, M. H. Devoret, and R. J. Schoelkopf. *Quantum-information processing with circuit quantum electrodynamics.* Phys. Rev. A **75**, 032329 (2007).

Blais, A., R.-S. Huang, A. Wallraff, S. M. Girvin, and R. J. Schoelkopf. *Cavity quantum electrodynamics for superconducting electrical circuits: An architecture for quantum computation.* Phys. Rev. A **69**, 062320 (2004).

Bocquillon, E., V. Freulon, J.-M. Berroir, P. Degiovanni, B. Plaçais, A. Cavanna, Y. Jin, and G. Fève. *Coherence and Indistinguishability of Single Electrons Emitted by Independent Sources.* Science **339**, 1054 (2013).

Boissonneault, M., J. M. Gambetta, and A. Blais. *Improved Superconducting Qubit Readout by Qubit-Induced Nonlinearities.* Phys. Rev. Lett. **105**, 100504 (2010).

Bozyigit, D., C. Lang, L. Steffen, J. M. Fink, C. Eichler, M. Baur, R. Bianchetti, P. J. Leek, S. Filipp, M. P. da Silva, A. Blais, and A. Wallraff. *Antibunching of microwave-frequency photons observed in correlation measurements using linear detectors.* Nat. Phys. **7**, 154 (2011a).

Bozyigit, D., C. Lang, L. Steffen, J. M. Fink, C. Eichler, M. Baur, R. Bianchetti, P. J. Leek, S. Filipp, A. Wallraff, M. P. da Silva, and A. Blais. *Correlation measurements of individual microwave photons emitted from a symmetric cavity.* J. Phys.: Conf. Ser. **264**, 012024 (2011b).

Carmichael, H. J. *Statistical Methods in Quantum Optics 1: Master Equations and Fokker-Planck Equations* (Springer-Verlag, Berlin, 2002), 2nd edition.

Carmichael, H. J. *Statistical Methods in Quantum Optics 2: Non-Classical Fields* (Springer-Verlag, Berlin, 2008).

Carmichael, H. J. and D. F. Walls. *A quantum-mechanical master equation treatment of the dynamical Stark effect*. J. Phys. B **9**, 1199 (1976).

Caves, C. M. *Quantum limits on noise in linear amplifiers*. Phys. Rev. D **26**, 1817 (1982).

Chen, Y.-F., D. Hover, S. Sendelbach, L. Maurer, S. T. Merkel, E. J. Pritchett, F. K. Wilhelm, and R. McDermott. *Microwave Photon Counter Based on Josephson Junctions*. Phys. Rev. Lett. **107**, 217401 (2011).

Chow, J. M., L. DiCarlo, J. M. Gambetta, F. Motzoi, L. Frunzio, S. M. Girvin, and R. J. Schoelkopf. *Optimized driving of superconducting artificial atoms for improved single-qubit gates*. Phys. Rev. A **82**, 040305 (2010).

Cicak, K., M. Allman, J. Strong, K. Osborn, and R. Simmonds. *Vacuum-Gap Capacitors for Low-Loss Superconducting Resonant Circuits*. Applied Superconductivity, IEEE Transactions on **19**, 948 (2009).

Clarke, J. and F. K. Wilhelm. *Superconducting quantum bits*. Nature **453**, 1031 (2008).

Córcoles, A. D., J. M. Chow, J. M. Gambetta, C. Rigetti, J. R. Rozen, G. A. Keefe, M. B. Rothwell, M. B. Ketchen, and M. Steffen. *Protecting superconducting qubits from radiation*. Appl. Phys. Lett. **99**, 181906 (2011).

Deleglise, S., I. Dotsenko, C. Sayrin, J. Bernu, M. Brune, J.-M. Raimond, and S. Haroche. *Reconstruction of non-classical cavity* *field states with snapshots of their decoherence.* Nature **455**, 510 (2008).

Duan, L.-M. and C. Monroe. *Colloquium: Quantum networks with trapped ions.* Rev. Mod. Phys. **82**, 1209 (2010).

Eichler, C., D. Bozyigit, C. Lang, M. Baur, L. Steffen, J. M. Fink, S. Filipp, and A. Wallraff. *Observation of Two-Mode Squeezing in the Microwave Frequency Domain.* Phys. Rev. Lett. **107**, 113601 (2011a).

Eichler, C., D. Bozyigit, C. Lang, L. Steffen, J. Fink, and A. Wallraff. *Experimental State Tomography of Itinerant Single Microwave Photons.* Phys. Rev. Lett. **106**, 220503 (2011b).

Eichler, C., D. Bozyigit, and A. Wallraff. *Characterizing quantum microwave radiation and its entanglement with superconducting qubits using linear detectors.* Phys. Rev. A **86**, 032106 (2012).

Eichler, C., C. Lang, J. M. Fink, J. Govenius, S. Filipp, and A. Wallraff. *Observation of Entanglement between Itinerant Microwave Photons and a Superconducting Qubit.* Phys. Rev. Lett. **109**, 240501 (2012).

Eichler, C. and A. Wallraff. *Controlling the dynamic range of a Josephson parametric amplifier.* EPJ Quantum Technology **1**, 2 (2014).

Einstein, A. *Über einen die Erzeugung und Verwandlung des Lichtes betreffenden heuristischen Gesichtspunkt.* Ann. Phys. **322**, 132 (1905).

Faraon, A., I. Fushman, D. Englund, N. Stoltz, P. Petroff, and J. Vuckovic. *Coherent generation of non-classical light on a chip via photon-induced tunnelling and blockade.* Nat. Phys. **4**, 859 (2008).

Filipp, S., P. Maurer, P. J. Leek, M. Baur, R. Bianchetti, J. M. Fink, M. Göppl, L. Steffen, J. M. Gambetta, A. Blais, and A. Wallraff.

Two-Qubit State Tomography Using a Joint Dispersive Readout. Phys. Rev. Lett. **102**, 200402 (2009).

Fink, J. M., M. Göppl, M. Baur, R. Bianchetti, P. J. Leek, A. Blais, and A. Wallraff. *Climbing the Jaynes-Cummings ladder and observing its nonlinearity in a cavity QED system.* Nature **454**, 315 (2008).

Fink, J. M., L. Steffen, P. Studer, L. S. Bishop, M. Baur, R. Bianchetti, D. Bozyigit, C. Lang, S. Filipp, P. J. Leek, and A. Wallraff. *Quantum-To-Classical Transition in Cavity Quantum Electrodynamics.* Phys. Rev. Lett. **105**, 163601 (2010).

Flagg, E. B., A. Muller, S. V. Polyakov, A. Ling, A. Migdall, and G. S. Solomon. *Interference of Single Photons from Two Separate Semiconductor Quantum Dots.* Phys. Rev. Lett. **104**, 137401 (2010).

Frey, T. *Design of microwave beam splitters for photon correlation measurements.* Master's thesis, ETH Zurich (2008).

Frey, T., P. J. Leek, M. Beck, K. Ensslin, A. Wallraff, and T. Ihn. *Characterization of a microwave frequency resonator via a nearby quantum dot.* Appl. Phys. Lett. **98**, 262105 (2011).

Gabelli, J., L.-H. Reydellet, G. Feve, J.-M. Berroir, B. Placais, P. Roche, and D. C. Glattli. *Hanbury Brown–Twiss Correlations to Probe the Population Statistics of GHz Photons Emitted by Conductors.* Phys. Rev. Lett. **93**, 056801 (2004).

Gambetta, J., W. A. Braff, A. Wallraff, S. M. Girvin, and R. J. Schoelkopf. *Protocols for optimal readout of qubits using a continuous quantum nondemolition measurement.* Phys. Rev. A **76**, 012325 (2007).

Gambetta, J. M., F. Motzoi, S. T. Merkel, and F. K. Wilhelm. *Analytic control methods for high-fidelity unitary operations in a weakly nonlinear oscillator.* Phys. Rev. A **83**, 012308 (2011).

Gardiner, C. W. and M. J. Collett. *Input and output in damped quantum systems: Quantum stochastic differential equations and the master equation.* Phys. Rev. A **31**, 3761 (1985).

Göppl, M. *Engineering Quantum Electronic Chips - Realization and Characterization of Circuit Quantum Electrodynamics Systems.* Ph.D. thesis, ETH Zurich (2009).

Göppl, M., A. Fragner, M. Baur, R. Bianchetti, S. Filipp, J. M. Fink, P. J. Leek, G. Puebla, L. Steffen, and A. Wallraff. *Coplanar Waveguide Resonators for Circuit Quantum Electrodynamics.* J. Appl. Phys. **104**, 113904 (2008).

Greentree, A. D., C. Tahan, J. H. Cole, and L. C. L. Hollenberg. *Quantum phase transitions of light.* Nat. Phys. **2**, 856 (2006).

Grosse, N. B., T. Symul, M. Stobinska, T. C. Ralph, and P. K. Lam. *Measuring Photon Antibunching from Continuous Variable Sideband Squeezing.* Phys. Rev. Lett. **98**, 153603 (2007).

Hanbury Brown, R. and R. Q. Twiss. *Correlation between Photons in two Coherent Beams of Light.* Nature **177**, 27 (1956).

Haroche, S. *Fundamental Systems in Quantum Optics*, chapter Cavity quantum electrodynamics (Elsevier, New York, 1992).

Haroche, S. *Nobel Lecture: Controlling photons in a box and exploring the quantum to classical boundary.* Rev. Mod. Phys. **85**, 1083 (2013).

Haroche, S. and J.-M. Raimond. *Exploring the Quantum: Atoms, Cavities, and Photons* (Oxford University Press, New York, USA, 2006).

Hartmann, M., F. Brandao, and M. Plenio. *Quantum many-body phenomena in coupled cavity arrays.* Laser & Photon. Rev. **2**, 527 (2008).

Hoffman, A. J., S. J. Srinivasan, S. Schmidt, L. Spietz, J. Aumentado, H. E. Türeci, and A. A. Houck. *Dispersive Photon Blockade in a Superconducting Circuit.* Phys. Rev. Lett. **107**, 053602 (2011).

Hofheinz, M., H. Wang, M. Ansmann, R. C. Bialczak, E. Lucero, M. Neeley, A. D. O'Connell, D. Sank, J. Wenner, J. M. Martinis, and A. N. Cleland. *Synthesizing arbitrary quantum states in a superconducting resonator*. Nature **459**, 546 (2009).

Hofheinz, M., E. M. Weig, M. Ansmann, R. C. Bialczak, E. Lucero, M. Neeley, A. D. O'Connell, H. Wang, J. M. Martinis, and A. N. Cleland. *Generation of Fock states in a superconducting quantum circuit*. Nature **454**, 310 (2008).

Hofmann, J., M. Krug, N. Ortegel, L. Gérard, M. Weber, W. Rosenfeld, and H. Weinfurter. *Heralded Entanglement Between Widely Separated Atoms*. Science **337**, 72 (2012).

Hoi, I.-C., T. Palomaki, J. Lindkvist, G. Johansson, P. Delsing, and C. M. Wilson. *Generation of Nonclassical Microwave States Using an Artificial Atom in 1D Open Space*. Phys. Rev. Lett. **108**, 263601 (2012).

Hong, C. K., Z. Y. Ou, and L. Mandel. *Measurement of Subpicosecond Time Intervals between Two Photons by Interference*. Phys. Rev. Lett. **59**, 2044 (1987).

Houck, A., D. Schuster, J. Gambetta, J. Schreier, B. Johnson, J. Chow, L. Frunzio, J. Majer, M. Devoret, S. Girvin, and R. Schoelkopf. *Generating single microwave photons in a circuit*. Nature **449**, 328 (2007).

Houck, A. A., J. A. Schreier, B. R. Johnson, J. M. Chow, J. Koch, J. M. Gambetta, D. I. Schuster, L. Frunzio, M. H. Devoret, S. M. Girvin, and R. J. Schoelkopf. *Controlling the Spontaneous Emission of a Superconducting Transmon Qubit*. Phys. Rev. Lett. **101**, 080502 (2008).

İmamoğlu, A., H. Schmidt, G. Woods, and M. Deutsch. *Strongly Interacting Photons in a Nonlinear Cavity*. Phys. Rev. Lett. **79**, 1467 (1997).

Israel, Y., I. Afek, S. Rosen, O. Ambar, and Y. Silberberg. *Experimental tomography of NOON states with large photon numbers.* Phys. Rev. A **85**, 022115 (2012).

Kaltenbaek, R., B. Blauensteiner, M. Żukowski, M. Aspelmeyer, and A. Zeilinger. *Experimental Interference of Independent Photons.* Phys. Rev. Lett. **96**, 240502 (2006).

Kimble, H. J. *The quantum internet.* Nature **453**, 1023 (2008).

Kiraz, A., M. Ehrl, T. Hellerer, Ö. E. Müstecaplılğu, C. Bräuchle, and A. Zumbusch. *Indistinguishable Photons from a Single Molecule.* Phys. Rev. Lett. **94**, 223602 (2005).

Knill, E., R. Laflamme, and G. J. Milburn. *A scheme for efficient quantum computation with linear optics.* Nature **409**, 46 (2001).

Koch, J. and K. Le Hur. *Superfluid-Mott-insulator transition of light in the Jaynes-Cummings lattice.* Phys. Rev. A **80**, 023811 (2009).

Koch, J., T. M. Yu, J. Gambetta, A. A. Houck, D. I. Schuster, J. Majer, A. Blais, M. H. Devoret, S. M. Girvin, and R. J. Schoelkopf. *Charge-insensitive qubit design derived from the Cooper pair box.* Phys. Rev. A **76**, 042319 (2007).

Lang, C. *Read-Out Strategies for Multi-Qubit States in Circuit Quantum Electrodynamics.* Diploma thesis, ETH Zurich and LMU Munich (2009).

Lang, C., D. Bozyigit, C. Eichler, L. Steffen, J. M. Fink, A. A. Abdumalikov Jr., M. Baur, S. Filipp, M. P. da Silva, A. Blais, and A. Wallraff. *Observation of Resonant Photon Blockade at Microwave Frequencies Using Correlation Function Measurements.* Phys. Rev. Lett. **106**, 243601 (2011).

Lang, C., D. Bozyigit, Y. Salathe, C. Eichler, and A. Wallraff. *Quantum Signal Analyzer for Itinerant Microwave Radiation.* in preparation (2013a).

Lang, C., C. Eichler, L. Steffen, J. M. Fink, M. J. Woolley, A. Blais, and A. Wallraff. *Correlations, indistinguishability and entanglement in Hong-Ou-Mandel experiments at microwave frequencies*. Nat. Phys. **9**, 345 (2013b).

Legero, T., T. Wilk, M. Hennrich, G. Rempe, and A. Kuhn. *Quantum Beat of Two Single Photons*. Phys. Rev. Lett. **93**, 070503 (2004).

Legero, T., T. Wilk, A. Kuhn, and G. Rempe. *Time-resolved two-photon quantum interference*. Appl. Phys. B: Lasers Opt. **77**, 797 (2003).

Lettow, R., Y. L. A. Rezus, A. Renn, G. Zumofen, E. Ikonen, S. Götzinger, and V. Sandoghdar. *Quantum Interference of Tunably Indistinguishable Photons from Remote Organic Molecules*. Phys. Rev. Lett. **104**, 123605 (2010).

Lucero, E., J. Kelly, R. C. Bialczak, M. Lenander, M. Mariantoni, M. Neeley, A. D. O'Connell, D. Sank, H. Wang, M. Weides, J. Wenner, T. Yamamoto, A. N. Cleland, and J. M. Martinis. *Reduced phase error through optimized control of a superconducting qubit*. Phys. Rev. A **82**, 042339 (2010).

Lyons, R. G. *Understanding Digital Signal Processing* (Prentice Hall PTR, Upper Saddle River, NJ, USA, 2004), 2nd edition.

Makhlin, Y., G. Schön, and A. Shnirman. *Quantum-state engineering with Josephson-junction devices*. Rev. Mod. Phys. **73**, 357 (2001).

Mallet, F., F. R. Ong, A. Palacios-Laloy, F. Nguyen, P. Bertet, D. Vion, and D. Esteve. *Single-shot qubit readout in circuit quantum electrodynamics*. Nat. Phys. **5**, 791 (2009).

Mandel, L. and E. Wolf. *Optical Coherence and Quantum Optics* (Cambridge University Press, 1995).

Mariantoni, M., E. P. Menzel, F. Deppe, M. A. Araque Caballero, A. Baust, T. Niemczyk, E. Hoffmann, E. Solano, A. Marx, and R. Gross. *Planck Spectroscopy and Quantum Noise of Microwave Beam Splitters*. Phys. Rev. Lett. **105**, 133601 (2010).

Marx, S. *Optimization of the microwave properties of a cryostat sample holder*. Master's thesis, ETH Zurich (2009).

Maunz, P., D. L. Moehring, S. Olmschenk, K. C. Younge, D. N. Matsukevich, and C. Monroe. *Quantum interference of photon pairs from two remote trapped atomic ions*. Nat. Phys. **3**, 538 (2007).

McDermott, R., R. W. Simmonds, M. Steffen, K. B. Cooper, K. Cicak, K. D. Osborn, S. Oh, D. P. Pappas, and J. M. Martinis. *Simultaneous state measurement of coupled Josephson phase qubits*. Science **307**, 1299 (2005).

Menzel, E. P., F. Deppe, M. Mariantoni, M. A. Araque Caballero, A. Baust, T. Niemczyk, E. Hoffmann, A. Marx, E. Solano, and R. Gross. *Dual-Path State Reconstruction Scheme for Propagating Quantum Microwaves and Detector Noise Tomography*. Phys. Rev. Lett. **105**, 100401 (2010).

Menzel, E. P., R. Di Candia, F. Deppe, P. Eder, L. Zhong, M. Ihmig, M. Haeberlein, A. Baust, E. Hoffmann, D. Ballester, K. Inomata, T. Yamamoto, Y. Nakamura, E. Solano, A. Marx, and R. Gross. *Path Entanglement of Continuous-Variable Quantum Microwaves*. Phys. Rev. Lett. **109**, 250502 (2012).

Mlynek, J. A., A. A. Abdumalikov, J. M. Fink, L. Steffen, M. Baur, C. Lang, A. F. van Loo, and A. Wallraff. *Demonstrating W-type entanglement of Dicke states in resonant cavity quantum electrodynamics*. Phys. Rev. A **86**, 053838 (2012).

Moehring, D. L., P. Maunz, S. Olmschenk, K. C. Younge, D. N. Matsukevich, L. M. Duan, and C. Monroe. *Entanglement of single-atom quantum bits at a distance*. Nature **449**, 68 (2007).

Mollow, B. R. *Power Spectrum of Light Scattered by Two-Level Systems*. Phys. Rev. **188**, 1969 (1969).

Motzoi, F., J. M. Gambetta, P. Rebentrost, and F. K. Wilhelm. *Simple Pulses for Elimination of Leakage in Weakly Nonlinear Qubits*. Phys. Rev. Lett. **103**, 110501 (2009).

Nakamura, Y., C. D. Chen, and J. S. Tsai. *Spectroscopy of Energy-Level Splitting between Two Macroscopic Quantum States of Charge Coherently Superposed by Josephson Coupling*. Phys. Rev. Lett. **79**, 2328 (1997).

Nguyen, F., E. Zakka-Bajjani, R. W. Simmonds, and J. Aumentado. *Quantum Interference between Two Single Photons of Different Microwave Frequencies*. Phys. Rev. Lett. **108**, 163602 (2012).

O'Brien, J. L., A. Furusawa, and J. Vučković. *Photonic quantum technologies*. Nat. Photon. **3**, 687 (2009).

Okean, H. and A. Kelly. *Low-Noise Receiver Design Trends Using State-of-the-Art Building Blocks*. Microwave Theory and Techniques, IEEE Transactions on **25**, 254 (1977).

Paik, H., D. I. Schuster, L. S. Bishop, G. Kirchmair, G. Catelani, A. P. Sears, B. R. Johnson, M. J. Reagor, L. Frunzio, L. I. Glazman, S. M. Girvin, M. H. Devoret, and R. J. Schoelkopf. *Observation of High Coherence in Josephson Junction Qubits Measured in a Three-Dimensional Circuit QED Architecture*. Phys. Rev. Lett. **107**, 240501 (2011).

Patel, R. B., A. J. Bennett, I. Farrer, C. A. Nicoll, D. A. Ritchie, and A. J. Shields. *Two-photon interference of the emission from electrically tunable remote quantum dots*. Nat. Photon. **4**, 632 (2010).

Peterer, M. *Investigating the suppression of external sources of decoherence in transmon qubits*. Master's thesis, ETH Zurich (2012).

Planck, M. *Ueber irreversible Strahlungsvorgänge*. Ann. Phys. **306**, 69 (1900).

Planck, M. *Ueber das Gesetz der Energieverteilung im Normalspectrum*. Ann. Phys. **309**, 553 (1901).

Pozar, D. M. *Microwave engineering* (John Wiley & Sons, Inc., 2011), 4th edition.

Puebla-Hellmann, G. and A. Wallraff. *Realization of gigahertz-frequency impedance matching circuits for nano-scale devices*. Appl. Phys. Lett. **101**, 053108 (2012).

Purcell, E. M. *Spontaneous Emission Probabilties at Radio Frequencies*. Phys. Rev. **69**, 681 (1946).

Reed, M. D., L. DiCarlo, B. R. Johnson, L. Sun, D. I. Schuster, L. Frunzio, and R. J. Schoelkopf. *High-Fidelity Readout in Circuit Quantum Electrodynamics Using the Jaynes-Cummings Nonlinearity*. Phys. Rev. Lett. **105**, 173601 (2010).

Riedmatten, H. d., I. Marcikic, W. Tittel, H. Zbinden, and N. Gisin. *Quantum interference with photon pairs created in spatially separated sources*. Phys. Rev. A **67**, 022301 (2003).

Ristè, D., C. C. Bultink, K. W. Lehnert, and L. DiCarlo. *Feedback Control of a Solid-State Qubit Using High-Fidelity Projective Measurement*. Phys. Rev. Lett. **109**, 240502 (2012).

Ristè, D., M. Dukalski, C. A. Watson, G. de Lange, M. J. Tiggelman, Y. M. Blanter, K. W. Lehnert, R. N. Schouten, and L. DiCarlo. *Deterministic entanglement of superconducting qubits by parity measurement and feedback*. Nature **502**, 350 (2013).

Romero, G., J. J. García-Ripoll, and E. Solano. *Microwave Photon Detector in Circuit QED*. Phys. Rev. Lett. **102**, 173602 (2009).

Sanaka, K., A. Pawlis, T. D. Ladd, K. Lischka, and Y. Yamamoto. *Indistinguishable Photons from Independent Semiconductor Nanostructures*. Phys. Rev. Lett. **103**, 053601 (2009).

Santori, C., D. Fattal, J. Vučković, G. S. Solomon, and Y. Yamamoto. *Indistinguishable photons from a single-photon device*. Nature **419**, 594 (2002).

Sayrin, C., I. Dotsenko, X. Zhou, B. Peaudecerf, T. Rybarczyk, S. Gleyzes, P. Rouchon, M. Mirrahimi, H. Amini, M. Brune, J.-M. Raimond, and S. Haroche. *Real-time quantum feedback prepares and stabilizes photon number states*. Nature **477**, 73 (2011).

Schmidt, S., D. Gerace, A. A. Houck, G. Blatter, and H. E. Türeci. *Nonequilibrium delocalization-localization transition of photons in circuit quantum electrodynamics*. Phys. Rev. B **82**, 100507 (2010).

Schoelkopf, R. J. and S. M. Girvin. *Wiring up quantum systems*. Nature **451**, 664 (2008).

Schreier, J., A. Houck, J. Koch, D. I. Schuster, B. Johnson, J. Chow, J. Gambetta, J. Majer, L. Frunzio, M. Devoret, S. Girvin, and R. Schoelkopf. *Suppressing charge noise decoherence in superconducting charge qubits*. Phys. Rev. B **77**, 180502 (2008).

Schuster, D. I., A. Wallraff, A. Blais, L. Frunzio, R.-S. Huang, J. Majer, S. M. Girvin, and R. J. Schoelkopf. *AC Stark shift and dephasing of a superconducting qubit strongly coupled to a cavity field*. Phys. Rev. Lett. **94**, 123602 (2005).

Schuster, I., A. Kubanek, A. Fuhrmanek, T. Puppe, P. W. H. Pinkse, K. Murr, and G. Rempe. *Nonlinear spectroscopy of photons bound to one atom*. Nat. Phys. **4**, 382 (2008).

Scully, M. O. and M. S. Zubairy. *Quantum Optics* (Cambridge University Press, 1997).

Shadbolt, P. J., M. R. Verde, A. Peruzzo, A. Politi, A. Laing, M. Lobino, J. C. F. Matthews, M. G. Thompson, and J. L. O'Brien. *Generating, manipulating and measuring entanglement and mixture with a reconfigurable photonic circuit*. Nat. Photon. **6**, 45 (2012).

Siddiqi, I., R. Vijay, M. Metcalfe, E. Boaknin, L. Frunzio, R. J. Schoelkopf, and M. H. Devoret. *Dispersive measurements of superconducting qubit coherence with a fast latching readout*. Phys. Rev. B **73**, 054510 (2006).

Siddiqi, I., R. Vijay, F. Pierre, C. M. Wilson, M. Metcalfe, C. Rigetti, L. Frunzio, and M. H. Devoret. *RF-Driven Josephson Bifurcation Amplifier for Quantum Measurement*. Phys. Rev. Lett. **93**, 207002 (2004).

Sillanpää, M. A., J. Li, K. Cicak, F. Altomare, J. I. Park, R. W. Simmonds, G. S. Paraoanu, and P. J. Hakonen. *Autler-Townes Effect in a Superconducting Three-Level System*. Phys. Rev. Lett. **103**, 193601 (2009).

da Silva, M. P., D. Bozyigit, A. Wallraff, and A. Blais. *Schemes for the observation of photon correlation functions in circuit QED with linear detectors*. Phys. Rev. A **82**, 043804 (2010).

Sipahigil, A., M. L. Goldman, E. Togan, Y. Chu, M. Markham, D. J. Twitchen, A. S. Zibrov, A. Kubanek, and M. D. Lukin. *Quantum Interference of Single Photons from Remote Nitrogen-Vacancy Centers in Diamond*. Phys. Rev. Lett. **108**, 143601 (2012).

Steffen, L., Y. Salathe, M. Oppliger, P. Kurpiers, M. Baur, C. Lang, C. Eichler, G. Puebla-Hellmann, A. Fedorov, and A. Wallraff. *Deterministic quantum teleportation with feed-forward in a solid state system*. Nature **500**, 319 (2013).

Steffen, M., M. Ansmann, R. McDermott, N. Katz, R. C. Bialczak, E. Lucero, M. Neeley, E. M. Weig, A. N. Cleland, and J. M. Martinis. *State tomography of capacitively shunted phase qubits with high fidelity*. Phys. Rev. Lett. **97**, 050502 (2006).

Steudle, G. A., S. Schietinger, D. Höckel, S. N. Dorenbos, I. E. Zadeh, V. Zwiller, and O. Benson. *Measuring the quantum nature of light with a single source and a single detector*. Phys. Rev. A **86**, 053814 (2012).

Thompson, R. J., G. Rempe, and H. J. Kimble. *Observation of normal-mode splitting for an atom in an optical cavity*. Phys. Rev. Lett. **68**, 1132 (1992).

Tian, L. and H. J. Carmichael. *Quantum trajectory simulations of two-state behavior in an optical cavity containing one atom*. Phys. Rev. A **46**, R6801 (1992).

VeriCold. *Cryofree™ DR200-10*. VeriCold Technologies, An Oxford Instruments Company (2008).

Vidal, G. and R. F. Werner. *Computable measure of entanglement.* Phys. Rev. A **65**, 032314 (2002).

Vijay, R., M. H. Devoret, and I. Siddiqi. *Invited Review Article: The Josephson bifurcation amplifier.* Rev. Sci. Instrum. **80**, 111101 (2009).

Vijay, R., D. H. Slichter, and I. Siddiqi. *Observation of Quantum Jumps in a Superconducting Artificial Atom.* Phys. Rev. Lett. **106**, 110502 (2011).

Vion, D., A. Aassime, A. Cottet, P. Joyez, H. Pothier, C. Urbina, D. Esteve, and M. H. Devoret. *Manipulating the quantum state of an electrical circuit.* Science **296**, 886 (2002).

Wallraff, A. *Quantenmechanik mit Schaltkreisen: Photonen und Qubits auf einem supraleitenden Mikrochip.* Physik Journal **7**, 39 (2008).

Wallraff, A., D. I. Schuster, A. Blais, L. Frunzio, R.-S. Huang, J. Majer, S. Kumar, S. M. Girvin, and R. J. Schoelkopf. *Strong coupling of a single photon to a superconducting qubit using circuit quantum electrodynamics.* Nature **431**, 162 (2004).

Wallraff, A., D. I. Schuster, A. Blais, L. Frunzio, J. Majer, S. M. Girvin, and R. J. Schoelkopf. *Approaching Unit Visibility for Control of a Superconducting Qubit with Dispersive Readout.* Phys. Rev. Lett. **95**, 060501 (2005).

Walls, D. F. and G. J. Milburn. *Quantum Optics* (Springer Verlag, Berlin, 2008), 2nd edition.

Wang, H., M. Mariantoni, R. C. Bialczak, M. Lenander, E. Lucero, M. Neeley, A. D. O'Connell, D. Sank, M. Weides, J. Wenner, T. Yamamoto, Y. Yin, J. Zhao, J. M. Martinis, and A. N. Cleland. *Deterministic Entanglement of Photons in Two Superconducting Microwave Resonators.* Phys. Rev. Lett. **106**, 060401 (2011).

Wineland, D. J. *Nobel Lecture: Superposition, entanglement, and raising Schrödinger's cat.* Rev. Mod. Phys. **85**, 1103 (2013).

Woolley, M. J., C. Lang, C. Eichler, A. Wallraff, and A. Blais. *Signatures of Hong-Ou-Mandel Interference at Microwave Frequencies.* New J. Phys. **15**, 105025 (2013).

Xilinx. *Virtex-4 Family Overview, DS112 (v3.1).* Xilinx (2010).

Yalamanchili, S. *Introductory VHDL: From Simulation To Synthesis* (Prentice Hall, New Jersey, 2001).

Yoshie, T., A. Scherer, J. Hendrickson, G. Khitrova, H. M. Gibbs, G. Rupper, C. Ell, O. B. Shchekin, and D. G. Deppe. *Vacuum Rabi splitting with a single quantum dot in a photonic crystal nanocavity.* Nature **432**, 200 (2004).

Zou, X. T. and L. Mandel. *Photon-antibunching and sub-Poissonian photon statistics.* Phys. Rev. A **41**, 475 (1990).

Acknowledgements

I owe thanks to numerous people who supported and encouraged me during my PhD work. Without their help and support the success of the experiments presented in this thesis would never have been possible.

First of all I would like to thank my advisor Andreas Wallraff for giving me the possibility to carry out this interesting PhD thesis project. I am very thankful for introducing me into the field of circuit QED and letting me work with FPGAs, which perfectly matched my personal interests in quantum information processing and electronics. I am also very grateful for his continuous support and steady encouragement, and that I could profit from his expertise and scientific skills.

I would also like to thank all my colleagues of the Quantum Device Lab for an inspiring and always nice and supportive working atmosphere. Each of them contributed to some aspect of this thesis work. My special thanks go to Christopher Eichler for the close collaboration, many productive discussions, and proofreading this thesis. I thank Deniz Bozyigit for co-working with me on the single-photon correlation function measurements and for his electrical engineering expertise, from which I profited gratefully. Moreover, I want to thank Lars Steffen, Matthias Baur, Jonas Mlynek, Tobias Thiele and Markus Oppliger for the great time, and many mind-broadening and supportive discussions we had in our office. I thank Abdufarrukh Abdumalikov, Christopher Eichler and Stefan Filipp for their help with my theoretical questions. I am thankful to our former colleague Romeo Bianchetti for teaching me how to handle the dilution refrigerator, being always helpful and very supportive, and cheering the working atmosphere. Thanks go to Lars Steffen for fabricating my chips with air bridges, and to Johannes Fink for fabricating the transmon qubits on these chips. I thank my former master student and new colleague Yves Salathé for his work on our FPGAs, and that he will continue to take care over the FPGA facilities and moving them forward. Furthermore, I am thankful to Arjan van Loo who did the photographs in this thesis. I am grateful to Gaby Strahm for all her administrative help and her delicious cakes. Many thanks go to Janis Lütolf for all his valuable technical help and advice, and for his new persistent ordering system for the workshop and laboratory. I appreciate the development of the beam splitter by Peter Leek and his semester students Tobias Frey, Dominik Henzen and Gebhard Littich.

I owe thanks to Alexandre Blais, Marcus da Silva and Matthew Woolley for the very fruitful collaborations and their theoretical support formulated in close relation to the experiments. I appreciate the quantum optics lecture of Ataç İmamoğlu from which I got much inspiration for my experiments. I express my gratitude to Denis Vion that he kindly accepted to take his time to co-examine my thesis, and thank Andreas Vaterlaus for being the chair of my thesis committee.

I cannot thank enough my family and friends, in particular my parents, who supported me during all my education, and my father for his constant interest and reading this thesis. I thank my grandmother who steadily wished me the best for my experiments. Very special thanks go to my partner Andrea for so many things, for supporting me, for reading this thesis, for her company in long nights of work. I appreciate her constant encouragement and thank her for making all past years so precious.

Curriculum Vitae

Personal Data

Name: Christian Lang

Date of Birth: December 31, 1980 in Munich, Germany

Nationality: German

Education

ETH Zurich, Switzerland

01/2010 - 02/2014 *Doctoral studies in Physics*

Quantum Microwave Radiation and its Interference Characterized by Correlation Function Measurements in Circuit Quantum Electrodynamics.

Advisor: Prof. Andreas Wallraff.

Co-examiner: Dr. Denis Vion.

ETH Zurich, Switzerland

06/2008 - 06/2009 *External diploma thesis*

Read-Out Strategies for Multi-Qubit States in Circuit Quantum Electrodynamics.

Advisor: Prof. Andreas Wallraff.

Universidad Complutense de Madrid, Spain

09/2005 - 03/2006 *ERASMUS scholarship*

Department of Mathematics

LMU Munich, Germany

10/2002 - 06/2009 *Diploma in Physics*

Applied Physics: Quantum communication and information, Electronics; Optional subject: Statistics

Städtisches Luisengymnasium, Munich, Germany

09/1992 - 07/2001 *Abitur* (German university entrance qualification)

Professional Experience

	ETH Zurich, Switzerland
07/2009 - 12/2009	*Scientific Assistant* in Quantum Device Lab
	GSF Neuherberg, Germany
10/2004 - 12/2004	*Student Assistant* in Institute of Bioinformatics
	LMU Munich, Germany
08/2004 - 12/2004	*Working Student* in Department of Statistics
	Medical Center of the University of Munich
07/2002 - 10/2002	*Working Student* in Computing Center
	Medical Center of the University of Munich
09/2001 - 06/2002	*Alternative Service* in Computing Center
	FC Puchheim, Fürstenfeldbruck, Germany
06/1998 - 03/2004	*Badminton Trainer*

Publications

Signatures of Hong-Ou-Mandel interference at microwave frequencies, M. J. Woolley, **C. Lang**, C. Eichler, A. Wallraff, and A. Blais, *New J. Phys.* **15**, 105025 (2013).

Deterministic quantum teleportation with feed-forward in a solid state system, L. Steffen, Y. Salathe, M. Oppliger, P. Kurpiers, M. Baur, **C. Lang**, C. Eichler, G. Puebla-Hellmann, A. Fedorov, and A. Wallraff, *Nature* **500**, 319 (2013).

Correlations, indistinguishability and entanglement in Hong-Ou-Mandel experiments at microwave frequencies, **C. Lang**, C. Eichler, L. Steffen, J. M. Fink, M. J. Woolley, A. Blais, and A. Wallraff, *Nat. Phys.* **9**, 345 (2013).

Observation of Entanglement between Itinerant Microwave Photons and a Superconducting Qubit, C. Eichler, **C. Lang**, J. M. Fink, J. Govenius, S. Filipp, and A. Wallraff, *Phys. Rev. Lett.* **109**, 240501 (2012).

Demonstrating W-type Entanglement of Dicke states in resonant cavity quantum electrodynamics, J. A. Mlynek, A. A. Abdumalikov Jr., J. M. Fink, L. Steffen, M. Baur, **C. Lang**, A. F. van Loo, and A. Wallraff, *Phys. Rev. A* **86**, 053838 (2012).

Observation of Two-Mode Squeezing in the Microwave Frequency Domain, C. Eichler, D. Bozyigit, **C. Lang**, M. Baur, L. Steffen, J. M. Fink, S. Filipp, and A. Wallraff, *Phys. Rev. Lett.* **107**, 113601 (2011).

Observation of Resonant Photon Blockade at Microwave Frequencies Using Correlation Function Measurements, **C. Lang**, D. Bozyigit, C. Eichler, L. Steffen, J. M. Fink, A. A. Abdumalikov, M. Baur, S. Filipp, M. P. da Silva, A. Blais, and A. Wallraff, *Phys. Rev. Lett.* **106**, 243601 (2011).

Experimental State Tomography of Itinerant Single Microwave Photons, C. Eichler, D. Bozyigit, **C. Lang**, L. Steffen, J. M. Fink, and A. Wallraff, *Phys. Rev. Lett.* **106**, 220503 (2011).

Correlation measurements of individual microwave photons emitted from a symmetric cavity, D. Bozyigit, **C. Lang**, L. Steffen, J. M. Fink, C. Eichler, M. Baur, R. Bianchetti, P. J. Leek, S. Filipp, A. Wallraff, M. P. da Silva, and A. Blais, *J. Phys.: Conf. Ser.* **264**, 012024 (2011).

Antibunching of microwave-frequency photons observed in correlation measurements using linear detectors, D. Bozyigit, **C. Lang**, L. Steffen, J. M. Fink, C. Eichler, M. Baur, R. Bianchetti, P. J. Leek, S. Filipp, M. P. da Silva, A. Blais, and A. Wallraff, *Nat. Phys.* **7**, 154 (2011).

Control and Tomography of a Three Level Superconducting Artificial Atom, R. Bianchetti, S. Filipp, M. Baur, J. M. Fink, **C. Lang**, L. Steffen, M. Boissonneault, A. Blais, and A. Wallraff, *Phys. Rev. Lett.* **105**, 223601 (2010).

Quantum-To-Classical Transition in Cavity Quantum Electrodynamics, J. M. Fink, L. Steffen, P. Studer, L. S. Bishop, M. Baur, R. Bianchetti, D. Bozyigit, **C. Lang**, S. Filipp, P. J. Leek, and A. Wallraff, *Phys. Rev. Lett.* **105**, 163601 (2010).

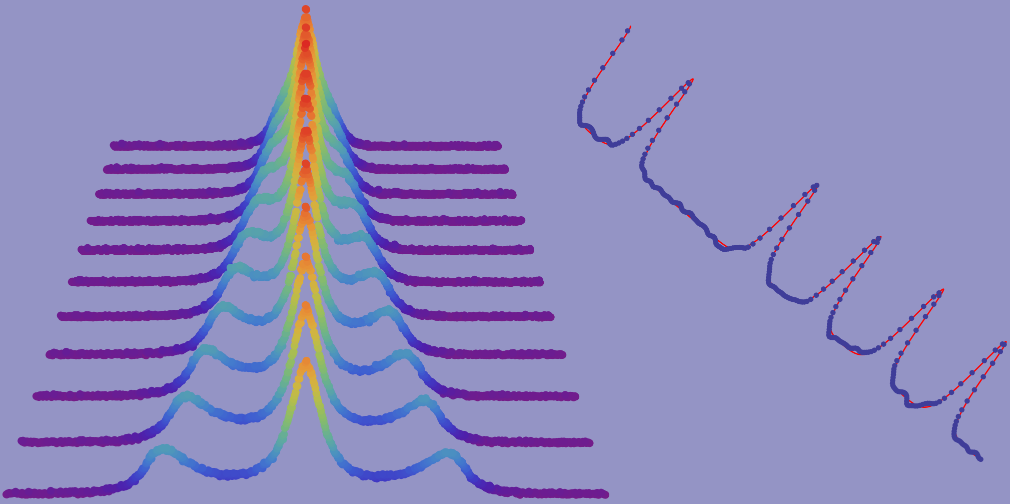

ETH zürich

DISS. ETH NO. 21779